Felipe Walter Dafico Pfrimer

TEMPERATURE MEASUREMENT TECHNIQUE IN FIBER BRAGG GRATINGS NETWORKS USING OPTICAL FEEDBACK

NOVA TÉCNICA PARA MEDIDA DE TEMPERATURA EM REDES DE SENSORES DE GRADES DE BRAGG EM FIBRAS ÓPTICAS USANDO REALIMENTAÇÃO ÓPTICA

Campinas
2013

Universidade Estadual de Campinas
Faculdade de Engenharia Elétrica e de Computação

Felipe Walter Dafico Pfrimer

Temperature measurement technique in fiber Bragg gratings networks using optical feedback

Nova técnica para medida de temperatura em redes de sensores de grades de Bragg em fibras ópticas usando realimentação óptica

Doctorate thesis presented to the School of Electrical and Computer Engineering in partial fulfillment of the requirements for the degree of Doctor in Electrical Engineering. Concentration area: Electronic, Microelectronic and Optoelectronic.

Tese de doutorado apresentada à Faculdade de Engenharia Elétrica e de Computação como parte dos requisitos exigidos para a obtenção do título de Doutor em Engenharia Elétrica. Área de concentração: Eletrônica, Microeletrônica e Optoeletrônica.

Orientador (Tutor): Prof. Dr. José Antonio Siqueira Dias

Este exemplar corresponde à versão final da tese defendida pelo aluno Felipe Walter Dafico Pfrimer, e orientada pelo Prof. Dr. Prof. Dr. José Antonio Siqueira Dias

_____

Campinas
2013

Ficha catalográfica
Universidade Estadual de Campinas
Biblioteca da Área de Engenharia e Arquitetura
Rose Meire da Silva - CRB 8/5974

COMISSÃO JULGADORA - TESE DE DOUTORADO

Candidato: Felipe Walter Dafico Pfrimer

Data da Defesa: 1 de outubro de 2013

Título da Tese: "Técnica Ultra-rápida e de Baixo Custo para Medida de Temperatura Usando Redes de Sensores com Grades de Bragg em Fibras Ópticas"

Prof. Dr. José Antonio Siqueira Dias (Presidente): _____

Prof. Dr. Paulo de Tarso Neves Junior: _____

Prof. Dr. Rogério Lara Leite: _____

Prof. Dr. Elnatan Chagas Ferreira: _____

Prof. Dr. Wilmar Bueno de Moraes: _____

Abstract

The increasing interest in the use of fiber Bragg gratings (FBG) in sensing systems can be explained by some of its features, which are immunity to electromagnetic interference (EMI), electrical insulation, low weight, flexibility, and long distance data transmission capability. This work presents a new interrogation technique capable of measuring temperature of Bragg gratings sensor networks in optical fibers, where an electronic circuit, capable to perform control routines, allows the implementation of an optical feedback. The optoelectronic scheme used is capable of performing the interrogation of all the sensors of the network almost instantly, and allows new sensors to be easily added. A prototype containing two channels was built and tested to validate the technique achieving a high resolution of $\pm$ 1 m°C in temperature measurements in a range of 72°C.

Key-words: Bragg gratings, Fiber Bragg gratings, Sensor networks, Optical fibers.

Resumo

O crescente interesse na utilização de Grades de Bragg (FBG) em sistemas sensores pode ser explicado por algumas de suas características, que são: imunidade à interferência eletromagnética (EMI), isolamento elétrico, baixo peso, flexibilidade, e transmissão de informações a longa distância. Este trabalho apresenta uma nova técnica de interrogação capaz de medir a temperatura de uma rede de sensores de grades de Bragg em fibras ópticas, onde um circuito eletrônico realiza rotinas de controle possibilitando a implementação de uma realimentação óptica. O esquema optoeletrônico empregado é capaz de realizar a interrogação de todos os sensores da rede de maneira quase instantânea, além de permitir que novos sensores possam ser facilmente acrescentados. Um protótipo contendo dois sensores foi construído e testado para validar a técnica obtendo-se uma alta resolução de $\pm$ 1 m°C na medida de temperatura em uma faixa de 72°C.

Palavras-chave: Grades de Bragg, Grades de Bragg em fibra, Rede de sensores, Fibras óticas.

x

Contents

Dedico este trabalho a todos os amigos do DEMIC.

Acknowledgments

List of Figures

List of Tables

Abbreviations and notation list

FBG	Fiber Bragg Gratings
OSA	Optical spectrum analyzer
λ_B	Bragg wavelength
PID	Proportional-integral-derivative
LED	Light-emitting diode
UV	Ultra-violet
IR	Infrared
POF	Polymer optical fiber
OIDA	Optoelectronic Industry Development Association
MCVD	Modified chemical vapor deposition
GODC	Germanium oxygen-deficient center
CW	Continuous wave
n	Index of refraction
n_{cl}	Index of refraction of Cladding
n_{co}	Index of refraction of the fiber core
L	Grating length
h	Planck constant
f_i	Frequency of incident light
f_f	Frequency of reflected light
Λ	Grating period
$\vec{k_i}$	Incident light wavevector
$\vec{K}$	Grating vector
$\vec{k_f}$	Scattered light wavevector
m	Order of diffraction
β	Modal propagation constant
n_{eff}	Effective refractive index
$\delta n(z)$	Average value of the refractive index
$h(z)$	Amplitude of the induced refractive index modulation
$\phi(z)$	aperiodicity of the induced refractive index modulation
$R(l, \lambda)$	FBG reflectivity as a function of the grating length
Ω	Coupling coefficient
Γ	Detuning wavevector

V	Normalized frequency of the fiber
FWHM	Full width half maximum
ε_Z	Applied strain along the fiber axis
p_e	Photo-elastic coefficient
ν	Poisson's ratio
α_n	Thermo-optic coefficient
ε_m	Mechanically caused strain
ε_T	Temperature caused strain
α_Λ	Thermal expansion coefficient
$n_{\text{eff}}^{\text{co}}$	Effective refractive index of the core
$n_{\text{eff,i}}^{\text{cl}}$	Effective refractive index of ith cladding mode
θ_B	Tilted angle of the grating planes
$\lambda_{B,i}^{\text{CL}}$	Resonance wavelength for the cladding mode
CCD	Charge-coupled devise
WDM	Wavelength division multiplexing
AOTF	Acousto-optic tunable filter
FPF	Fabry-Perot filter
Ocp	Optical coupler
ICGI	Identical chirped grating interrogation
PZ	Piezoelectric
MEMS	Microelectromechanical systems
DSP	Digital signal processor
SLED	Superluminescent light emitting diode
ADC	Analog-to-digital converter
DAC	Digital-to-analog converter
TIA	Transimpedance amplifier
PD	Photo diode
VCO	Voltage-controlled oscillator
FSK	Frequency-shift-keyed
AM	Amplitude modulation
TFBG	Tunable fiber Bragg gratings
PZT	Lead zirconium titanate
TEC	Thermo electric cooler
DFB	Distributed feedback laser
TDM	Time division multiplexing
SDM	Spatial division multiplexing
FFT	fast Fourier transform
STB	Signal tracking block
µC	Microcontroller
MCU	Microcontroller
SPS	Samples per second
SPI	Serial-peripheral-interface
USB	Universal-serial-bus
FTDI	Future Technology Devices International

"The most exciting phrase to hear in science, the one that heralds new discoveries, is not 'Eureka!' but 'That's funny'..."

Isaac Asimov

Introduction

OPTICAL fibers have gained great importance over the past four decades mainly due the role they assumed in the scope of telecommunications. The development of fabrication technologies and applications of optical fibers allowed the emergence of devices and equipments that quickly revolutionized optical communications and optical sensing.

One of the events that clearly symbolize this revolution occurred in the late 70's, consisting in the discovery of photo-sensitivity in optical fibers by Hill and coworkers (Hill, Fujii, Johnson & Kawasaki 1978) at the Communication Research Center in Canada, allowing the development of a new kind of optical component, called fiber Bragg Gratings (FBG). This device is capable of realize several functions, such as reflexion and filtering in a very efficient way (Othonos & Kalli 1999). Fiber Bragg Gratings are having a strong impact on the optical sensors field. The advantages offered by the optical fibers such as low loss transmission, immunity to electromagnetic interference, low weight and electrical isolation make the FBGs an ideal candidate to be used in a sensor network (Othonos & Kalli 1999).

A FBG is relatively a very simple device. It consists in a periodic modulation of the index of refraction along the fiber core. This modulation makes the fiber to reflect a portion of the light spectrum centered in a certain wavelength called Bragg or center wavelength, generating a reflection profile, which has the approximate shape of a Gaussian function (Othonos & Kalli 1999). It acts like a wavelength filter, bandpass in reflection and band reject in transmission. These devices appear as elements capable of measuring variations in temperature, pressure and mechanical deformation.

Due to its versatility, the FBG has been widely used for construction of single point and multi-point sensor systems where the characteristics of the optical fibers are desirable. Gratings sensors are small, lightweight and immune to electromagnetic interference (EMI). They are intrinsically passive, meaning that no electrical power is necessary, and therefore can be placed in high voltage and potentially explosive atmosphere areas. The FBG signals are not distance-dependent, being possible more than 50 km connection length (Kreuzer 2008). On a single fiber many Fiber Bragg Gratings can be located and no return fiber is necessary. Furthermore, FBGs sensors possess a very high long term stability and good corrosion resistance (Kreuzer 2008).

Grating sensors find applications where environmental conditions prevents the use of conventional semiconductor-based sensors, thermocouples or thermistors, and since FBGs can be easily multiplexed forming sensor networks, they can provide measurements across long struc-

tures like bridges (Kerrouche, Leighton, Boyle & Gebremichael 2008), naval and space vessels (Banks & Grant 2007, Baldwin, Kiddy, Salter & Chen 2002) and oil pipes (Morikawa, Camerini, Pipa, Santos, Pires, Braga, Llerena & Ribeiro 2008, Zhong, Zhi & Yi 2007, Wang, Zhang, Sun & Yu 2008).

However, for temperature measurements, due to the small dependency of the Bragg shifts with temperature for a naked FBG, interrogators with very high wavelength resolutions are required. For example, since a typical naked FBG presents a typical temperature sensibility of approximately 10 pm°C^{-1} (Othonos & Kalli 1999), the interrogator should present a 1 pm resolution if a resolution of 0.1°C is required in the measurement system.

Therefore, all the advantages of FBG sensors listed here are meaningless without an appropriate demodulation system. One of the most simple demodulation system makes use of an optical spectrum analyzer (OSA), however, due to the bulk size and elevated cost, this type of equipment is limited to laboratory usage. Furthermore, techniques which employ sophisticated optical components in the interrogation system are usually very expensive and cannot be used in low-cost applications (Othonos & Kalli 1999).

There are several studies in the literature which propose low-cost systems for interrogation of FBG sensors. Many of these demodulation systems perform open loop measurements using passive, active filters and tunable narowband light sources (Fallon 1997, Gong 2002, Cai, Hao, Dong & Chiam 2012). There are also systems that perform closed-loop measurements where tunable filters or lasers seek the region of highest reflection of the grating profile (Leite & Ferreira 2007, Cremonezi, Ferreira, Filho & Dias 2013).

No less important is the multiplexing scheme of the sensors. Greater the number of grating sensors that one system supports, lower is the cost per sensor, making the system more competitive. There are several multiplexing techniques, however, the most popular is wavelength division multiplexing (WDM), where each sensor of an array of sensors placed on the same fiber has a specific operation range in the spectrum. In this case, the detection system identify a particular sensor through the wavelength assigned to it.

Objectives and motivations

A simple low cost solution for FBG interrogation is described in (Pfrimer, Koyama, Ferreira & Dias 2013) and is based on the control of the operating point of a small AC signal on a high slope region of the sensor's reflection spectrum (Leite & Ferreira 2007, Cremonezi et al. 2013), witch uses a closed-loop network with an analog electronic PID control to make a DFB laser track the reflection profile on the defined operation point. When the laser stabilizes over the operation point, the FBG temperature can be associated with the laser wavelength. The closed-loop network results in a very accurate system, and a 0.001°C resolution in temperature was obtained(Pfrimer et al. 2013). Despite of the outstanding resolution obtained with such technique, the system cannot be used to interrogate serially multiplexed FBG sensors, and is limited to only one FBG sensor.

Therefore, the objective of this work is the implementation of a novel closed-loop interrogation system which, although based on a similar principle, is capable of multi-point sensing and is

extremely fast, since only a few microseconds are required to read, almost simultaneously, every FBG in the sensor network. It uses a digital control making possible to built a smaller and easy to calibrate electronic circuit. It also uses only one broadband light source to illuminate the FBGs sensors. To validate the technique a two-channel prototype was assembled and tested.

Thesis structure

This thesis is organized in four Chapters. The Chapter 1 makes a brief introduction to the fiber Bragg grating sensors. It begins with a historical perspective and makes a brief commentary of the actual FBG sensors market. This Chapter also describes fundamental conceptions to understand the FBG sensing operation. Chapter 2 describes several demodulation techniques and multiplexing schemes and explains the working principle of the newly proposed demodulation technique. Chapter 3 describes all the optical and electronic hardware developed to validate the technique along with the achieved results. Finally, the last Chapter present the conclusion and prospects for future works.

The basics of Fiber Bragg Grating sensors

As the optical fibers technology matured winning their position in the telecommunications field, efforts were realized by various groups in the world to explore some of the key fiber features and utilize them in sensing applications. In the beginning, fiber optic sensors were just a mere laboratory curiosity. Over time, this kind of sensor began to be increasingly accepted, generating a great impact in many industry areas (Méndez 2007). Optical sensors found widespread use for structural sensing and monitoring applications in civil engineering, aerospace, marine, oil and gas, composites, smart structures, bio-medical devices, electric power industry and many others (Méndez 2007). Among several types of optical sensors the fiber Bragg gratings based sensors become well known, researched and popular, finding a great commercial growth in the last years.

This chapter deals with some concepts of fiber Bragg gratings operation as a sensor, needed to understand the interrogation technique proposed. It begins with a historical perspective of FBG sensors covering the birth of this market. After, some basic concepts of the FBG structure and operation are displayed, emphasizing the dependency of this device with temperature and strain.

1.1 Historical perspective

1.1.1 The discovery of photosensitivity in optical fibers

The 70's witnessed the evolution of fiber optics telecommunications systems, replacing many of the metallic transmission lines and radio systems by fiber optic cables. Systems in the 70's were fundamentally based on multi-mode fibers, since all LED and lasers technology, cleavage and cable splicing were more convenient for this type of fiber and the light guidance properties indicated a lower dispersion in the multi-mode fiber for the wavelengths available at that time (Hecht 1999). At that time, scientist and engineers believed that only transoceanic systems would use single-mode fibers, and the first application of that type of fiber was relegated to the field of sensors, specifically in gyroscopes (Jeunhomme 1990). The situation changed in the 80's, when the multi-mode systems began to be abandoned and single-mode fibers assumed the main role in optical communications and sensor area.

In the second half of the 70's, scientists discovered the photosensitivity of a germanium-doped silica-fibers and, along with this finding, they used the effect to fabricate narrowband Bragg reflectors (Hill et al. 1978, Kawasaki, Hill, Johnson & Fujii 1978), that came to be known as Fiber Bragg gratings, or simply FBG. The developed fabrication technique used an argon ion laser beam with central wavelength of either 488.0 or 514.5 nm, over an optical fiber segment which the final edge was perpendicularly cleaved, producing the 4% Fresnel reflection, generating interference along the fiber between the incident and reflected beam. The stationary wave pattern generated caused a disturbance in the periodic refractive index and induced the formation of the filter reflection, which the band was centered on the wavelength of the laser.

This internal writing technique do not aroused much interest. The motives was the difficult writing repeatability and the reflected wavelength equal to that used for its recording (da Silva 2005).

For almost a decade after the discovery of the photosensitivity in optical fibers, works related to this phenomena were realized occasionally in Canada using special fibers. The lack of international interest of the photosensitivity in optical fibers was due to the reliance in special optical fibers. In 1987 was observed the photosensitivity in different kinds of optical fibers, all with high concentration of germanium (Stone 1987).

In Kawasaki's paper (Kawasaki et al. 1978), became apparent the possibility of tuning the filter through temperature or strain variations, as well as the fabrication of chirped Bragg gratings, in case of a temperature or strain gradient along the optical fiber during the manufacturing process, since that would be relatively simple because the newly formed Bragg grating had the same length of optical fiber segment employed, typically a few tens of centimeters. These ideas would lead fiber Bragg gratings in the sensors field.

Currently, there are two major methods for fabricating Fiber Bragg Grating: interferometric fabrication technique (Meltz, Morey & Glenn 1989) and phase mask method (Hill, Malo, Bilodeau, Johnson & Albert 1993).

In 1989 Gerry Meltz et al. developed a writing technique of Bragg networks through the lateral illumination of the fiber core with a periodic pattern derived from the intersection of two coherent 244 nm beams in an interferometer. The result was a modulation of the core index of refraction. The periodicity of the gratings could be determined by the angle between the intersecting beams, thus making possible reflectance at any wavelength. This writing technique allowed the use of the FBGs in modern telecommunication and sensor systems, since it provided the much-needed degree of freedom to shift the Bragg condition to longer and more useful wavelengths.

In 1993 Hill and coworkers presented the writing technique using phase masks. Phase masks are surface relief gratings etched in fused silica transparent to ultraviolet light. The form of this structure resembles a square wave shape, see figure 1.1. The "period" (or "pitch") of phase mask gratings range from a few hundred nanometers to almost 2 microns. The grating areas come in a wide variety of dimensions, ranging from a few square millimeters to 1500 mm^2. The silica substrates on which the phase mask gratings are etched are typically 1/8" thick. The grating profile is essentially binary (a rectangular wave) for the longer periods, and tends to be somewhat quasi-sinusoidal for the shorter periods (Kuntz 2011).
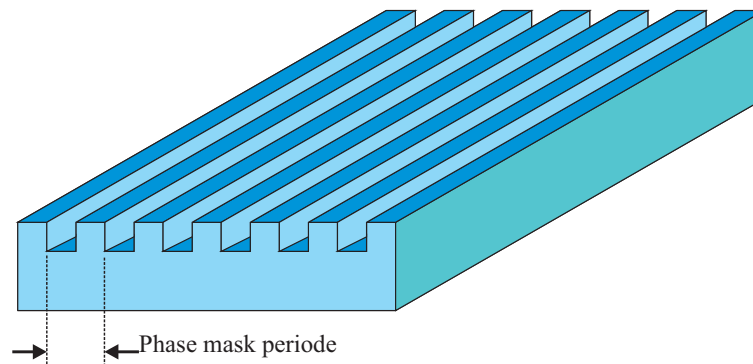
Figure 1.1: Phase masks are surface relief gratings etched in fused silica.
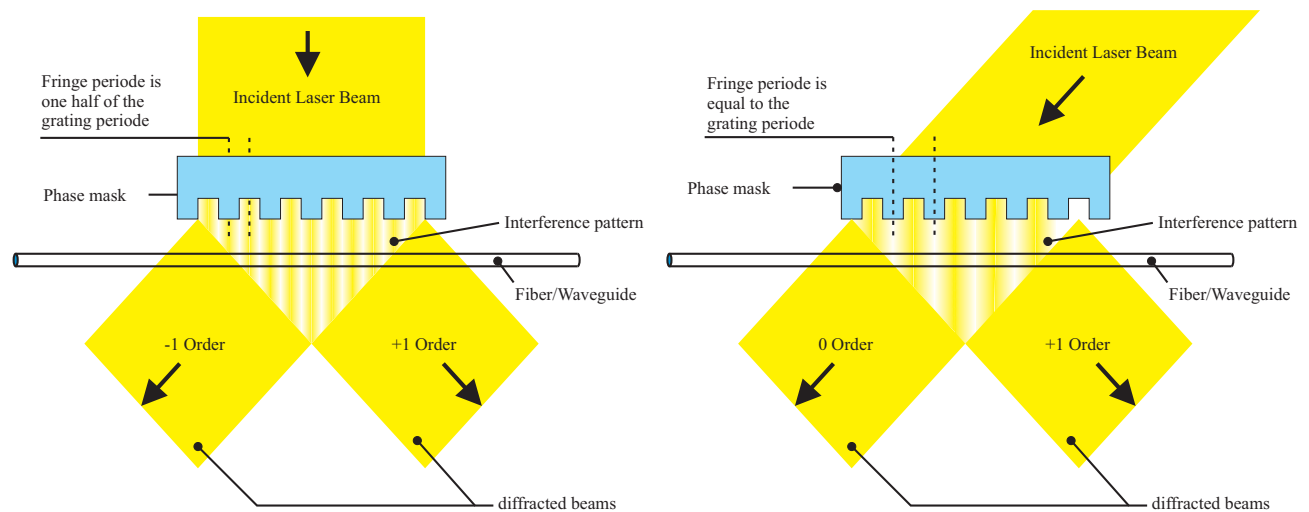
(a) Phase mask configured in the $-1/+1$ configuration.

(b) Phase mask configured in the $0/+1$ configuration.

Figure 1.2: Schematic representations of the phase masks configurations.

Phase masks are typically employed in one of two configurations, $+1/-1$ or $0/-1$, where the numbers refer to the diffracted orders which contain the bulk of the diffracted light (Kuntz 2011). The characteristics of the FBG produced is not dependent on the wavelength of the incident light. In the $+1/-1$ configuration, the UV radiation is directed with normal incidence at the phase mask, and the period of the fringe pattern generated by the interference of the outgoing beams is exactly one half of the period of the phase mask grating as shown in figure 1.2a. In the 0/-1 configuration, the UV radiation is directed at the phase mask with a specially chosen angle of incidence, and the period of the fringe pattern is exactly equal to the period of the phase mask grating (Kuntz 2011), as shown in figure 1.2b.

Also in 1993, Lemaire et al developed a technique to increase the photosensitivity in optical fibers. This technique consists in submit the fiber under high pressure and temperature for a long period of time in a atmosphere filled with hydrogen. (Atkins, Lemaire, Erdogan & Mizrahi 1993, Lemaire, Atkins, Mizrahi & Reed 1993). Instead of FBGs with grating modulation amplitudes barely reaching 10^{-4} without hydrogen, modulation amplitudes approaching 10^{-2} were achieved.

Another important fabrication method, which should be noted, is the point-by-point technique (Malo, Hill, Bilodeau, Johnson & Albert 1993). This technique is accomplished by inducing a change in the index of refraction corresponding to a grating plane one step at a time along the fiber core. A single pulse of UV light from a excimer laser passes through a mask containing a slit. A focusing lens project the slit onto the core of the optical fiber from the side, changing the refractive index of the fiber core locally. The fiber is them translated through a distance Λ, corresponding to the grating pitch, in a direction parallel to the fiber axis. The process is repeated to form the grating structure (Othonos & Kalli 1999).

With the development of the optical fibers and the writing techniques for Bragg networks the use of such components in the development of devices and applications in telecommunications and sensing areas has became more accessible.

1.1.2   The Beginning of the FBG Sensor Market

Despite its appearance in the late 70's the commercialization of FBGs only began to be significant in the second half of the 90's, being driven by the needs of the telecommunications industry. The FBG market was also encouraged during the telecommunications "bubble" expansion which witnessed a tremendous explosion in the number of companies and research groups related to the design, fabrication and encapsulation (Méndez 2007).

After the telecommunications bubble collapse, many companies changed their focus from communications to sensing applications. This change was prudent and strategic since this companies could take advantage from the existing infrastructure they had available. Nevertheless, the sensing sector benefited tremendously from this shift and resulted in an increase in activity and demand of FBG-based sensors.

In the beginning the majority of the sensors applications were centered on discrete, single point sensing of specific parameters, most of then related to temperature and strain. These early commercial FBGs sensors were typically fabricated using phase masks or interferometric methods. Initially, these fabrication techniques relied mostly on manual skills causing limitations on many of the features and performance of the FBGs such as production capacity, repeatability, mechanical strength, and the number of FBGs that could be written on a continuous fiber (Méndez 2007). However, the sensor industry requires multiple sensing points and a greater mechanical strength. These needs of the market demanded more sophisticated and automated fabrication processes allowing the writing of various FBGs sensors inside the same fiber spool.

1.1.3   The actual FBG Sensor Market

The optical sensors is fragmented due to the variety of sensor applications and industries where they are applied. Several niche markets have been established and there are several companies around the world attending the expectations of specific applications and customers (Méndez 2007).

According to Méndez, the current market of optical sensors is composed of three main segments:

Sensing devices: Composed of bare FBGs for sensing applications, packaged FBG sensors and FBG arrays.

Instrumentation: Composed of FBG interrogating instruments and related auxiliary components such as multiplexers, switches, data acquisition systems, software and graphical user interfaces.

System integration and installation services: Covering services like project management and engineering aspects related to implementing sensing solutions and system installations such as design, planning, system integration, customer training, service and on-site installation.

Since the year 2000, more than twenty companies have been active in the FBGs sensor market. In 2000, Micron Optics was able to launch in the market the first line of advanced FBG interrogators, while in 2003 LxSix (now LxDATA) and Sabeus launched the first reel-to-reel production of high reliability FBGs arrays. Finally, in May of 2007 HBM - the world's largest supplier of strain sensing systems - began offering optical strain gages and interrogators based on FBG technology. This was the first time that a conventional strain gage manufacturer adopted and embraced FBGs as an essential part of their product portfolio. A broad and intense commercial pull is expected to follow from this breakthrough (Albert 2011).

According data from *BCC Research Market Forecasting*, the global market value from intrinsic optical sensors, like FBG sensors, grew to almost US$ 1.5 billions in the year 2012 and is calculated to increase to more than $2.5 billion in 2017. the figure 1.3 shows the projection for the 2010 - 2017 period.
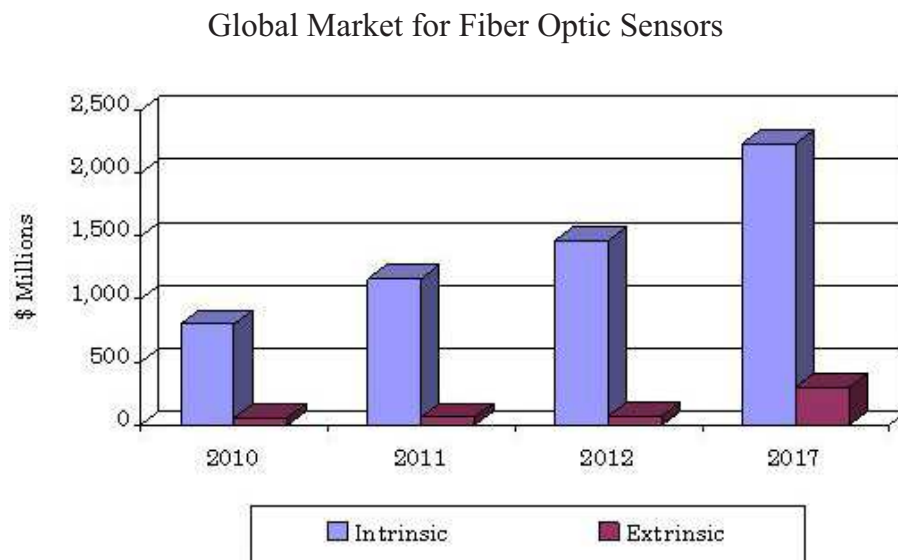
Figure 1.3: Global value for fiber optic sensors by type. Source: *BCC research.*

1.1.4 Future applications

Researchers from many groups in various countries are working on new fabrication techniques, FBG reliability, new device designs, and new data processing techniques (Albert 2011). For instance, FBGs can now be fabricated in many types of glasses using ultrafast IR writing (Grobnic, Mihailov, Smelser & Ramos. 2008) and new post processing techniques have been developed to customize the FBG sensor for enhanced sensitivity in specific applications. New industrial applications have opened up in many strategic sectors, especially in the case of chemical, biological and medical sensing, where a new generation of products and devices will be developed for the measurement of a specific agent or parameter. These products will be possible due to the development of coatings and reagents. Initially such devices will have a higher cost, due to the slow market diffusion and expenses associated with quadruplicated personnel and industry certifications (Méndez 2007).

High temperature resistant FBGs are now possible, operating above 800°C (Wang, Jewart, Canning, Grobnic & andand Kevin P. Chen 2011), open up new applications in harsh environment sectors such as power plants, turbines, combustion and aerospace (Méndez 2007). Similarly, the perspectives of using polymer optical fibers (POF) in sensing applications is expected to lead to the development of POF FBGs for inexpensive, simple and low-cost disposable platforms (Yuan, Stefani & Bang 2012). Similarly, "micro-structured optical fibers are expected to have a major impact in the development of new chemical and biological systems based on optofluidics as well as active and passive microfluidics" (Albert 2011).

Future FBG sensor applications will heavily depend on the cost reduction and development of new encapsulations for specific applications. It is expected that conventional applications such as discrete measurement of temperature and strain will continue to evolve and acquire a greater slice of the market. Likewise, applications with various sensors per fiber will become more popular as prices decrease allowing to compete more directly with truly distributed fiber sensing approaches(Méndez 2007).

Along with the emergence of new applications in the field of FBG sensors there is also the need to develop new interrogation techniques that are fast, efficient and inexpensive. As will be seen in the next chapter, several techniques are being developed in recent years. Being a closed-loop system, the technique developed for this work has many differentials compared to most existing systems and represents a great alternative in the construction of low-cost systems.

1.1.5 The need of a standard

At this time, no standard for FBG sensors was established, resulting in a great variability in the available FBGs designs and specifications offered by the market. It is common a variation in performance of FBG sensors when used in conjunction with instruments from different vendors. Besides, is a tendency to make specific FBGs or FBGs arrays from the scratch resulting in wast of labor time and more expensive components. A standardization will result in easy to fabricate and less expensive products (Méndez 2007).

The group OIDA (Optoelectronic Industry Development Association) has made a initial attempts to create a standard for FBG sensors in sensing applications for WDM and TDM

interrogation schemes (Méndez 2007). However, there is not a formal standard development process.

1.2 Photosensitivity in silicon based optical fibers

The term photosensitivity refers to the permanent change of the index of refraction of the fiber core when exposed to light with a characteristic intensity and wavelength, that depends of the material of the fiber core. Initially, it was thought to be a phenomenon associated only with optical fibers having a strong concentration of germanium in the core, and photo-excited with 240-250 nm ultraviolet light (UV). However, after many years of research, the phenomenon of photosensitivity was observed in a wide variety of optical fibers through photo-excitation at different UV wavelengths (Othonos & Kalli 1999). Nevertheless, Germanium doped optical fibers remains one of the most important materials for the fabrication of devices utilizing photosensitivity.

Many studies related to the dependency of the core dopants have been carried out in order to find whether a particular dopant is necessary to cause the photosensitivity phenomenon. This studies pointed that fibers doped with europium, cerium and erbium-germanium show different degrees of photosensitivity in a silica host optical fiber (Othonos & Kalli 1999). However, the germanium doped fiber presents a better sensitivity.

Initially it was believed that the germanium-oxygen vacancy defects were the only responsible for the photo-induced index changes. However, with the demonstration the photosensitivity in various types of fiber, including polymer fibers, it is clear that this phenomenon is a function of many others mechanisms such as photo-chemical, photo-mechanical and thermo-chemical (Othonos & Kalli 1999). The relative contribution will depend of the intensity and wavelength of the light as well the fiber type.

Several models, that were proposed to describe the chances in the index of refraction in germanium-doped fibers, usually claims that the germanium-oxygen vacancy defects are the precursors responsible for the photo-induced index changes. The photosensitivity occurs when one or two photons are absorbed and it is attributed to the iteration from the UV radiation with four different types of defects in the molecular bonds involving Ge atoms (da Silva 2005). In the modified chemical vapor deposition technique (MCVD) for optical fiber fabrication, during the high-temperature gas-phase oxidation process, GeO_2 dissociates to the GeO molecule due to its higher stability at higher temperatures (Othonos & Kalli 1999). When this molecule is incorporated into the fiber it can manifest in the form of oxygen vacancy Ge-Si and Ge-Ge wrong bonds. The absorption band is independent of the defect present in the glass structure. The band have its peak at 242 nm and its center are known as germanium oxygen-deficient centers or GODCs. The four most common types of defects in germanium-doped optical fibers are shown in figure 1.4.

The GeO defect, shown in figure 1.4a, occurs the germanium atom is bonded to only three atoms of oxygen and the fourth bond occurs with an atom of Si or Ge. This defect induce the appearance of a optical absorption band around 240 nm and spectral width of about 30 nm. It is believed that this type of defect causes the photosensitivity phenomenon in germanium-doped

(a) GeO defect.

(b) GeE′ defect.

(c) Ge(1) defect.

(d) Ge(2) defect.
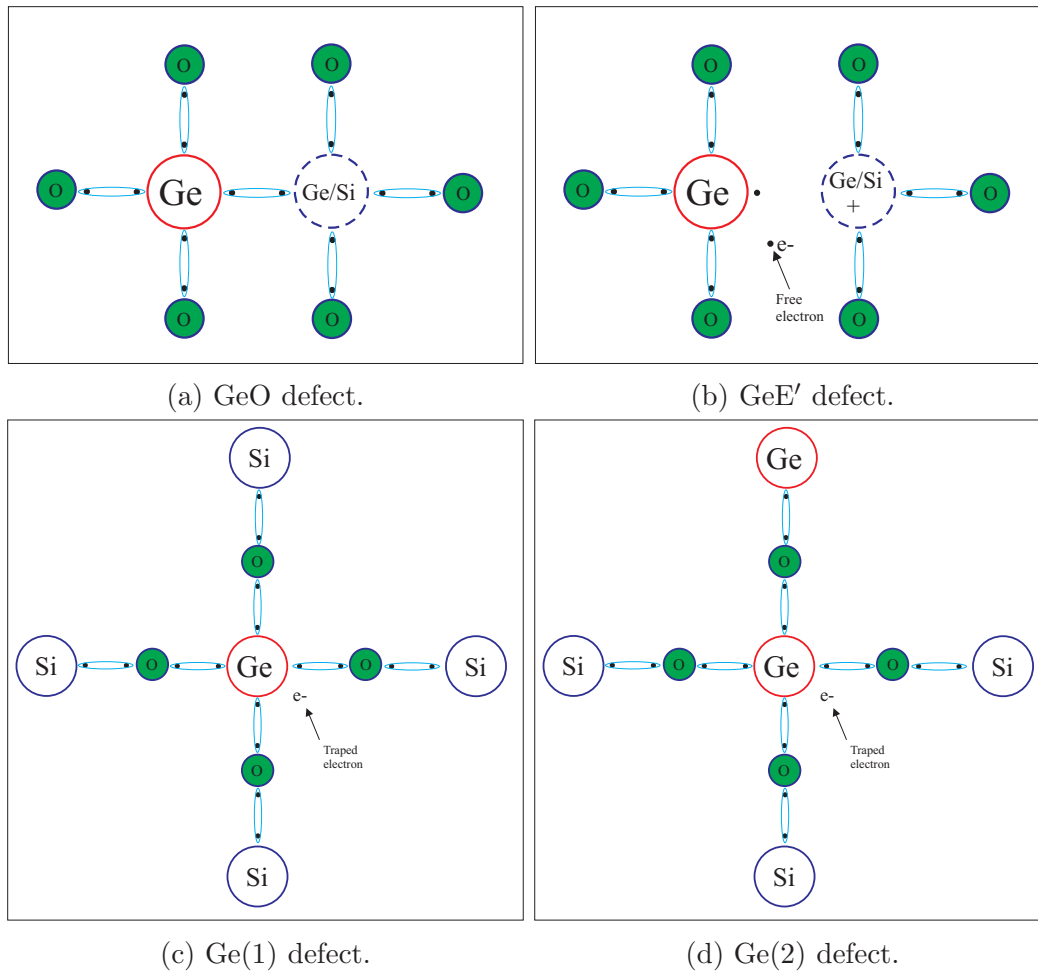
Figure 1.4: Most common types of defects in germanium-doped optical fibers (Kashyap 1999).

optical fibers (Atkins & Mizrahi 1992).

The GeE′ defect, shown in figure 1.4b, occurs when one of the bonds Ge − Ge or Ge − Si is broken and one electron stays free to move in the glass molecular structure through hopping or tunneling, or by two-photon excitation into the conduction band (Kashyap 1999). The removal of this electron causes a reconfiguration in the molecule structure, also enabling a material density change and optical absorption. The concentration of this type of defect increases after some elevated UV or visible light exposure, showing long lifetime even in room temperature (da Silva 2005).

The types Ge(1), showed in figure 1.4c, and Ge(2), showed in figure 1.4d, present the regular tetrahedral configuration, however, they have one additional electron trapped in the Ge atom (Kashyap 1999). The numbers (1) and (2) are related with the presence of one Si or Ge atom respectively, present in the material immediately adjacent to this structure.

Another type of defect that appears to be responsible for the photosensitivity in optical fibers is the GeO_2. This center comes when one Ge atom replaces one silicon atom in the glass structure, inducing the appearance of a absorption band around 195 nm (da Silva 2005).

The physical mechanisms behind the photosensitivity in optical fibers are still not completely understood and further detailed investigations is needed in order to clarify this phenomenon.

1.2.1   Methods to increase in photosensitivity in optical fibers

The characteristics of a FBG highly depends of how much the refractive index is changed during the writing. Therefore, it is desirable to increase the photosensitivity of the fiber allowing more efficient writings, eliminating the need of high optical power in the inscribing beam and long periods of exposition, increasing the production efficiency. Some techniques allow a higher photosensitivity increasing the concentration of Ge inside the fiber core, or inducing hydrogen in the glass structure, or even utilizing another types of dopants like boron (B) in conjunction with Ge.

A higher Ge concentration is not a recommended technique in most of the cases, because results in a more thick fiber, causing more insertion loss (da Silva 2005).

It was demonstrated a increased photosensitivity in fibers treated with heated hydrogen (Atkins et al. 1993, Lemaire et al. 1993, Meltz & Moery 1991). Since the hydrogen remains chemically trapped inside the material the hydrogen treatment will permanently increase the photosensitivity. According to Lemaire et al, the fiber must be submitted in a high pressure H_2 atmosphere, around 20 atm - 748 atm, and with temperature between 20°C and 75°C during some days. This allows FBG writing with a high refractive index change ($\Delta n \approx 10^{-3}$ to 10^{-2}) in optical fibers, with lower optical power and lower time exposition. The hydrogen diffusion under high pressure in optical fibers in room temperature results in refractive index changes higher than 0.01, with almost all germanium participating of the vacancy formation after the UV light exposition (Lemaire 1991). Optical fibers treated with cold hydrogen and high pressure remain photosensitive while the hydrogen is present, therefore, they must be kept over low temperatures or high pressures in hydrogenated atmospheres to stop the diffusion of hydrogen out of the fiber (da Silva 2005).

Standard optical fibers, like the SMF-28, presents a low intrinsic photosensitivity due to the low concentration of Ge. Thereby, an alternative photosensitization technique is the fiber scanning with hydrogen in flame (Flame Brushing) (Hill, Malo, Bilodeau & Johnson 1993). In this technique the fiber is exposed over a oxy-hydrogen flame, which the temperature cam be higher than 1700°C approximately. In high temperature the hydrogen diffuses into the core faster than in room temperature. This treatment results in permanently photosensitive optical fiber and brings the advantage of make a local photosensibilization. This technique allows fiber Bragg gratings, stable with temperature, to be fabricated in standard optical fibers used in telecommunications, which present low intrinsic photosensibilization due to the low concentration of germanium (da Silva 2005).

1.3   Photosensitivity Types of Bragg Gratings

To optimize the fabrication of Bragg gratings, the growth dynamics of the gratings planes as the fiber is exposed to UV light must be studied. This dependency can be a complex issue since there are various parameters that must be analyzed, such as: the fiber type, different UV radiation bands, and laser power available (Othonos & Kalli 1999).

1.3.1 Type I Bragg grating

Type I Bragg gratings refer to gratings that are formed in normal photosensitive fibers under moderate intensities (Othonos & Kalli 1999). It corresponds a monotonic increase in the amplitude of the refractive index of modulation and is observed in most photosensitive fibers. This type o grating can be written on either continuous wave (CW) or pulsed UV radiation. This type of Bragg grating is produced with 100 mJ/cm^2/pulse with a cumulative energy that is typically greater than 500 J/cm^2 (Othonos & Kalli 1999). The exposure to the writing lasers results in a positive change of the refractive index ($\Delta n > 0$).

The low power used during the writing process not necessarily results in low reflection profiles. Bragg gratings with reflectivity near 100% are achieved (Othonos & Kalli 1999).

Type I Bragg gratings can be easily erased in relatively low temperatures (around 200°C). However, type I Bragg gratings are the most used and can work from -40°C to +80°C, a temperature range that cover most of telecommunication and sensing applications (Othonos & Kalli 1999).

Another fundamental characteristic of type I Bragg grating is that the reflection spectra of the guiding mode is complementary to the transmission signal, as a result of the negligible loss due to absorption or reflection into the cladding (Othonos & Kalli 1999).

Continuous wave radiation has better modal quality and spacial uniformity than pulsed beans. Thus, type I Bragg gratings with great reproductivity can be fabricated with CW radiation and, once all the parameters needed to engrave gratings with specifics characteristics are set, the grating can be replicated in another region of the fiber. As the writing process can be monitored in real time, it is possible to change parameters during the fabrication process aiming desired characteristics (da Silva 2005).

1.3.2 Type IIA Bragg grating

Prolonged exposure of the type I Bragg grating results in partial or complete erasure of the original reflection profile and the appearance of another spectral formation. This new reflection spectrum is associated with a very negative Δn (Othonos & Kalli 1999).

During the fabrication process of the type IIA Bragg grating the center wavelength of the original type I grating moves towards bigger wavelengths of the spectrum, showing the positive change of the refractive index. At the time of erasure of the type I grating, the center wavelength of the type IIA either shifts towards shorter wavelengths or does not significantly shift, indicating a negative change in the refractive index (Othonos & Kalli 1999).

The formation of the reflection profile of type IIA Bragg gratings is not completely understood. Two different dynamic stages are being suggested to justify the experimental observations. The first stage is relatively fast and correspond to the intrinsic photosensitivity of the optical fibers, being responsible by the positive change in the refractive index during the formation of the type I Bragg grating. The second stage is normally slower and it seems to be related with the relaxation of the accumulated tension in the fiber core resulting in the negative change of the index (Riant & Haller 1997).

Type IIA Bragg gratings have the same spectral characteristic of type I gratings since the

transmission and reflection spectra are complementary. Figure 1.5 shows an illustration of a typical transmission and reflection profiles of a type I and IIA Bragg gratings. However, due to the different mechanism involved in the fabrication process, some distinguishable features are visible either in the initial fabrication or in the gratings temperature of erasure. Type IIA gratings are achieved through a long process, following type I grating formation and disappearance. At approximately 30 minutes of exposure the type IIA grating is complete (Othonos & Kalli 1999). The long period of fabrication makes this type of grating not very practical to fabricate.
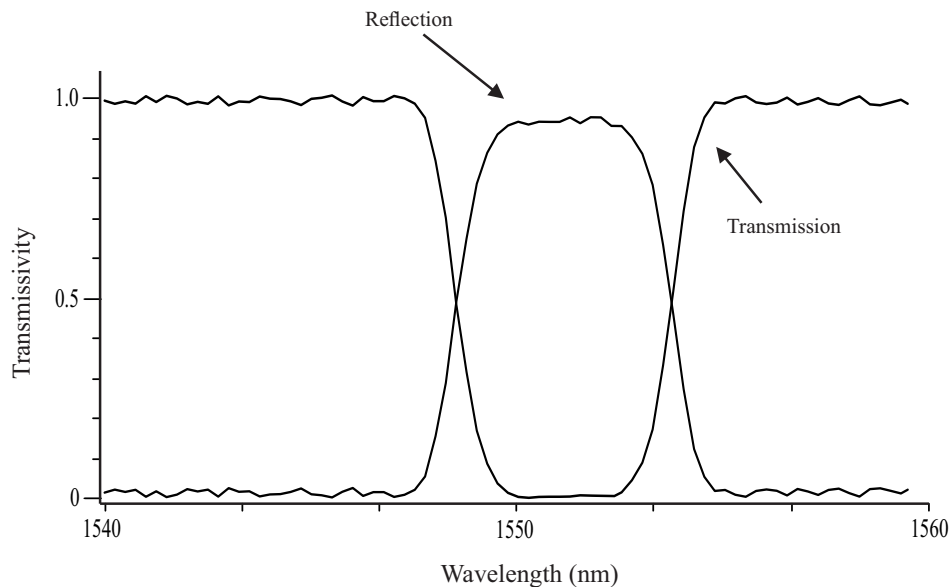
Figure 1.5: Illustration of a typical transmission and reflection profiles of a type I and IIA Bragg gratings. The transmission and reflection spectra are complementary.

A clear advantage of the type IIA Bragg grating over the type I is the temperature stability. Type IIA gratings are erased only in temperatures as high as 500°C, making them very useful in sensing applications if the system is exposed in high ambient temperatures.

1.3.3   Type II Bragg grating

The major advantage of pulsed writing systems for Bragg gratings is that the intensity of the pulse is usually so high that few pulses are enough to create the grating planes. However the radiation power can be so high that the mechanical damage caused in the glass structure may be considerable. Bragg gratings with great stability can be inscribed with this method.

If the energy level utilized to write the FBG is grater than 1,000 mJ/cm^2 in a unique pulse beam, type II Bragg grating can be formed on the draw tower (Archambaut, Reekie & Russel 1993). Type II Bragg grating is the result of physical damage of the fiber core due to the large amount of energy of the writing process. Index changes of 10^{-2} can be observed. An illustration of the transmission and reflection spectrum of a type II grating is shown on figure 1.6.

The reflection profile appears to be broad, and several characteristics over the spectrum are believed to be caused by the nonuniformities in the excimer bean profile that are heavily
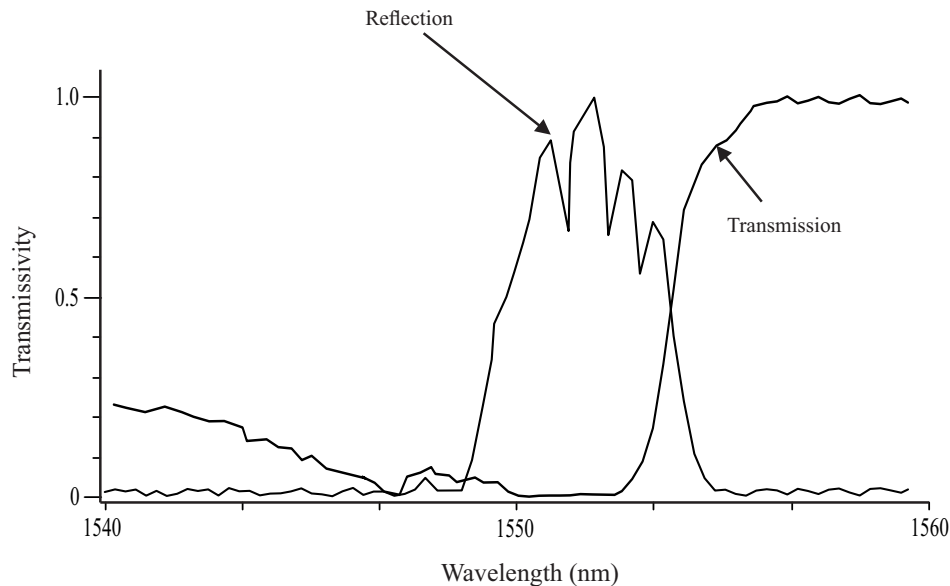
Figure 1.6: Illustration of a typical transmission and reflection profiles of a type II Bragg gratings.

amplified by the great nonlinear response mechanism of the fiber core. As observed in figure 1.6 the transmission profile of the type II grating is longer than the refection, whereas shorter wavelengths are strongly coupled into the cladding (Archambaut et al. 1993, Dong, Archambault, Reekie, Russel & Payne 1993), allowing their use as wavelength selective taps (Othonos & Kalli 1999). Furthermore, type II gratings are also characterized by the relatively high insertion loss, typically between 0.2 and 2 dB. This loss seems to depend of the Bragg wavelength and of the extension of the damage over the fiber core (da Silva 2005).

Type II Bragg gratings presents a elevated temperature stability. Gratings of this kind can operate in temperatures near 800°C during a 24 hours period without change their characteristics. Around 1000°C most of the grating disappears after 4 hours (Othonos & Kalli 1999). This elevated temperature stability make the type II gratings ideal candidates to be used in very hostile environments.

One characteristic of great practical importance of type II gratings is that the duration of the beam pulse used in the fabrication process, usually lasts a few nanoseconds. This is of great importance for large scale production of strong gratings during the fiber drawing process before the application of the coating.

Type II Bragg gratings possess no relation with type IIA gratings. There is no similarity in the mechanisms responsible for the formation these gratings types.

1.3.4   Type IA Bragg grating

In 2002, studies presented a new kind o Bragg grating, known as type IA (Liu, Williams, Zhang & Bennion 2002). This type of grating is written in hydrogenated fibers with high concentration of germanium. It presents, as the main characteristic, a low temperature sensitivity of approximately 6.4 pm/°C (an average Bragg grating presents a temperature sensitivity between 10 and 14 pm/°C).

Type IA gratings are written with 244 nm laser with a elevated exposure time, approximately four hours with radiation power of 60 mW. Due to the long period of exposition, the grating undergoes an annealing process, caused by the heating generated inside the fiber by the UV radiation absorption.

Due to the long exposure time, it was expected the formation of a type IIA grating, but a different spectral behavior was observed. A initial formation similar of the type IIA was observed, but the central wavelength continuously shifted towards higher wavelengths. From the beginning of the process until the end, the Bragg wavelength shifted 18 nm, which indicates a high variation of the refractive index. This type of grating was applied in strain measurements, where the type IA grating was utilized to compensate temperature variations of the sensing type I Bragg grating (Simpson, Kalli, Zhou, Zhang & Bennion 2003).

1.4   Properties of Fiber Bragg Gratings

A Fiber Bragg Grating or FBG, in its simplest form, is a devise built inside a single-mode optical fiber consisting in a periodic modulation of the fiber core along its length. It acts like a wavelength filter, bandpass in reflection and band reject in transmission. The parallel planes of greater and lesser amplitudes of the index of refraction, that are localized across the core, form the basic Bragg structure, as shown in the figure 1.7. The light, guided along the core of an optical fiber, will be scattered by each grating plane. If the bragg condition is not satisfied, the light reflected by the planes becomes progressively out of phase and eventually will cancel out. The light component that is not coincident with the Bragg wavelength resonance will suffer very weak refection at each grating plane (Othonos & Kalli 1999).

Figure 1.7 shows the structure of a single-mode optical fiber with a Bragg grating inscribed inside the core which is out of scale for better visualization. The fiber core and the cladding has the refractive index n and n_{cl} respectively. The Bragg grating structure can be observed by the various parallel planes with index of refraction $n + \Delta n$ placed along the fiber core. The grating length is given by L.

The Bragg condition can be understood as a requirement that satisfies both momentum and energy conservation (Othonos & Kalli 1999). The energy of an electromagnetic wave is given by $E = h \cdot f$, where h is the Plank constant. Thus, in order to the energy to be conserved, the frequency of the incident light, f_i, and the reflected light, f_f, must be the same $(h \cdot f_i = h \cdot f_f)$. The momentum conservation requires that the wavevector of the incident light, $\vec{k_i}$, added to the grating vector, $\vec{K}$, must be equal to the wavevector of the scattered light $\vec{k_f}$. The momentum conservation can be stated as equation 1.1:

$$\vec{k_i} + \vec{K} = \vec{k_f} \tag{1.1}$$

The direction of the grating wavevector, $\vec{K}$, as can be seen in figure 1.7, has direction normal to the grating planes and magnitude $2\pi/\Lambda$ where Λ is the grating period. The diffracted wavevector is equal in magnitude, but opposite in direction, to the incident wavevector. Therefore the momentum conservation condition can be written accordingly to the equation 1.2
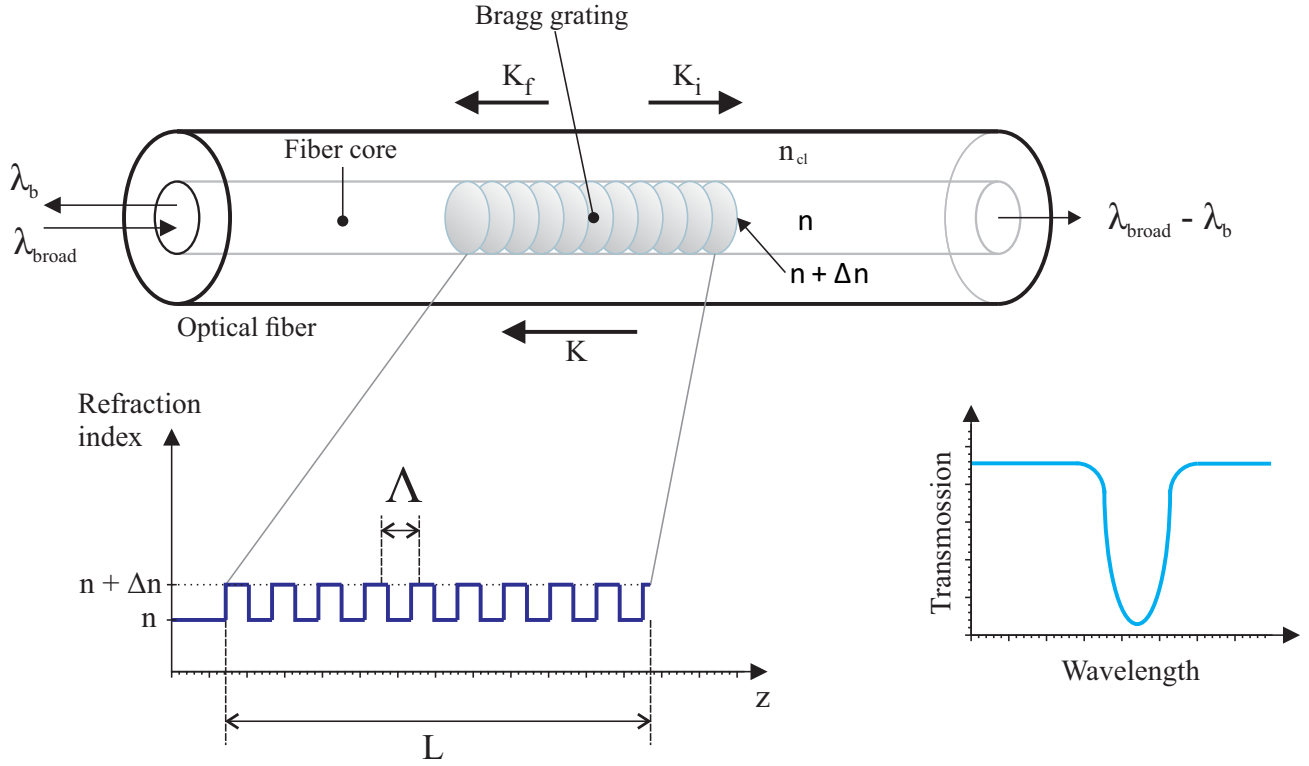
Figure 1.7: Illustration of a uniform Bragg grating with constant index of modulation, amplitude and period. The incident, diffracted, and grating wavevectors have to be matched form momentum to be conserved.

(da Silva 2005):

$$\frac{2\pi n}{\lambda}\sin\theta_f = \frac{2\pi n}{\lambda}\sin\theta_i + m\frac{2\pi}{\Lambda} \tag{1.2}$$

The element m represents the order of diffraction, where $m = -1$ for optical fibers. Since the modal propagation constant, β, is given by $\beta = (2\pi/\lambda)n_{\text{eff}}$, where n_{eff} is the effective refractive index of the fiber core at the free space center wavelength (Othonos & Kalli 1999), the equation 1.2 can be rewritten accordingly to the equation 1.3:

$$\beta_f = \beta_i - \frac{2\pi}{\Lambda} \tag{1.3}$$

The momentum conservation condition can be expressed accordingly to the equation 1.4:

$$2\left(\frac{2\pi n_{\text{eff}}}{\lambda_B}\right) = \frac{2\pi}{\Lambda} \tag{1.4}$$

The equation 1.4 can be simplified to the first order Bragg condition, accordingly to the equation 1.5:

$$\lambda_B = 2n_{\text{eff}}\Lambda \tag{1.5}$$

In the equation 1.5 λ_B represents the Bragg grating wavelength. Only wavelengths very near of λ_B that will back-reflected by the grating inside the fiber core. The others wavelengths will

be transmitted.

1.4.1   Fiber Bragg Grating Reflectivity

A fiber Bragg grating engraved inside an optical fiber has its refractive index given by the expression represented by the equation 1.6 (Erdogan 1997):

$$n(z) = \delta n(z) + h(z)cos\left(\frac{2\pi z}{\Lambda} + \phi(z)\right) \tag{1.6}$$

In the equation 1.6, z is the independent variable representing the propagation direction, $\delta n(z)$ represents the average value of the refractive index modulation calculated over the period Λ, $h(z)$ and $\phi(z)$ is the amplitude and aperiodicity of the induced refractive index modulation. If the phase $\phi(z)$ varies along the direction z it can be said that the grating presents *chirp*, which means that the period of the grating varies along the structure. When the amplitude $h(z)$ varies along the fiber, lateral peaks of the reflection profile can be minimized. The process that reduces the amplitude of the lateral lobules in the reflection profile is called apodization.

The main peak in the reflection spectrum in a Bragg grating with uniform modulation of the index of refration is aways accompanied by a series of side-lobes, at wavelengths near λ_B. This side-lobes has its origins in the discontinuity of the index of refraction in the edges of the grating structure. However, many application requires a good separation of multiplexed channels in wavelength. Thus, the existence of this lobes reduces the isolation between the channels, affecting the performance of the device. In this situation is necessary utilize apodization techniques to reduce the lateral lobes.

In order to achieve an apodized reflection profile, the amplitude $h(z)$ is gradually reduced in the edges, minimizing the discontinuity of the index of refraction, as can be observed in figure 1.8.

The fabrication of apodized FBGs is intrinsic to systems that utilizes UV lasers with appropriate transversal intensity profile. In this case, the distribution of the index of refraction modulation amplitude is similar to the transversal intensity profile of the UV source (Mizrahi & Sipe 1993). Another technique consists of translating a UV beam along the fiber through a phase mask, varying the effective time exposure in each position (Martin & Ouellette 1995).

Through the coupled mode theory (Lam & Garside 1981) that described the reflection properties of a fiber Bragg grating, the reflectivity of a FBG with constant modulation amplitude ($h(z)$ constant) and constant period is given by the expression 1.7:

$$R(l, \lambda) = \frac{\Omega^2 \sinh^2(sl)}{\left(\frac{\Gamma}{2}\right)^2 \sinh^2(sl) + s^2 \cosh^2(sl)} \tag{1.7}$$

In the equation 1.7, $R(l, \lambda)$ represents the reflectivity as a function of the grating length, l, and wavelength λ. The symbol Ω is the coupling coefficient, and Γ represents the detuning wavevector for a given wavelength of the optical source spectral band.

The detuning wavevector, Γ, is given by the expression 1.8 (Lam & Garside 1981):

$$\Gamma = \left(2\frac{2\pi n_{eff}}{\lambda}\right) - \left(\frac{2\pi}{\Lambda}\right) \tag{1.8}$$
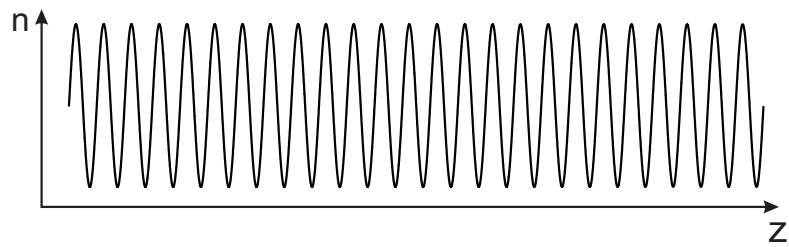
(a) Uniform modulation of the refractive index n.
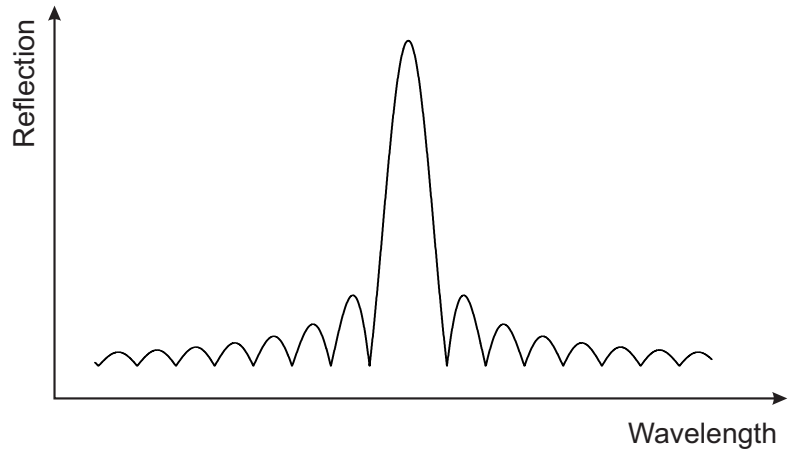
(b) Reflected spectrum of a FBG with uniform modulation of the refractive index.
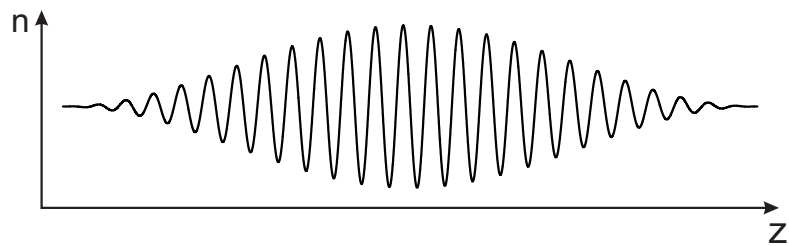
(c) Non-uniform modulation of the refractive index n.
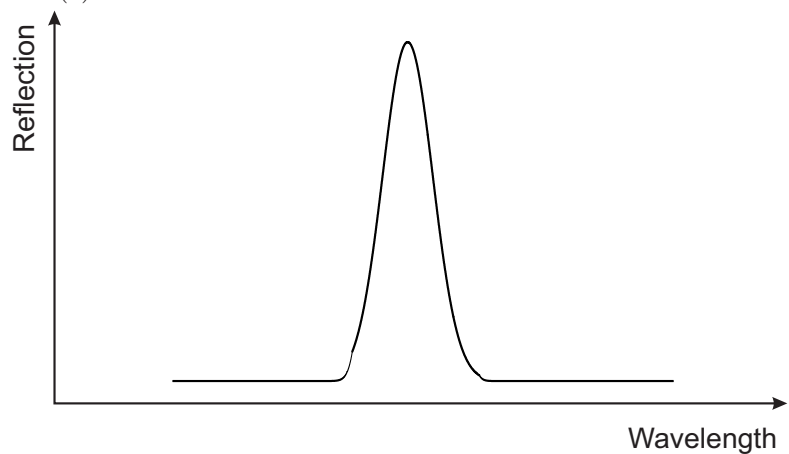
(d) Reflected spectrum of a FBG with non-uniform modulation of the refractive index.

Figure 1.8: Schematic representation of an apodized and a non-apodized FBG. The side-lobes has its origins in the discontinuity of the index of refraction in the edges of the grating structure. With an apodized modulation the side-lobules are reduced.

In the equation 1.7 the parameter s is given by the expression 1.9:

$$s = \sqrt{\Omega^2 - \left(\frac{\Gamma}{2}\right)^2} \tag{1.9}$$

The coupling coefficient, Ω, for a sinusoidal variation of the refraction index along the fiber axis can be defined by the equation 1.10 (Othonos & Kalli 1999):

$$\Omega = \frac{\pi \delta n_{\text{eff}}}{\lambda} M_p \tag{1.10}$$

In the equation 1.10, M_p represents the fraction of the fiber mode power contained by the fiber core. Assuming the Bragg grating is uniformly written through the fiber core, the value of M_p can be approximated by the expression 1.11 (Othonos & Kalli 1999):

$$M_p = 1 - \frac{1}{V^2} \tag{1.11}$$

The parameter V, in the equation 1.11, is the normalized frequency of the fiber, and it is given by the expression 1.12:

$$V = \left(\frac{2\pi}{\lambda}\right) a \sqrt{n_{\text{co}}^2 - n_{\text{cl}}^2} \tag{1.12}$$

In the equation 1.12 the term a is the fiber core radius, n_{co} and n_{cl} are the refractive index of the core and the cladding, respectively.

In the Bragg grating central wavelength there is no wavevector detuning, in other words, $\Gamma = 0$. Therefore, the expression for the reflectivity becomes the expression 1.13 (Albert 2011):

$$R(l, \lambda) = \tanh^2(\Omega l) \tag{1.13}$$

A general expression for the approximate full-width-half-maximum bandwidth, or FWHM, of a grating reflection profile is given by the equation 1.14 (Russell, Archambault & Reekie 1993):

$$\Delta\lambda = \lambda_B s \sqrt{\left(\frac{\Delta n}{2n_0}\right)^2 + \left(\frac{1}{N}\right)^2} \tag{1.14}$$

The value N from the expression 1.14 represent the number of grating planes ($N = l/\Lambda$). The parameter s is approximately 1 for strong gratings, with reflection near 100%, and 0.5 for weak gratings (Othonos & Kalli 1999).

The expressions 1.13 and 1.14 shows that the reflectivity increases and the FWHM decreases as the induced change in the index of refraction increases. It also shows that higher grating lengths increases the reflectivity and decreases the FWHM.

1.4.2   Strain and Temperature Sensitivity of FBGs

According to equation 1.5, the center wavelength, λ_B, of back-reflected light from a Bragg grating, depends on the refractive index of the core and the periodicity of the grating. The effective index of refraction and the periodic spacing between the grating planes are both affected

by strain and temperatures changes. Therefore, any perturbation that changes those quantities will induce a shift in the relative position of λ_B.

Using equation 1.5, the change in the FBG center wavelength is given by the expression 1.15 (Othonos & Kalli 1999).

$$\Delta\lambda_B = 2\left(\Lambda\frac{\partial n_{\text{eff}}}{\partial l} + n_{\text{eff}}\frac{\partial\Lambda}{\partial l}\right)\Delta l + 2\left(\Lambda\frac{\partial n_{\text{eff}}}{\partial T} + n_{\text{eff}}\frac{\partial\Lambda}{\partial T}\right)\Delta T \qquad (1.15)$$

The first term from the equation 1.15 represents the strain effect on the optical fiber. This term correspond to a change in the grating spacing, Λ, and the strain-optic induced change in the refractive index.

The strain effect can be expressed by the expression 1.16 (Othonos & Kalli 1999):

$$\frac{\Delta\lambda_B}{\lambda_B} = (1 - p_e)\,\varepsilon_Z \qquad (1.16)$$

In the equation 1.16, $\Delta\lambda_B$ is the wavelength shift, ε_Z is the applied strain along the fiber axis, and p_e is the photo-elastic coefficient, and it is defined by equation 1.17(Othonos & Kalli 1999):

$$p_e = \frac{n_{\text{eff}}^2}{2}\left[p_{12} - \nu\left(p_{11} + p_{12}\right)\right] \qquad (1.17)$$

The terms p_{11} and p_{12} are components of the strain-optic tensor, and ν is the Poisson's ratio. The values of this terms for a typical germanium-doped optical fiber are $p_{11} = 0.113$, $p_{12} = 0.252$, $\nu = 0.16$, and $n_{eff} = 1.482$. Replacing this values in equation 1.17, it is obtained $p_e = 0.213$. Substituting the value of p_e in equation 1.16 the expected strain sensitivity at 1550 nm is about 1.2 pm/$\mu\varepsilon$, assuming constant temperature.

The second term in equation 1.15 represents the effect of temperature on a FBG. Thermal expansion will cause changes in the index of refraction, thus, shifts in the Bragg wavelength will be observed. The wavelength shift for a temperature change ΔT may expressed by equation 1.18 (Kreuzer 2008):

$$\frac{\Delta\lambda_B}{\lambda_B} = \alpha_n\Delta T \qquad (1.18)$$

The quantity $\alpha_n = (1/n_{\text{eff}})(\partial n_{\text{eff}}/\partial T)$ represents the thermo-optic coefficient, which is approximately equal to $8.6 \times 10^{-6}\ K^{-1}$ for germanium-doped fibers.

It is important to note that any change in the central wavelength of a FBG, caused by a external perturbation, is the sum of temperature and strain terms. Thus, the total change in the center wavelength is given by equation 1.19

$$\frac{\Delta\lambda_B}{\lambda_B} = (1 - p_e)\,\varepsilon_Z + \alpha_n\Delta T \qquad (1.19)$$

The strain, ε_Z, may be caused by mechanical force and/or temperature as described by equation 1.20 (Kreuzer 2008):

$$\varepsilon_Z = \varepsilon_m + \varepsilon_T \qquad (1.20)$$

The value ε_m is the mechanically caused strain $(\Delta L/L)$ and ε_T is the temperature caused strain. ε_T can be calculated by the equation 1.21:

$$\varepsilon_T = \alpha_\Lambda \Delta T \tag{1.21}$$

The term $\alpha_\Lambda = (1/\Lambda)(\partial\Lambda/\partial T)$ in equation 1.21 is the thermal expansion coefficient of the fiber or the substrate if the Bragg grating is bonded. The value of α_Λ is approximately 0.55×10^{-6} K^{-1} for silica.

Substituting the equations 1.20 and 1.21 on equation 1.19, it is obtained equation 1.22 (Kreuzer 2008):

$$\frac{\Delta\lambda_B}{\lambda_B} = (1 - p_e)\left(\varepsilon_m + \alpha_\Lambda \Delta T\right) + \alpha_n \Delta T \tag{1.22}$$

In case of a pure temperature sensor, the Bragg grating is not stressed. Therefore, the center wavelength of the FBG changes only with temperature according to equation 1.23 (Kreuzer 2008):

$$\frac{\Delta\lambda_B}{\lambda_B} = \left[(1 - p_e)\alpha_\Lambda + \alpha_n\right]\Delta T \tag{1.23}$$

Substituting the values of α_Λ and α_n in equation 1.23 it is obtained the expected temperature sensitivity for a 1550 nm Bragg grating, which is approximately 14 pm/°C. Since $\alpha_\Lambda << \alpha_n$, it is evident that the index change is by far the dominant effect.

In some cases the FBG may be bonded on a metallic substrate to act as a strain gage or to improve the temperature sensitivity. When the fiber is fixed in a substrate the FBG signal $\Delta\lambda_B/\lambda_B$ changes with strain $(\varepsilon_m + \varepsilon_T)$ of the substrate and therefore the thermal expansion coefficient α_Λ is the coefficient of the substrate and not from the silica. Table 1.1 shows the thermal expansion coefficient of some materials used as substrate and the expected temperature sensibility of the bonded FBG.

Material	α_Λ ($10^{-6}\times K^{-1}$)	Sensitivity @1550 nm (pm/°C)
Silica	0.55	14.0
Steel	13.0	29.2
Aluminum	22.2	40.4
Zinc	29.7	49.6
Cooper	16.6	33.6
Lead	28.0	47.6

Table 1.1: Thermal expansion coefficient of some materials used as substrate and the expected temperature sensibility of the bonded FBG

Figure 1.9 shows experimental results of a FBG bonded on a zinc substrate. The FBG presented a temperature sensitivity of 48,8 pm/°C, very close of the theoretical value. A thermal chamber was utilized to change the temperature of the bonded FBG. The center wavelength was monitored by an OSA.
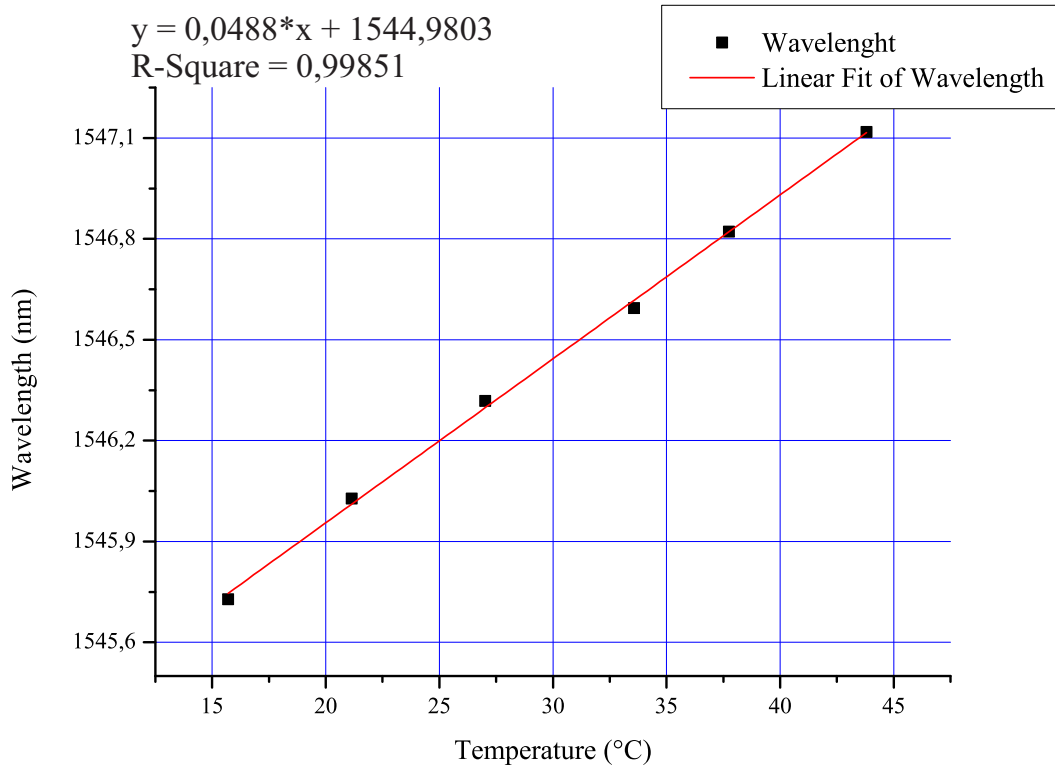
Figure 1.9: Experimental results of a FBG bonded on a zinc substrate.

1.5 Grating structures

According to (Othonos & Kalli 1999) there are three main types of fiber Bragg gratings structures: the common Bragg reflector, the blazed Bragg grating, and chirped Bragg grating. What differentiates these types of structures is either their grating pitch (the spacing between grating planes, Λ) or the angle between the grating planes and the fiber axis. The common Bragg reflector, which is the most common Bragg grating, has a constant pitch. The blazed grating has the grating planes tilted with respect to the fiber axis. The chirped grating has an aperiodic pitch, presenting a continuous increase in the spacing between the grating planes.

1.5.1 Common Bragg reflector

The common Bragg reflector has already been illustrated in figure 1.7. It is the simplest and most used Bragg grating. Depending of the reflection spectrum shape, they may be utilized as narrowband transmission or reflection filter or a broadband mirror. In combination with others Bragg reflectors, they can be utilized as band-pass filters.

Bragg reflectors are considered excellent strain and temperature sensors, since all the information about these parameters are contained in the wavelengths reflected by the devise. This characteristic eliminates amplitude and intensity fluctuation problems that exist in others sensing system based in optical fibers (Othonos & Kalli 1999). Each Bragg reflector can be associated with a specific wavelength, therefore, several gratings can be written in the same fiber, each one with its respective wavelength. This configuration can be utilized for wavelength

division multiplexing (WDM) or quasi-distributed sensing (Kersey 1997). These gratings also proved to be very useful components in tunable fibers or semiconductor lasers (Ball, Morey & Glenn 1991), serving in one or both ends of the laser cavity.

1.5.2   Blazed Bragg Gratings

As previously stated, the main difference between a blazed Bragg gratings and a common grating reflectors is that, the first have the grating planes tilted, as can be seen in figure 1.10. This tilted structure will result in light that is guided in the fiber core being coupled into loosely bound, guided-cladding or radiation modes (Othonos & Kalli 1999). The angle of the grating planes and the amplitude of the refractive index modulation will determine the coupling efficiency and bandwidth of the light that is tapped out.
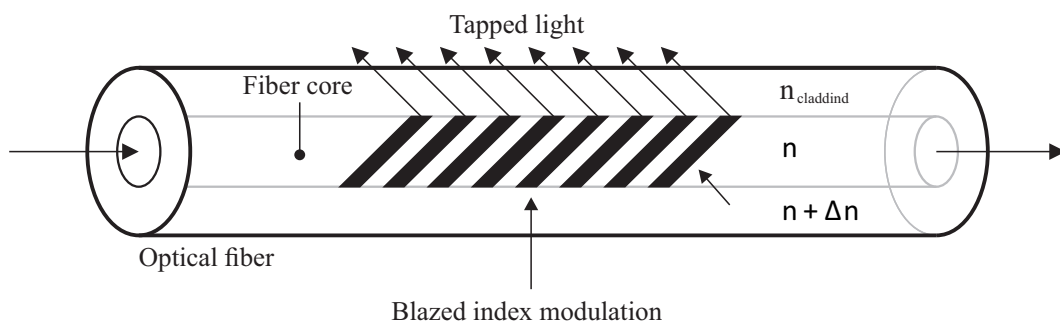
Figure 1.10: A Schematic diagram of a blazed grating tilted planes.

The Bragg condition must be analyzed with the same criteria of energy and momentum conservation that as seen in section 1.4, where $\vec{k_f} = \vec{k_i} + \vec{K}$ and $h \cdot f_i = h \cdot f_f$. Figure 1.11 shows the vector diagram of the Bragg condition for the blazed grating.
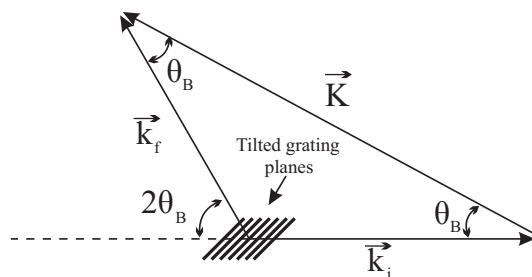
Figure 1.11: Vector diagram of a blazed grating Bragg condition.

The grating wavevector $\vec{K}$ is incident at an angle θ_B in relation to the fiber axis. The module of the incident, $\vec{k_i}$, and scattered, $\vec{k_f}$, wavevectors must be equal ($v = |\vec{k_i}| = |\vec{k_f}|$). With simple trigonometry relations, it is clear that the scattered wavevector are at an angle $2\theta_B$ with respect the fiber axis. The law of the cosines may be applied on the diagram of figure 1.11, which gives (Othonos & Kalli 1999)

$$|\vec{k_i}|^2 + |\vec{k_f}|^2 - 2|\vec{k_i}||\vec{k_f}| \cos{(\pi - 2\theta_B)} = |\vec{K}|^2 \qquad (1.24)$$

that can be simplified to

$$\cos\left(\theta_B\right) = \frac{|\vec{K}|}{2v}. \tag{1.25}$$

Equation 1.25 shows that the scattering angle is restricted by the Bragg wavelength and the effective refractive index (Othonos & Kalli 1999). According to (Dong, Zhang, Liu & Miao 2011), the Bragg condition can be expressed as

$$\lambda_B^{\text{co}} = 2n_{\text{eff}}^{\text{co}}\frac{\Lambda}{\cos\theta_B}, \tag{1.26}$$

where $n_{\text{eff}}^{\text{co}}$ is the effective refractive index of the core. Due to the existence of tilt angle, part of the forward propagating core mode light will be coupled into the counter-propagating cladding mode, resulting in resonance wavelength for the cladding mode given by (Dong et al. 2011):

$$\lambda_{B,i}^{\text{CL}} = \left(n_{\text{eff}}^{\text{co}} + n_{\text{eff,i}}^{\text{cl}}\right)\frac{\Lambda}{\cos\theta_B}, \tag{1.27}$$

where $n_{\text{eff,i}}^{\text{cl}}$ is the effective refractive index of ith cladding mode.

Due to the similarities of the Bragg center wavelength of FBGs and blazed FBGs, the core mode of blazed FBGs share the same sensing characteristics of a FBG sensor, including temperature and strain. However, for common Bragg reflectors, the cladding mode center wavelength is also influenced by effective refractive index of cladding modes, which is sensitive to temperature, strain, and fiber cross section.

Figure 1.12 shows the complex transmission spectrum of a blazed FBG with tilt angle of less than 5 degrees. The several peaks in the transmission spectrum is the result of the co-existence of core mode and cladding mode in blazed FBGs. The center wavelength of the core mode occurs in greater wavelengths while the cladding mode resonance peaks are located in shorter wavelengths. It is also evident the appearance of a ghost mode peak in the transmission spectrum (Dong et al. 2011).
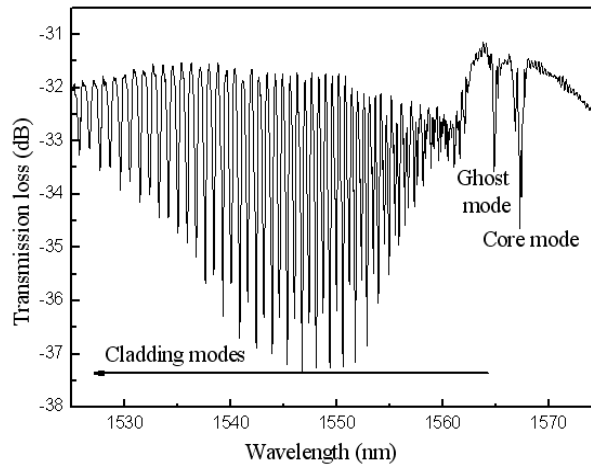
Figure 1.12: Transmission spectrum of a blazed FBG with tilt angle of less than 5 degrees (Dong et al. 2011).

Blazed Bragg grating with its complex mode coupling possess distinguished characteristics which could be employed to develop new photonic devices that could be used in optical sensing and communications applications. Various sensing application using blazed FBGs are cited in (Dong et al. 2011).

1.5.3 Chirped Bragg gratings

Chirped Bragg gratings posses a monotonically varying pitch, Λ, along the fiber core, as can be seen in figure 1.13. Some properties of the chirped profile are considered advantages in specific applications of telecommunications and sensor technology, such as dispersion compensation and stable synthesis of multiple wavelength sources (Othonos & Kalli 1999). Chirped gratings can be fabricated either by varying the grating period or the effective index of refraction or both.
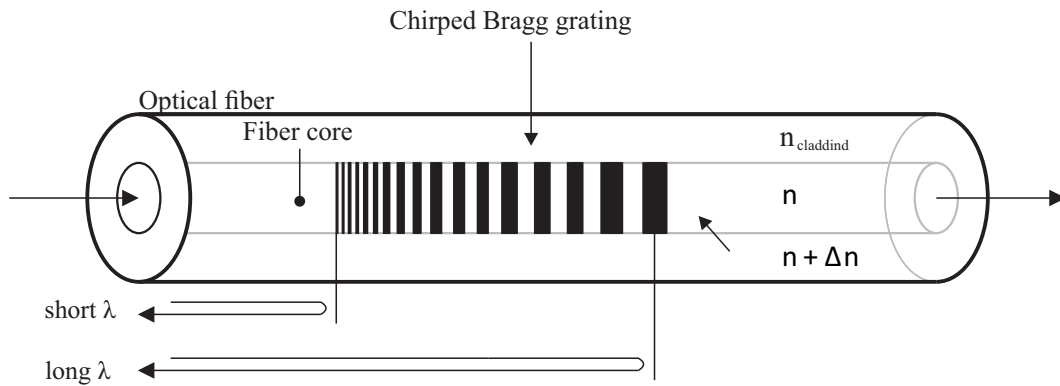
Figure 1.13: Schematic diagram of a chirped Bragg grating with an aperiodic period.

Therefore, the Bragg condition of a chirped Bragg grating is given by

$$\lambda_B(z) = 2n_{\text{eff}}(z)\Lambda(z). \tag{1.28}$$

Accordingly to (Othonos & Kalli 1999) the simplest type o chirped grating is the one where the variation of the pitch is linear such as $\Lambda(z) = \Lambda_0 + \Lambda_i z$, where Λ_0 is the starting pitch and Λ_i is growing rate of the period. This grating acts as if it were formed by a series of smaller length uniform Bragg gratings, increasing in period along the fiber core. Therefore, a chirped Bragg grating can be utilized as a broadband reflector.

Chapter 2

Demodulation of fiber Bragg gratings sensors

L IGHT signals from optical sensors, such as fiber Bragg gratings, must pass through an optical circuit that ends in a transducer, so that the sensing information may be read in a electronic circuit, where it can be easily processed and monitored. Demodulation of the optical signal have been a study object of several individuals and institutions around the world, aiming low cost systems with good resolutions and accuracy, trying to make the optical sensing field more popular.

For temperature and strain a wavelength resolution of approximately 1 pm is required to identify a temperature and strain change of approximately 0.1°C and 1 µε, respectively. Therefore, accurate measurements are needed to achieve a good sensor performance. Equipments such as optical spectrum analyzers (OSA) and tunable lasers may achieve this wavelength resolution, but makes the system very bulk and expensive. There is, in the literature, a increasing number of FBG interrogation topologies that tries to achieve higher resolutions with less expensive optical and electronic instruments.

This chapter describes some interrogations techniques existing in the literature and in the market in order to make a comparison between these systems and the newly proposed interrogation technique of this work.

2.1   Demodulation techniques

Demodulation of fiber Bragg gratings sensors may be done by several different techniques. The simplest method utilizes a optical spectrum analyzer (OSA). This methodology is very used in laboratory for preliminary experiment analyzes or calibration of the FBG sensors. However, spectrometers are very expensive. An OSA that delivers 1 pm of resolution may cost tens of thousands of dollars. Moreover, conventional OSAs are relatively very large preventing their use in practical applications (Othonos & Kalli 1999, Zhao & Liao 2004).

The ability to identify center wavelength shifts of Bragg grating sensors with high resolutions and without the use of expensive spectrometers have been wildly studied. The majority of the demodulation schemes make use of interferometers, passive and active filters (Tunable FBGs, Acousto-optic tunable filter, and Fabry-Perot tunable filter), tunable narrowband light sources, parallel detection using charge-coupled devise (CCD) and time-domain detection (Othonos &

Kalli 1999, Zhao & Liao 2004).

The most fundamental way to interrogate a Bragg grating sensor consists in the use of a broadband light source that illuminates the sensors. The spectrum of the light source must cover all the operating region of the sensors when they are exposed to a external perturbations. The reflection profile of the sensors is then directed to a wavelength detection system (Othonos & Kalli 1999). The reflected light usually reaches the detection system through an optical coupler, but in some cases an optical circulator is used. Optical circulators are more expensive but bring some advantages to the system, such as high isolation of the input and reflected optical power and its low insertion loss.

This basic reflectometric configuration is illustrated in figure 2.1. All demodulations techniques that will be analyzed in the next sections makes use of this reflectometric configuration. This configuration is also the basic WDM (wavelength division multiplexing) technique that will discussed further in this chapter in section 2.2.1. Tunable narrowband sources can also be used in a similar configuration simplifying the detection system to a single broadband power meter like a photodiode.

(a) Using optical coupler.

(b) Using optical circulator.
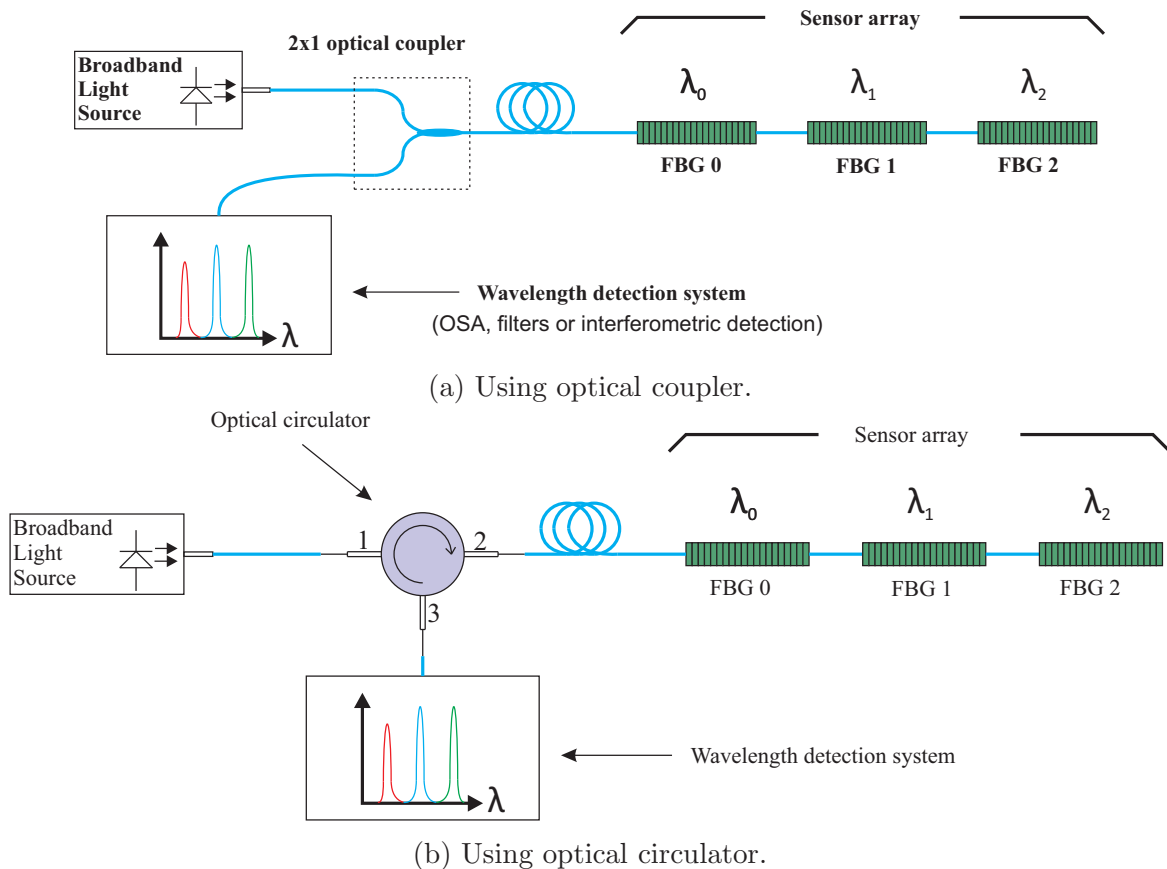
Figure 2.1: Basic reflectometric Bragg grating demodulation configurations. A broadband light source illuminates the sensor array and the reflection signal is directed to a wavelength detection system through an optical coupler (2.1a) or circulator (2.1b).

When using a tunable filter as a detection method, its spectral bandwidth is, in most of the cases, approximately equal to the sensor bandwidth, see figure 2.2. Examples of tunable

filter demodulation configurations, such as tunable Fabry-Perot (FP) filter (Kersey, Berkoff & Morey 1993, Allan, Graham, Zayas & Roach 2009), acousto-optic tunable filter (AOTF) (Xu, Geiger, l. Archambault & Reekie 1993), and Bragg grating-based tunable filters (Jackson, Ribeiro, Reekie, & Archambault 1993) have all been demonstrated. In all these cases the output signal measured by the broadband detector is the convolution of the tunable filter spectrum with that of the FBG sensor, and maximum output signal will occur when the spectrum of the filter matches that of the grating. If this point of maximum convolution and wavelength position are continually measured the center wavelength shifts of the sensor can be obtained(Zhao & Liao 2004). This demodulation configuration has a relatively high resolution and a large full-scale range, and is one of the most successful and attractive demodulation configurations (Othonos & Kalli 1999).
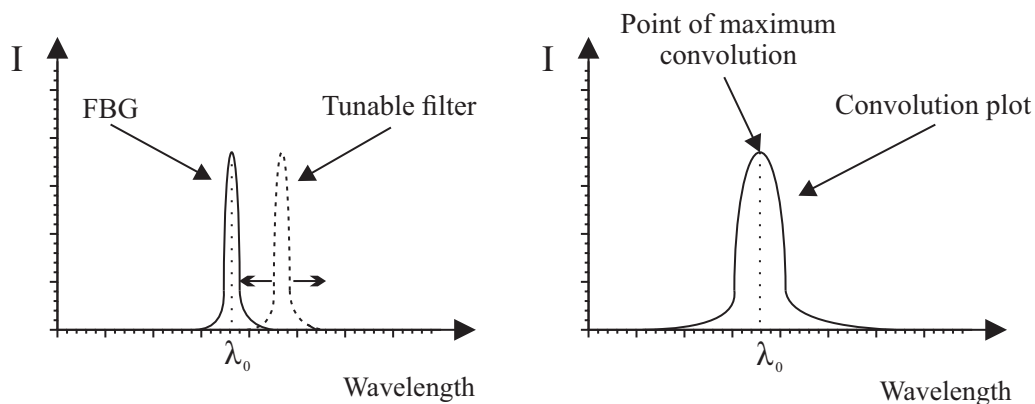
Figure 2.2: Principle of the tunable filter method. When the spectrum of the filter matches that of the grating, the point of maximum convolution occurs. Center wavelength shifts, caused by external perturbations, may be detected by tracking the point of maximum convolution.

2.1.1   Wavelength demodulation using a reference filter

The principle of operation of an interrogation system that makes use of an edge filter as a reference is illustrated in figure 2.3. By measuring the optical power intensity through the broadband detector the spectral position of the sensor (central wavelength), determined by the external conditions, can be obtained. The filter may have specific desirable optical characteristics for the system. For a higher full-scale range the filter must have a larger spectral bandwidth, losing sensibility. For higher resolutions the system must have a narrower filter bandwidth. This approach offers several advantages, such as low cost and easy operation, being very satisfactory for single point applications.

An example of such system is illustrated in figure 2.4, where a broadband light source illuminates the Bragg grating sensor S_1 and the reflected light is divided in two identical parts by a optical coupler, Ocp_2. The first half pass through the edge filter and is detected by a photodiode generating the measurement signal, I_S. The second half of the reflected light is
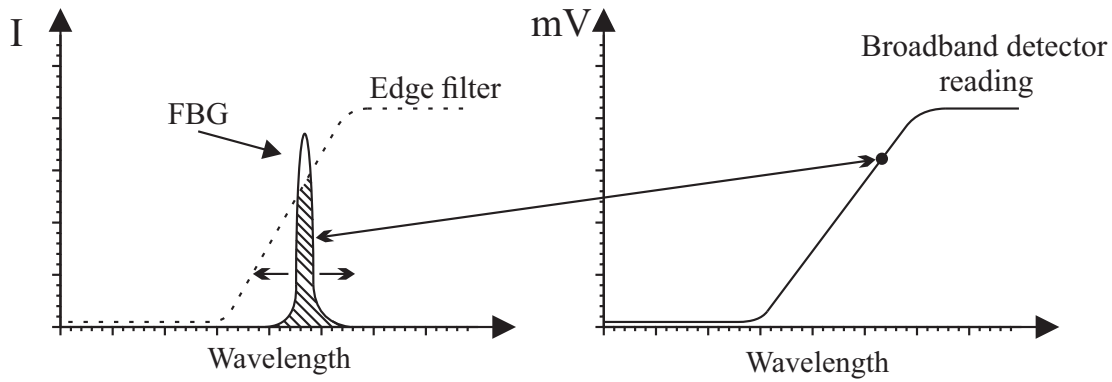
Figure 2.3: Operation principle of the edge filter method. By measuring the optical power intensity through the broadband detector the central wavelength of the sensor can be obtained.

directly captured by a second photodiode generating a reference signal, I_R. This reference signal can be used to compensate variations of the light source or bend losses.
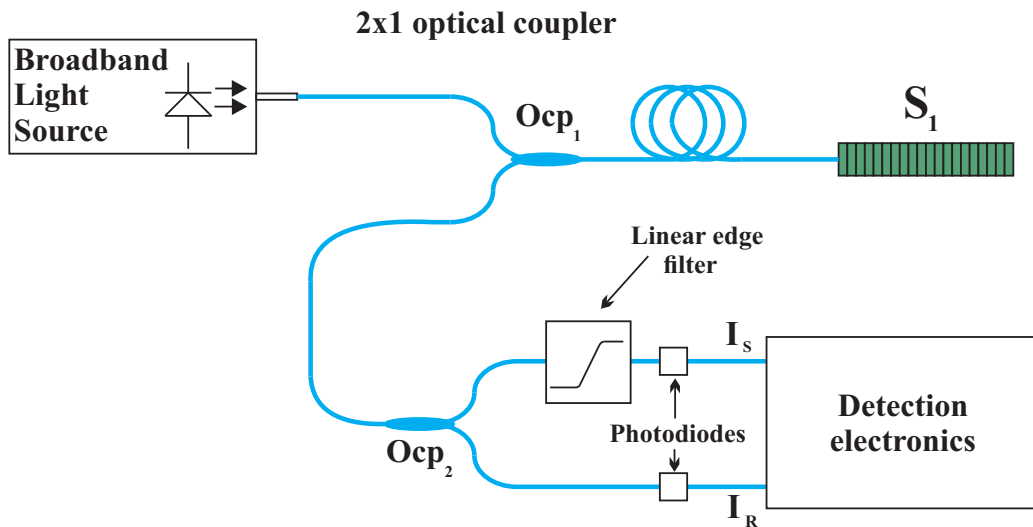
Figure 2.4: Example of an edge filter demodulation scheme (Melle et al. 1992).

The system that uses one reference filter may be improved adding another reference filter, in such a way to obtain a higher dynamic range (Nunes, Valente & Braga 2004). The optical scheme of this system is shown in figure 2.5. The sensor is illuminated by the broadband light source (LED), and its reflection passes through an optical coupler (Ocp) that makes the reflected light pass through two filters. The transmitted light of the two filters are detected by two photodiodes (D_1, D_2). The ratio between the optical power detected by the two photodiodes (P_{D_1}/P_{D_2}) is immune to any intensity variation of the system, being sensitive only to spectral variations of the sensor.

Fallon et al. (1993) developed a system that makes use of chirped Bragg grating as a reference filter to interrogate another identical chirped Bragg grating for large strain sensing applications. The basic experimental arrangement of this system is illustrated in figure 2.6. The identical chirped grating interrogation (ICGI) system makes use of a broadband light source, two optical couplers (Ocp$_1$, Ocp$_2$), two identical chirped gratings and two photodiodes (D_1, D_2).
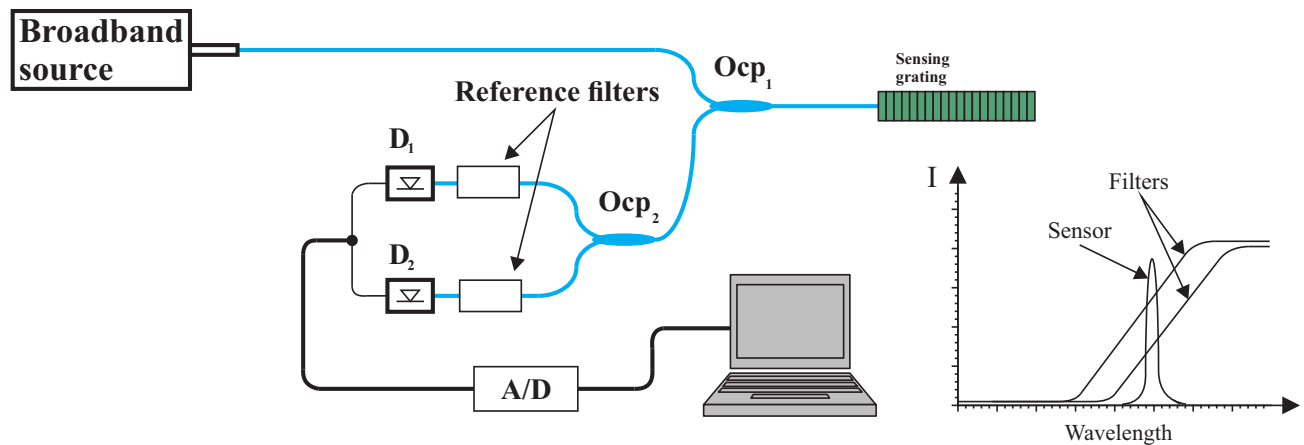
Figure 2.5: Demodulation scheme using two reference filters (Nunes et al. 2004). The ratio between the optical power detected by the two photodiodes is immune to any intensity variation of the system.
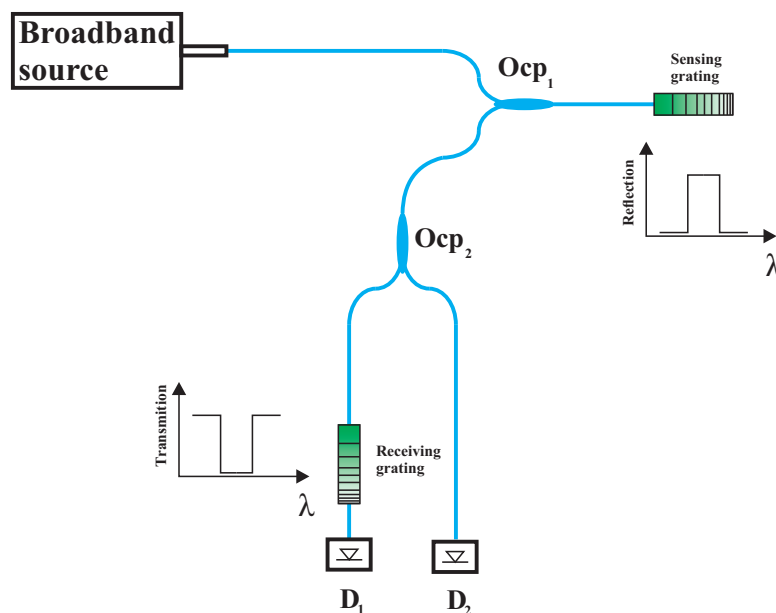
Figure 2.6: Basic experimental arrangement for a ICGI system (Fallon 1997).

The sensor is illuminated by the broadband light source via Ocp_1. The sensor reflected light enters in the second coupler Ocp_2 and is divided in two equal parts. Half of the light is transmitted through the reference grating reaching the photodiode D_1 an the other half reaches the photodiode D_2. D_1 measures the light transmitted from the reference grating while D_2 detects time-varying intensity and spectral variations of the light source to be compensated in the final strain calculation. The reference grating acts like a rejection filter and if both sensor and reference gratings are under zero strain, then, the light detected by D_1 will be minimal. If the sensor is stretched, its spectral profile is linearly shifted and the two reflection bands of the two gratings no longer completely overlap and some light is transmitted to D_1. The result is a liner dependency of the strain applied over the sensor grating and the light power detected by the photodiode. The strain resolution reached by this system was approximately 4 $\mu\varepsilon$ (which

is equivalent to 4 pm at 1300 nm) in a full scale range of 12,000 µε. However, to this system works properly the temperature of the reference grating must be kept constant.

2.1.2   Wavelength demodulation using tunable a Fabry-Perot filter

The Fabry-Perot filter (FPF) is an optical resonator that confines and stores light energy at selected frequencies. The filter transmission is characterized by bandpass resonances which has the approximate shape of a Lorentzian function and bandwidths of typically 0.3 nm (Othonos & Kalli 1999). The operating range of a FPF can reach tens of nanometers. The filter tuning is achieved by changing the cavity spacing, e.g., using a piezoelectric element.

Allan et al. (2009) reports a multi-point interrogation system for FBG strain sensors based on a microelectromechanical (MEMS) Fabry-Perot tunable filter. The filter is controlled using an embedded digital signal processor (DSP) which implements a correlation algorithm to detect shifts of the central wavelength of each sensor, providing real-time strain readings. The block diagram of this system is shown in figure 2.7.
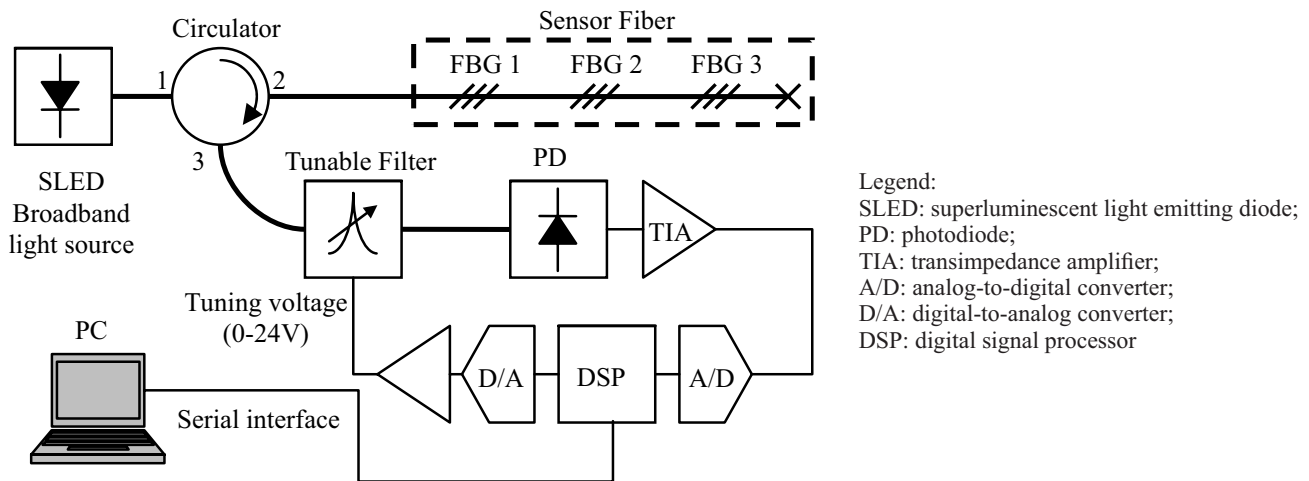
Figure 2.7: Interrogation block diagram using a tunable FPF (Allan et al. 2009).

A fiber-coupled superluminescent light emitting diode (SLED) is used as broadband light source. Light from the SLED passes through a three-port optical circulator reaching a FBG strain sensor array. Wavelength division multiplexing (WDM) is used to allow the various FBG sensors to be detected in the same fiber, i.e., each sensor has a different center wavelength, sufficiently separated to allow the detection of individual sensors within their operating range. The reflected light from the sensor array passes through the MEMS tunable filter, and is detected by a photodiode. The signal from the photodiode is digitized with an analog-to-digital converter (ADC) and processed by a DSP. The DSP uses a digital to analog converter (DAC) to generate a tuning voltage, sweeping the center wavelength of the tunable filter over the desired wavelength range, allowing the measurement of each individual sensor.

This scheme may be used to operate in either scanning mode or tracking mode (closed-loop). In the scanning mode a voltage ramp must be applied in the input of the tunable FPF. The ramp and photodetector voltages are simultaneously recorded, allowing the continuous detection of the individual center wavelengths of the sensors by each ramp period. Allan et al. reported

a scanning speed of 0.1 nm/µs, allowing the reflection spectrum from six FBGs spanning a 30 nm wavelength range to be measured in 0.3 ms with a 1.5 pm resolution.

In tracking mode the system is limited to addressing one FBG. In this closed-loop configuration the signal acquired in the detector is used to generate a control signal that is applied on the input of the tunable FPF to track the sensor center wavelength. Kersey et al., using a similar system, reported a resolution of approximately 1 pm over a working range in excess of 40 nm for a single FBG.

2.1.3   Wavelength demodulation using acousto-optic tunable filters

The acousto-optic tunable filter (AOTF) is a solid-state optical filter which is driven by RF frequencies, i.e., the applied RF frequency generates a transmission spectrum which center wavelength is proportional to the input frequency. The AOTF can be driven at multiple wavelengths simultaneously by applying multiple RF signals of different frequencies, allowing parallel interrogation, making this devise very attractive for FBG interrogation systems. The AOTF covers a large wavelength range that can extend to several micrometers (Othonos & Kalli 1999).

Like FPF systems, demodulation schemes that uses AOTF may operate in scanning or tracking modes to detect the shifts of the FBG center wavelength. In scanning mode a PC drives the AOTF using a voltage-controlled oscillator (VCO) over the wavelength of interest, recording the power of the reflected light that reaches the broadband detector. In tracking mode the system tracks the instantaneous wavelength of a specific FBG using a feedback loop.
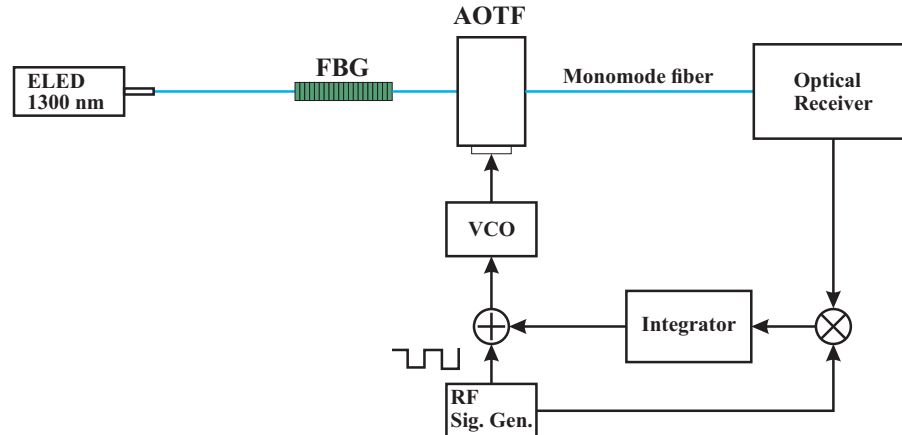
Figure 2.8: Schematic of a Bragg wavelength tracking loop using AOTF (Xu et al. 1996).

Xu et al. (1996), in a practical demonstration of an interrogation system using AOTF achieved a noise-limited strain resolution of 0.26 µε or 0.31 pm in wavelength. The system is represented in figure 2.8. To track the central wavelength of the FBG sensor a frequency-shift-keyed (FSK) signal is applied to the AOTF, resulting in a square-wave amplitude modulation of the transmitted light, where amplitude of the modulated signal is a function of the difference between the grating and the AOTF central wavelengths, and its polarity depends on the relative position between the FBG and the AOTF. The AM light signal is detected by an optical receiver and then multiplied by the modulating signal, integrated, and finally added to the modulating signal, thereby controlling the central wavelength position of the AOTF to track the grating

wavelength. When the central wavelength of the AOTF reaches the granting wavelength, the amplitude modulation of the light at the dither frequency will be zero. The grating wavelength can be monitored by the mean RF frequency that determines the AOTF central wavelength.

One of the most notable advantages of the AOTF is the possibility track simultaneously various FBG sensors in the same fiber, using a single filter and broadband detector. To that end, Volanthen et al.(1996) and Boulet et al. (2001) have demonstrated a simultaneous monitoring of two Bragg grating sensors. The experiment performed by Volanthen et al. produced a rms error of 2 µε or 2.4 pm for both gratings.

2.1.4   Wavelength demodulation using tunable Bragg grating filters

Tunable Bragg gratings filters (TFBG) can be achieved by applying the grating in a stretching or heating element such as a piezoelectric material (PZT) or a thermo-electric cooler (TEC), respectively. Therefore, the center wavelength of the tunable FBG will vary accordingly to the equation 1.22.

A simple scheme of Bragg grating demodulation system using a TFBG was first demonstrated by Jackson et al. in 1993. The basic concept of this system is illustrated inf figure 2.9. Light from the broadband source is reflected by the sensor, G_{1S}, reaching the TFBG, G_{1R}, which is mounted on a piezoelectric stretcher. The central wavelength of the two gratings are identical if no strain is applied on the gratings. The center wavelength of the sensor will vary in direct proportion to the measurand and will generally not match that of G_{1R}. But if the central wavelength of G_{1R} is linearly swept over the sensor spectrum by driving the PZT, eventually the reflecting wavelengths will exactly match. When this occurs a strong signal will be detected by the photodiode. If a closed-loop servo is used to maintain the matched condition, the instantaneous value of the strain applied over the sensor can be detected by measuring the PZT voltage at that point, assuming that the voltage-to-wavelength constant of G_{1R} is known.
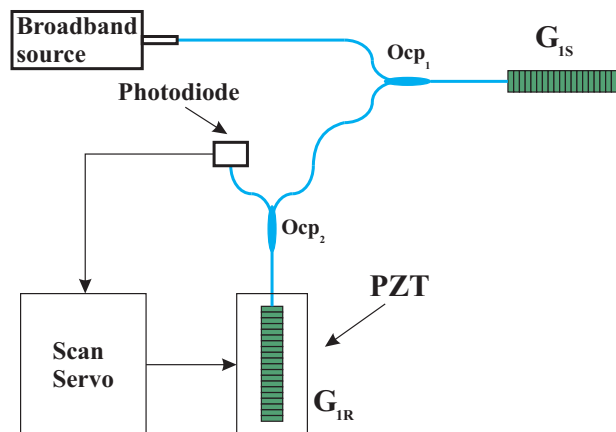
Figure 2.9: Basic concept of the sensor-receiving grating pair (Jackson et al. 1993). The broadband light source illuminates the sensor. The reflected spectrum reaches the TFBG and if the two gratings are matched at the same wavelength, the photodiode will identify a strong signal.

Figure 2.10 shows the experimental multiplexed system with two sensor-receiving grating pairs. By using this approach, Jackson et al. was able the achieve a resolution of 4.12 µε or 3.4 pm in each grating, which corresponded to the minimum induced strain necessary to destroy the matched condition. Brady et al. modified the parallel topology using a serial array of TFBGs reducing the number of optical components. The resolution obtained was 2.3 pm.
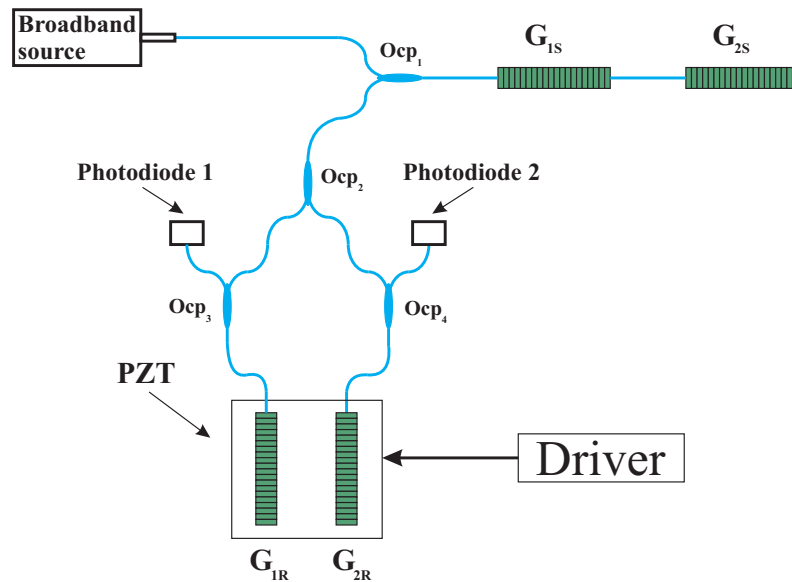
Figure 2.10: Experimental system with two sensor-receiving grating pairs. A resolution of 4.12 µε or 3.4 pm was achieved in each grating (Jackson et al. 1993).

Davis & Kersey (1995) developed a similar configuration as shown in figure 2.11. In this configuration light from a broadband source pass through a optical coupler to illuminate the sensing FBG array. The reflected light from the sensors pass through the receiving matched filter array and reach a photodiode. Each TFBG is mounted on separated small stretching devices driven by piezoelectric stacks, allowing independent tuning of the TFBGs.
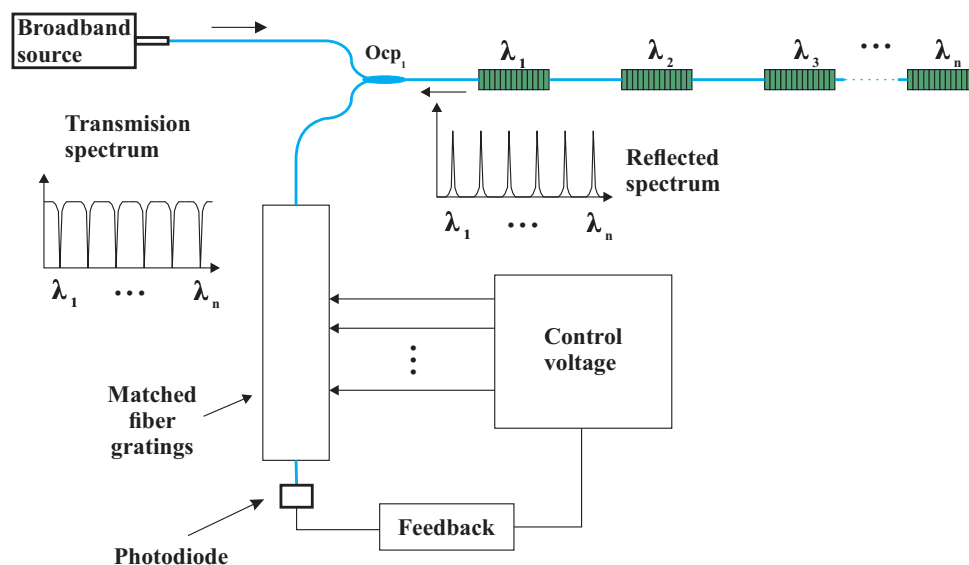
Figure 2.11: Experimental setup with TFBGs in transmissive mode (Davis & Kersey 1995).

To track the center wavelengths of the sensors a small dither signal is applied on the TFBGs. The signal detected by the single photodiode is fed to lock-in amplifiers, each one referenced to the dither signal of a specific TFBG. The outputs of the lock-ins is then summed with the dither signals and fed back onto the filter gratings. This feedback loop allowed the TFBGs track any shift in the center wavelengths of the sensing gratings.

2.1.5   Demodulation using tunable narrowband light source

Another configuration for Bragg grating demodulation uses a tunable narrowband light source that illuminates the sensor and a optical power meter (broadband detector) receives the reflected signal from the sensor (Othonos & Kalli 1999). In this type of system the maximum reflection occurs when the laser wavelength is in the same spectral position of the sensor. If the laser tuning is well calibrated it is possible to determine the spectral position of the sensor. Figure 2.12 show a block diagram of a single point system.
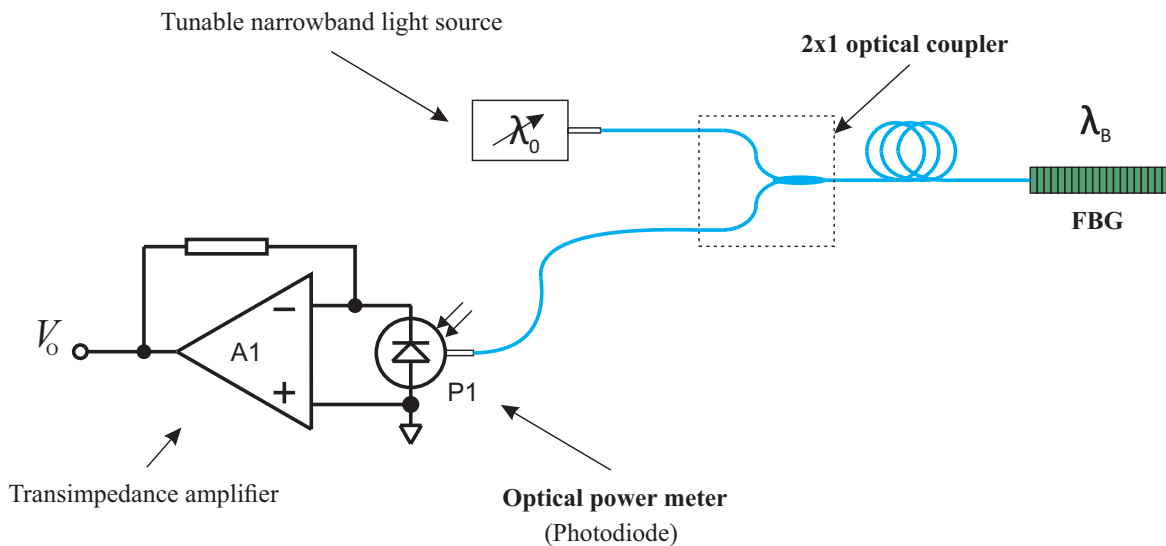
Figure 2.12: Optical circuit that uses a tunable narrowband light source and an optical power meter. The maximum reflection occurs when the laser wavelength is in the same spectral position of the sensor, being possible to determine the spectral position of the sensor.

A distributed feedback laser (DFB) can be used as a narrowband light source. Generally, this type of laser comes with an embedded thermoelectric cooler (TEC) that is used to tune the laser spectrum. The tuning range is usually of the order of 6 nm for a 50°C change in temperature. Altering of the current powering the laser will also tune the device, as a current change causes a temperature change inside the device. Less expensive models (few hundreds of dollars) comes with the tuning range around 2 nm allowing the interrogation of one or two gratings sensors, depending on the operation range of the sensors. Like tunable filters the laser can either sweep the grating spectrum or track the sensor wavelength in a closed-loop interrogation.

A system, proposed by Silva et al.(2013), uses a DFB laser to interrogate a FBG sensor in a quasi-static temperature measurement. A block diagram of this system is shown in figure 2.13. The DFB laser illuminates the sensor FBG_1 and a photodetector PD_1 receives the

sensor reflected spectrum. The current generated by PD_1 is converted in voltage by low noise transimpedance amplifier A_0. Therefore, the voltage V_{FBG} is proportional to the intensity of the reflected light. The temperature can be easily obtained by sweeping the laser over the sensor spectrum and searching for the center wavelength peak. The laser wavelength, λ_L, is calculated measuring the voltage V_{TH} from the resistive divider formed by R_L and the thermistor R_T which is inside the laser package. All this process is controlled by a microcontroler which features an internal ADC and DAC. When the system is turned on an algorithm makes the laser search for the grating peak. Once found the peak, the algorithm makes the laser sweep over the top flat part of the FBG reflection profile. So, every time that the grating center wavelength shifts due to temperature the algorithm establishes a new sweeping range to track the FBG reflection profile.
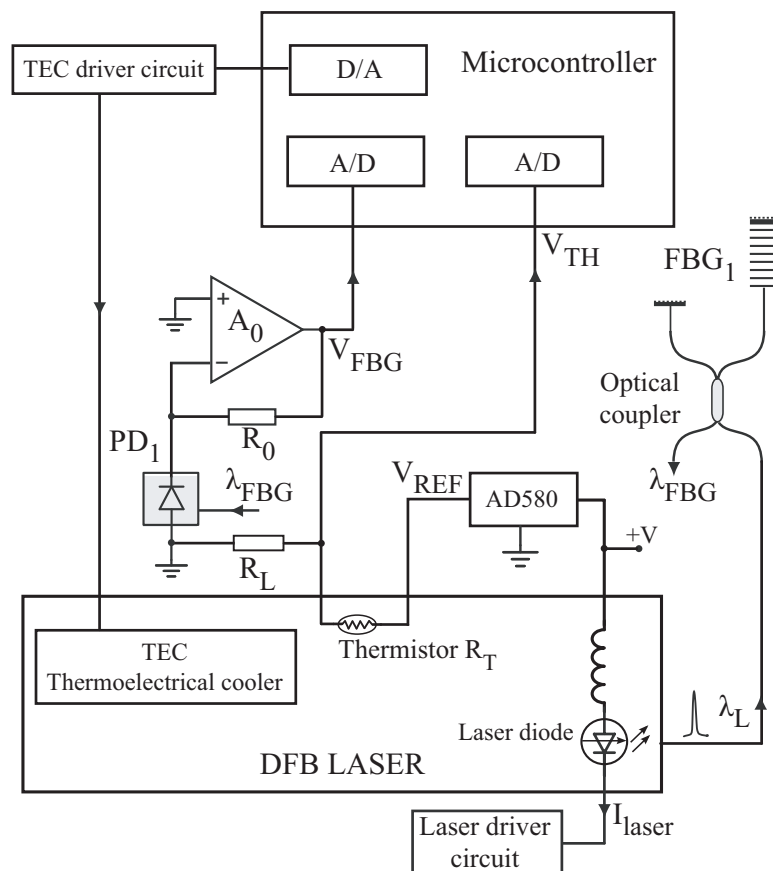
Figure 2.13: Block diagram of the interrogation system proposed by Silva et al. (Silva et al. 2013).

In another similar approach (da Costa 2009), the light reflected by the Bragg grating sensor is detected by a photodiode and the photo-induced current enters in a proportional-integral-derivative (PID) controller. This controller makes the laser wavelength tracks one of the two high slope regions of the sensor reflection spectrum, as can be seen in figure 2.14. The high slope region makes the controller much more responsive and stable to little center wavelength shifts when compared with the peak region of the grating, making the measurement very precise. This system was able to measure a range of 100°C with a maximum absolute error of 3.2%.
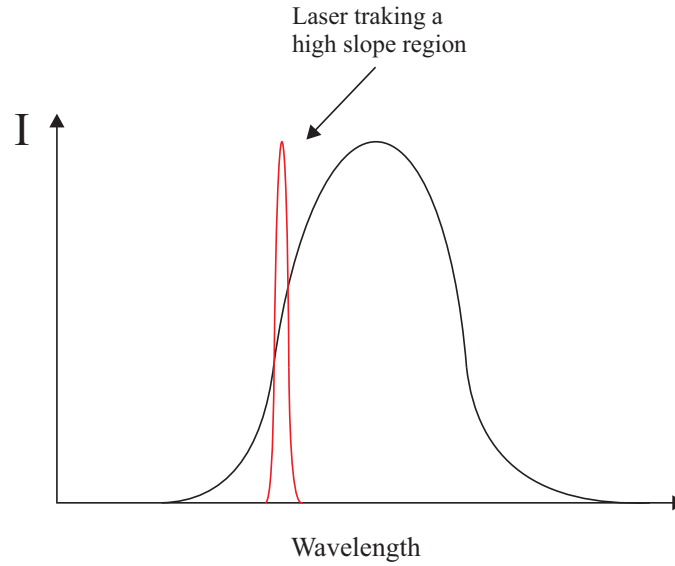
Figure 2.14: Tunable DFB laser tracking a high slope region of the sensor reflection spectrum.

2.2 Multiplexing techniques

In many real-world applications a large number of sensors is needed to achieve a distributed measurements of the parameters. This is the case of smart structures where sensor arrays are bonded or embedded into the materials to monitor the structure health (Yu, Yin & Ruffin 2010). Multiplexing brings a great advantage to optical sensors interrogation systems, since sharing the light source, optical components and processing electronics reduces dramatically the cost per sensor, making the system more competitive. FBG sensors have a great advantage over other sensors since many sensors can be interrogated through a single fiber. One may distinguish three main categories of fiber Bragg gratings multiplexing techniques: time division multiplexing (TDM), wavelength division multiplexing (WDM), and spatial division multiplexing (SDM) (Othonos & Kalli 1999).

The system developed in this work uses the a WDM configuration that will be described in the next section. The TDM and SDM configurations will be briefly presented.

2.2.1 Wavelength division multiplexing

WDM systems are the most popular approach and the most straightforward multiplexing technique (Yu et al. 2010). The basic WDM configuration was already shown in figure 2.1, where the reflected light from the sensors are fed into a wavelength detection scheme. In this type of system the sensors are distinguished through the wavelength, i.e. various sensors have the central wavelength spaced by a few nanometers. Each sensor is tracked as the center wavelength changes due to the environmental conditions such as strain, temperature, and pressure.

In early configurations presented in section 2.1, tunable filters (FPF, AOTF, and TFBG) were used to distinguish wavelength shifts of each FBG sensor in the array. When the tunable filter operates in scanning mode, multiplexed FBG sensors can be interrogated using the same broadband detector (Yu et al. 2010).

A parallel topology can be used, in the detection system, to allow simultaneous measurements of all the sensors in the array (Yu et al. 2010). Figure 2.15 shows a $1 \times N$ fiber splitter used to divide the optical power of the sensors reflected light into N channels. In each channel a matched TFBG detects wavelength shifts from the specific FBG sensor. In this scheme each TFBG receives less than $1/2N$ of the reflected power, as a result of using the $1 \times N$ splitter. Therefore, adding more channels reduces the power of each individual channel.
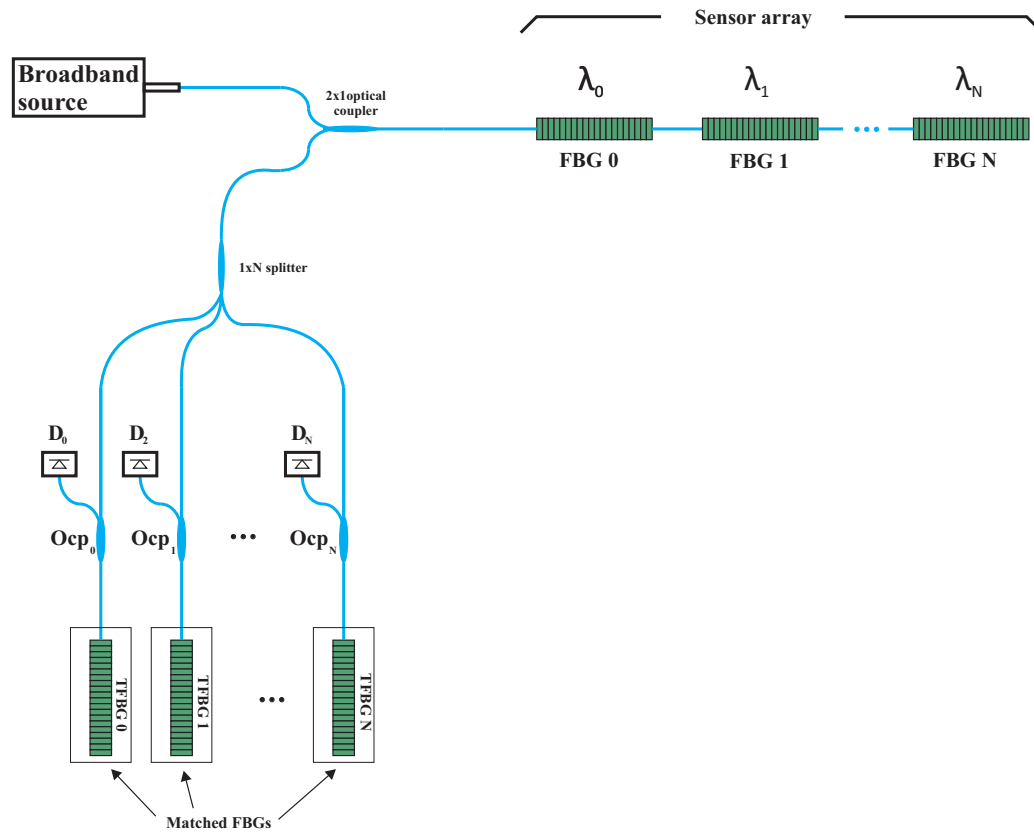
Figure 2.15: TParallel detection topology of a WDM system (Yu et al. 2010).

A improved scheme, proposed by Brady et al., uses a serial configuration as shown in figure 2.16. The optical power of the serial scheme is used more efficiently than the parallel topology. However, a large power reduction still exists through the use of the reflection of the matched TFBG.
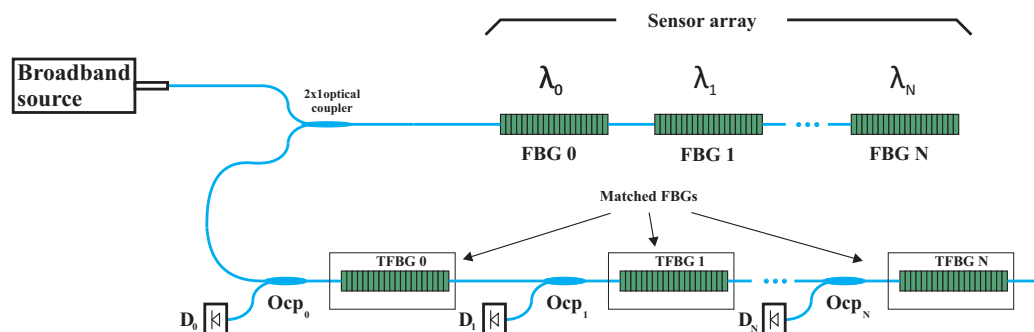

Figure 2.16: Serial detection topology of a WDM system (Brady et al. 1994).

The system proposed in this work makes use of an alternative serial topology as can be seen in figure 2.17. This configuration maximizes the power of the reflected light that enters in the detection system by using an optical circulator. The detection of the photodiode is reflective. Each optical coupler divides the reflected light into two parts. The first part represents 1% of the reflected light of the sensor array and reaches the matched TFBG where the light is reflected to be detected by a photodiode. The second part of represents 99% of the reflected light and it is transmitted to the next optical coupler. If fifty sensors are placed in this configuration less than 60% of the reflected signal from the sensors still reaches the last optical coupler, which is more than enough to perform the measurements.
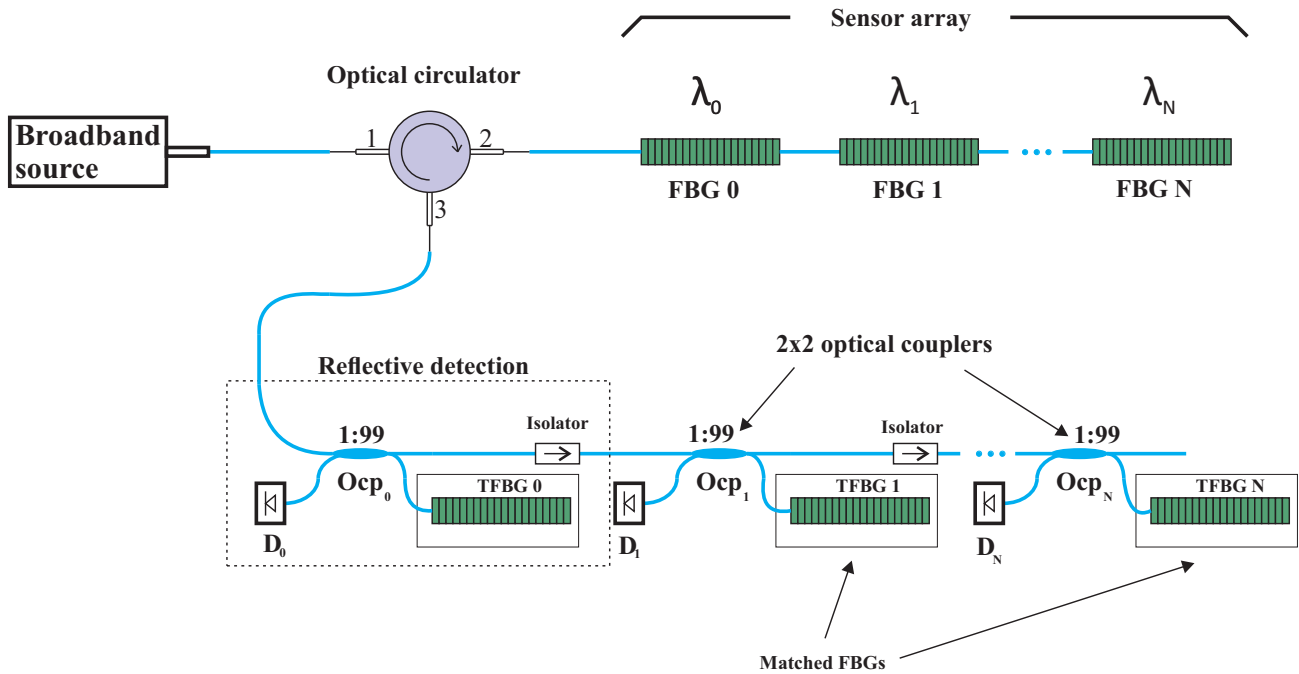
Figure 2.17: Serial detection topology of the proposed system system.

In WDM systems the available number of multiplexed FBG sensors depends on the measurement range of the sensors and the bandwidth of the gratings (Yu et al. 2010). However, reducing the bandwidth of the gratings also reduces the available optical power from each sensor, degrading the system performance.

2.2.2 Time division multiplexing

TDM systems distinguishes each sensor placed in the same optical fiber by measuring the required time to a light pulse be back-reflected to the detection system. In this type of interrogation system all sensors are written with the same center wavelength λ_B and low reflectivity, allowing a considerable portion of the light reach each sensor. Theoretically, 100 or more FBGs can be on the same fiber at the same nominal center wavelength (Graver 2008). Depending on the changes of the environmental conditions, the temporal signature of each sensor also changes. TDM systems translate this changes in the parameter of interest, such as strain or temperature. In TDM systems there is a trade-off between the sampling rate and the distance of the light

source to the sensor and the detection system. Lower distances need higher sampling rates. The distance between the sensors must be, typically, greater them a few meters to distinguish clearly adjacent sensors (Zhou, Graver, Hsu & ping Ou 2003). Figure 2.18 shows a basic TDM schematic diagram and the operating principle.
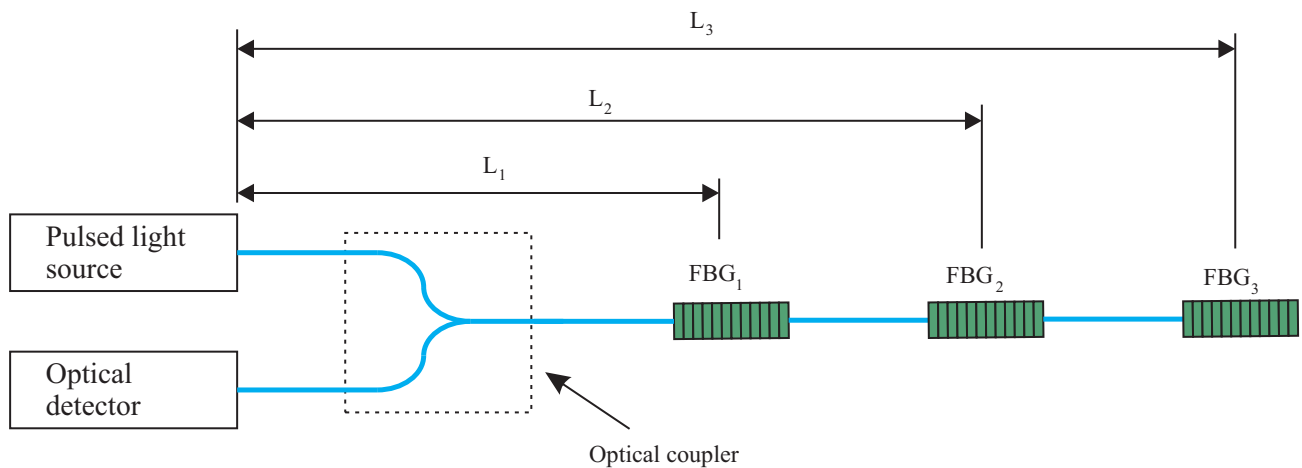
(a) Pulses from light source pass through the optical coupler, which is also connected to detector, to the fiber containing FBG sensors.
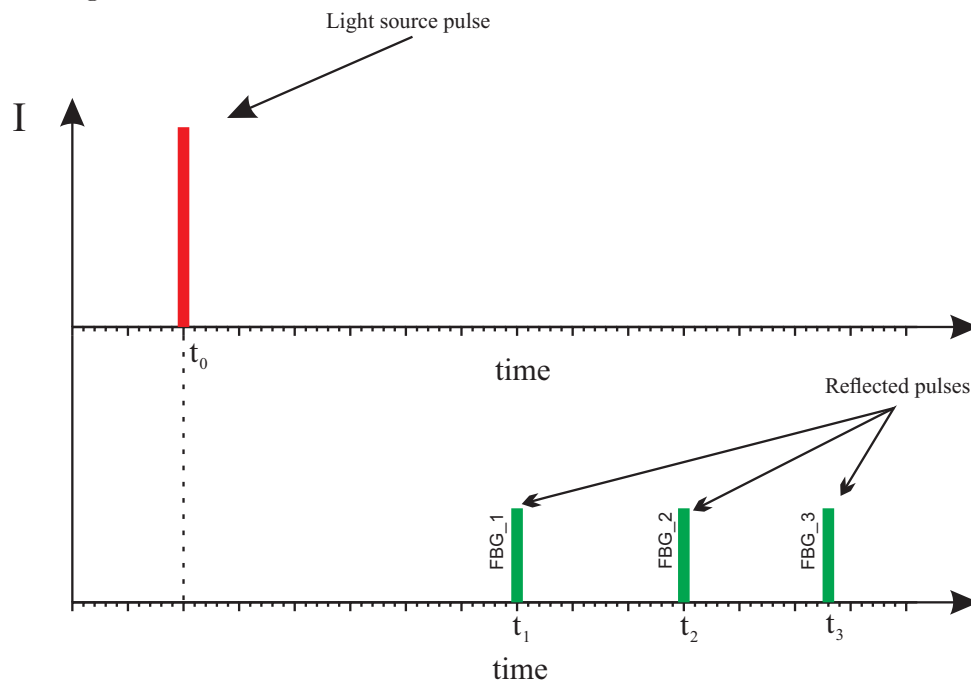
(b) Pulses emanating from source at time t_0 are reflected from the sensors, and return at t_1, t_2 and t_3.

Figure 2.18: Schematic and operating principle of a TDM equipment.

One example of commercial interrogation system that uses TDM technology is a module developed and fabricated by Moog Insensys Limited that commercializes optical monitoring solutions applied in the wind industry of the United Kingdom (Rhead 2008). Their module OEM-3030 (Epsilon 2013) is capable of interrogate 100 FBG sensors with resolution around 1.5 pm at a sampling rate up to 10 kHz.

2.2.3 Spatial division multiplexing

The multiplexing techniques described in previous sections are ideal for applications where distributed sensing is needed. In some cases, however, point measurements are required where FBG sensors in a network need to be operated independently, interchangeable, and replaceable without substantial calibration (Othonos & Kalli 1999). This requires identical characteristics of the FBG sensors in the network. A spatial division multiplexing (SDM) configuration is based in a parallel sensor topology, being ideal for the aerospace industry and security applications.

Figure 2.19 shown a schematic of a SDM configuration (Yu et al. 2010). A super-luminescent-diode (SLD) is used as a broadband light source, a Michelson interferometer as a wavelength scanner, and several FBGs with the same nominal Bragg wavelength and FWHM as sensor elements. The reflection of each sensor is detected separately by different photodiodes. The center wavelength interrogation of the grating sensors are based on interferometric phase measurement (Yu et al. 2010). A system with 32 FBG sensors using a SDM configuration has been demonstrated in (Rao, Kalli, Brady, Webb, Jackson, Zhang & Bennion 1995). To reduce the cost per channel the SDM configuration is often combined with another multiplexing configurations (Davis, Bellemore, Putnam & Kersey 1996, Rao et al. 1995, Rao, Jackson, Zhang & Bennion 1996).
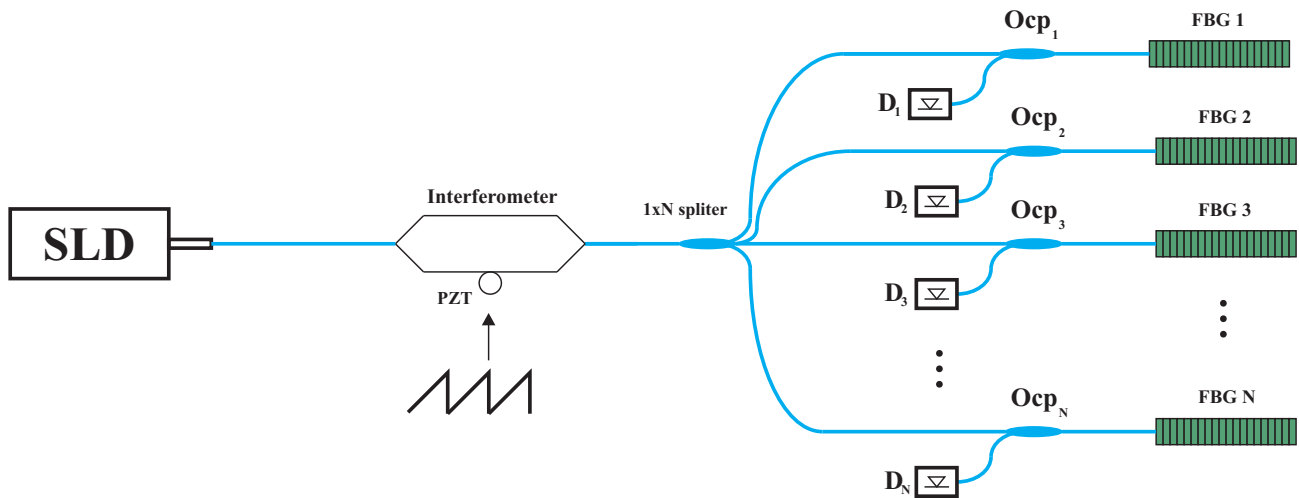
Figure 2.19: A spatial division multiplexing configuration (SDM) using a fiber splitter and several photodetectors.

A novel SDM method is using the fact that reflection spectrum of a low-reflectivity Bragg grating is the Fourier transform of its spatial structural variation (Froggatt 1996). Optical power from a tunable laser is coupled into a sensing array built with several low reflection fiber Bragg gratings and with the same center wavelength, as can be seen in figure 2.20. The scanning of the tunable laser leads to the measurement of the reflected power from the sensing array as a function of wavelength. The Fourier transform of this data gives reflected power as a function of distance from a reference air gap reflector located at the beginning of the sensor array. The reflected power as a function of distance can be used to select the specific data of a single Bragg grating sensor located in the sensing array. An inverse Fourier transform is applied in the selected data to recover the reflection power as a function of wavelength of the sensor being

interrogated. A similar system with 12 FBG sensors has been demonstrated in (Wood, Brown, Rogowski & Jensen 2000).
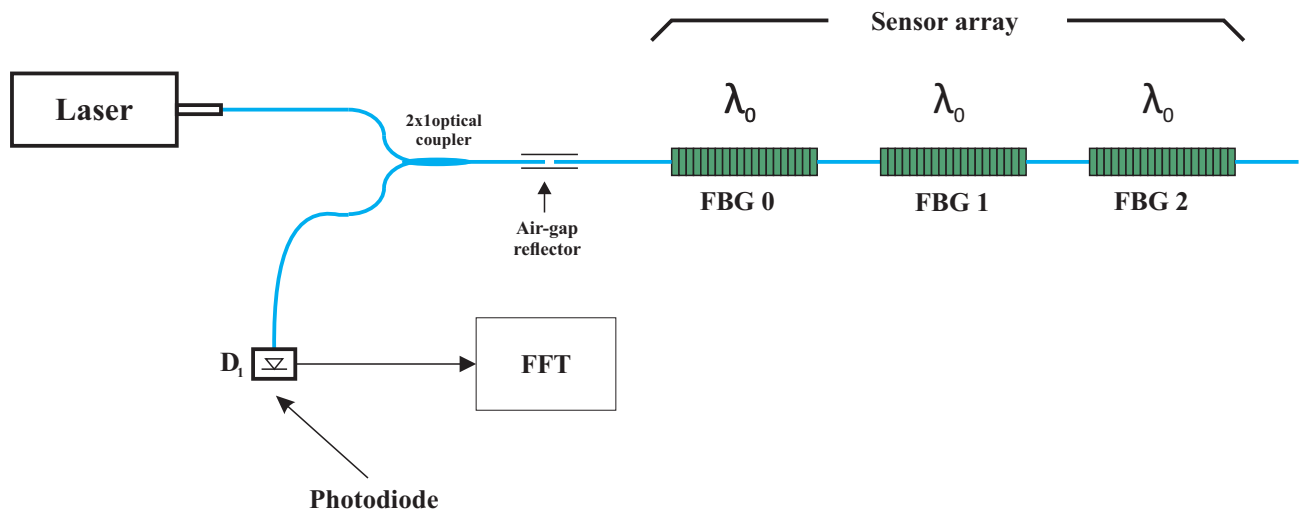
Figure 2.20: SDM system based on Fourier transform.

2.3   The proposed interrogation technique

This section will describe the proposed closed-loop interrogation technique. The system developed for this thesis is based in the application of tunable FBG filters, described in section 2.1.4, and the serial multiplexed scheme exposed in section 2.2.1. It also features compensations against optical power fluctuations of the light source, insertion loss, and bend losses. The great differential of this work is the individual control of each TFBG to track the center wavelength of the respective grating sensor placed in the array. Therefore, each channel is controlled by a simple electronic module composed of a microcontroller, a transimpedance amplifier to read the photodetector signal, and a power amplifier to drive a thermo electric cooler (TEC), used to tune the TFBG.

2.3.1   Overview of a single point system

Firstly, consider an interrogation system with only one FBG sensor. A block diagram of this system is shown in figure 2.21. The system uses a broadband light source that illuminates the FBG sensor through the port 1 of the optical circulator. The FBG sensor receives the light through port 2 and reflects light back according to its reflection profile. The reflection returns via port 2 and exits through port 3 being divided in two by the optical coupler. Half of the light signal is read by the photodiode P2, and the other half reaches a TFBG.

To allow the tuning, the TFBG is placed over a TEC inside a thermal chamber where temperature may be controlled and monitored through an electronic temperature sensor. The center wavelength of the TFBG must be approximately matched with the sensor FBG, in such a way that when the light signal reaches the TFBG occurs another reflection that returns via the optical coupler and reaches the photodiode P1. The luminous power read by the photodiode P2

represents the power reflected by the sensor FBG, and should remain constant independently of the temperature (Lima, Antunes, de Lemos Pinto & Nogueira 2013).
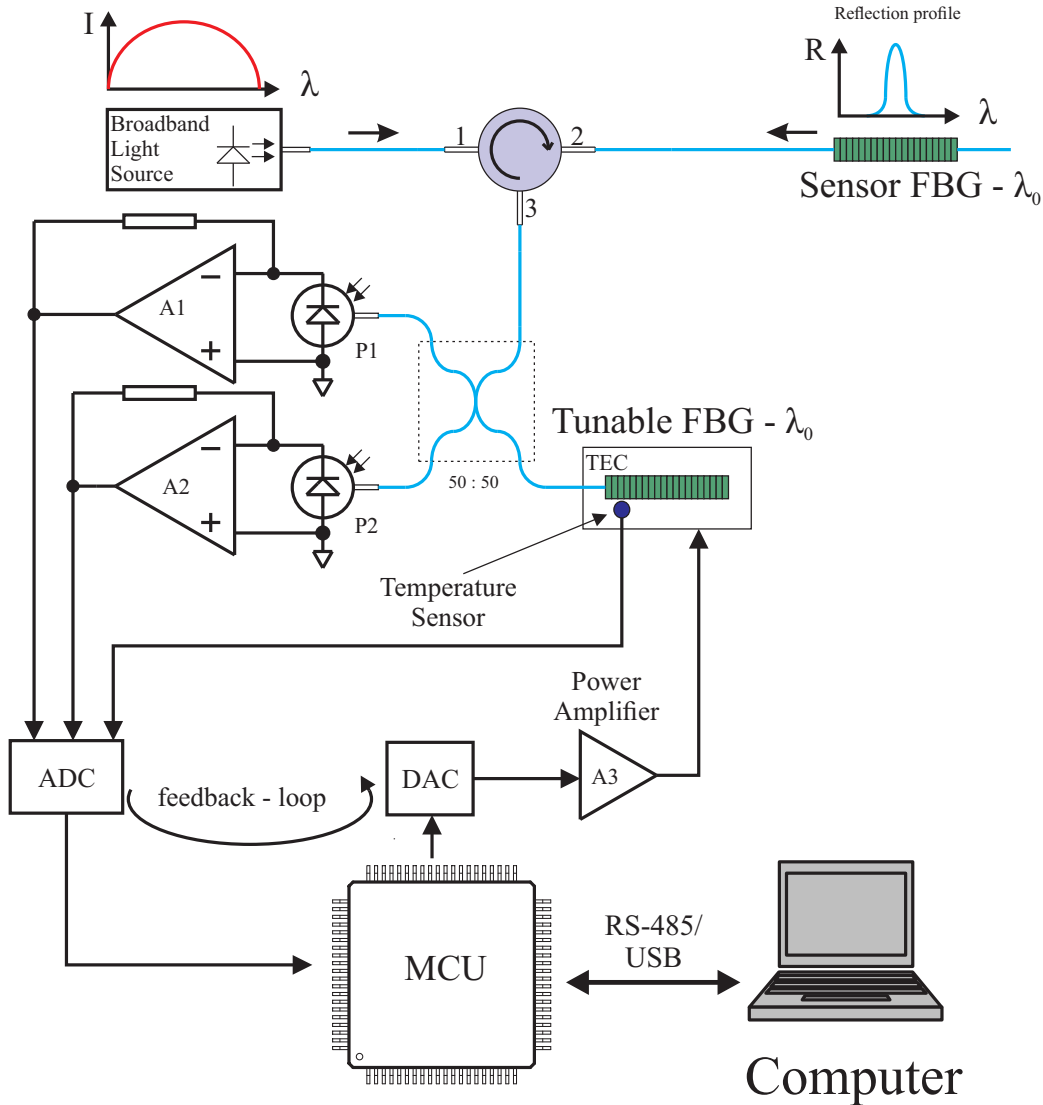
Figure 2.21: The block diagram for a single-sensor interrogation system.

Mathematically, the signal of P1 represents the convolution between the refection profiles of the sensor and the TFBG in a given temperature difference ΔT between then. Figure 2.22 shows an illustration of two matched FBGs that have the same central wavelength (λ_0) in a given temperature T_0. This figure also assumes that the sensor FBG stays in a constant temperature T_0 and that the TFBG can vary the temperature by a portion ΔT. The hatched area represents the optical power that reaches P1 (a point in the convolution chart).

Signals of the photodiodes are amplified by A1 and A2 to be digitally converted by an analog-to-digital converter (ADC) inside a control board with an embedded microcontroller. The microcontroller can receive the converted data and control the tunable FBG, through temperature. The temperature of the tunable FBG can also be digitalized.
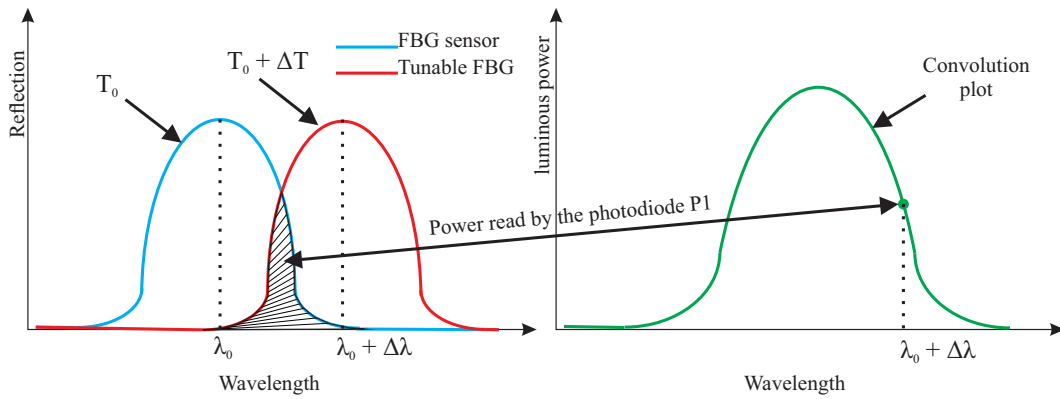
Figure 2.22: Signal in P1 represents the convolution between the reflection profiles of the sensing and the tunable FBGs, for a given temperature difference ΔT between them.

2.3.2 Principle of operation

When the system is turned on the microcontroller makes the TFBG scan the light spectrum searching for the sensor FBG reflection, see figure 2.23. When the sensor FBG reflection spectrum is found a digital PID control routine is initialized. This control has as reference a point over the convolution plot between the reflection profiles, as shown in figure figure 2.24. When the reference is reached any change in the sensor temperature makes the the tunable FBG tracks the sensor reflection profile to maintain the PID error zero. This means that, in steady state, the two reflection profiles are spaced by a constant value ($\Delta\lambda_{\mathrm{const}}$) in the wavelength spectrum, regardless of the sensor temperature, see figure 2.25. Thus, the temperature of the sensor can be associated with the temperature of the tunable FBG, since the difference of temperature between then also remains constant ($\Delta T_{\mathrm{const}}$). Consequently the temperature measurement performed by this system is done indirectly through the temperature sensor disposed within the thermal chamber of the tunable FBG.
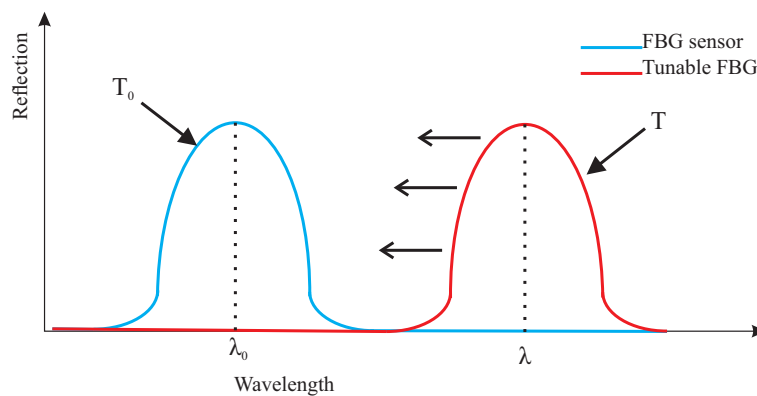
Figure 2.23: TFBG searching for the sensor FBG spectrum when the system is turned on.

Must be noted that for each reference point chosen on the convolution plot exists a different relationship (ΔT) between the two FBGs temperatures. Therefore, a low reference point implies a larger temperature difference between the FBGs and a high reference point implies a shorter temperature difference. This is important when choosing the reference point, because depending
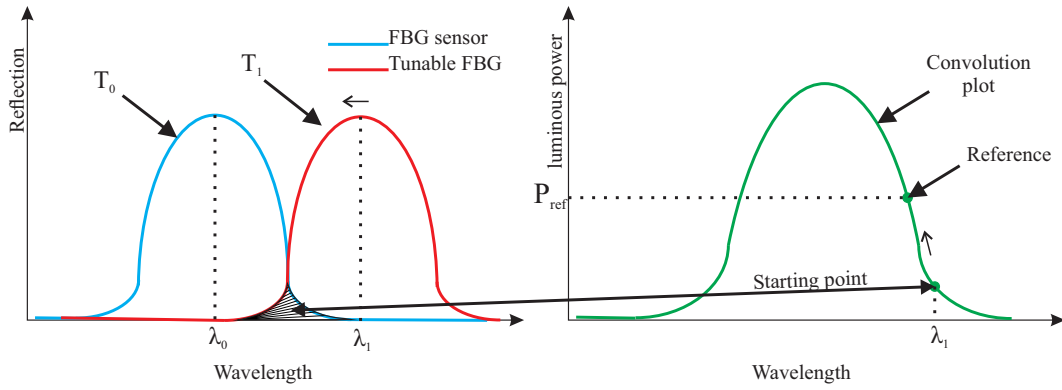
Figure 2.24: When the sensor FBG refection spectrum is found, a PID control routine is initialized with the reference power P_{REF}.
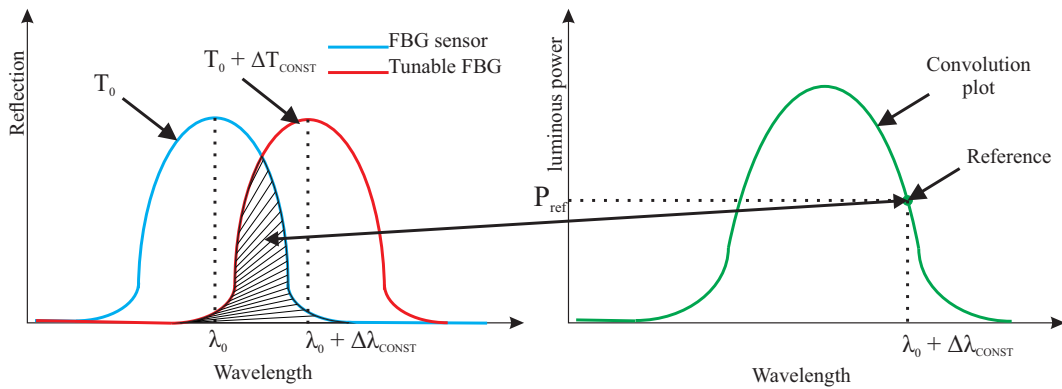
Figure 2.25: When the reference is reached any change in the sensor temperature makes the tunable FBG tracks the sensor reflection profile to maintain error near zero

on the chosen point more energy will be spent to control the temperature of the TFBG through the TEC.

The photodiode P2 checks the amount of luminous power that returns from the sensor allowing the microcontroller performs the necessary compensations. Thus, if there is any event which reduces the luminous power that reaches the interrogator, the microcontroller changes the reference value to maintain the temperature difference constant.

2.3.3 The multi-point system

The system with multiple FBG sensors follows the same principle of operation from the single-point system, and allows the measurement of all sensors almost simultaneously. The figure 2.26 shows the block diagram of the system.

In this scheme, the number of optical components is proportional to the number of FBGs sensing elements, and the final cost of an interrogation system with input for more than 3 FBG temperature sensors is dominated by the cost of the optical components (tracking FBGs, couplers and photodiodes).

The broad band light source illuminates the sensor network with n FBGs sensing elements through a optical circulator $Circ_1$. The reflected light from the FBG sensors is fed into a series
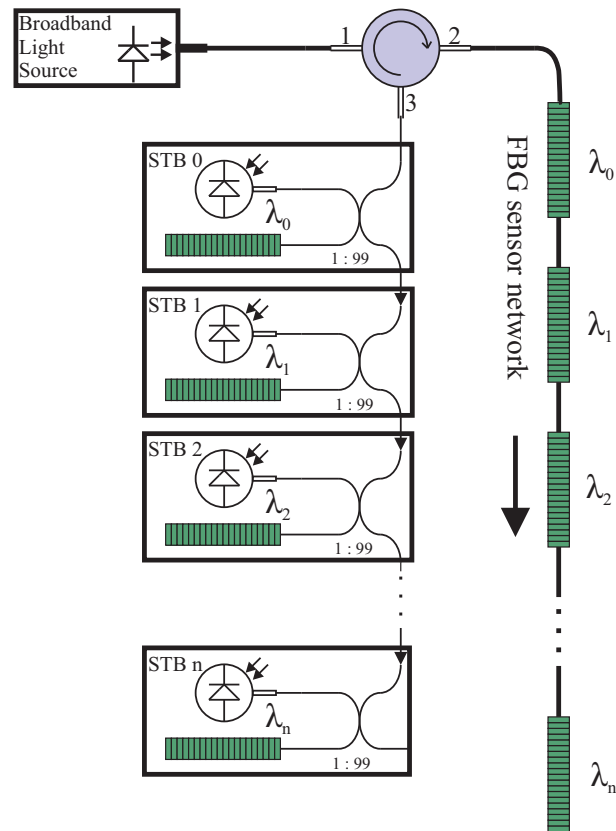
Figure 2.26: Block diagram of the multi-point closed-loop interrogator.

of optical couplers. Each optical coupler let the majority of the incoming light (around 99%) goes to the next coupler, and a small portion (around 1%) of the light is directed into a small circuit called Signal Tracking Block or STB. Each STB module is connected with a optical isolator to prevent light return to the previous STB block. In each STB there is one tunable FBG paired with its respective sensor, one photodiode, one thermoelectric cooler, one semiconductor temperature sensor and one microcontroller along with its electronic circuitry. It is also possible to share one microcontroler with various STBs, but the price of the microcontroller and electronics circuits is so small compared to the optical components (typically less than 5%), that it is highly interesting to have one electronic block for each sensor, because system calibration and maintenance is much simpler. A basic schematic of each STB block is presented in figure 2.27.

Like the single sensor system, the microcontroller inside the STB acquires the output of the transimpedance amplifier, which the value represents the convolution between the sensor and the TFBG. A PID algorithm executed in the microcontroller controls a DAC and a TEC driver circuit, forcing the value of this convolution (output voltage of the transimpedance amplifier) to be equal to a reference value. The temperature measurement of the FBG sensors is also done indirectly through the temperature sensors near the TFBGs.

To stabilize the thermal mass of the TFBGs on their operation points, the system may require up to one minute to reach the steady state. However, once the steady state is reached, all the signal processing for the stabilization of the n sensing FBGs is done in parallel, and only a few microseconds is required to interrogate each one of the n channels. The speed of the
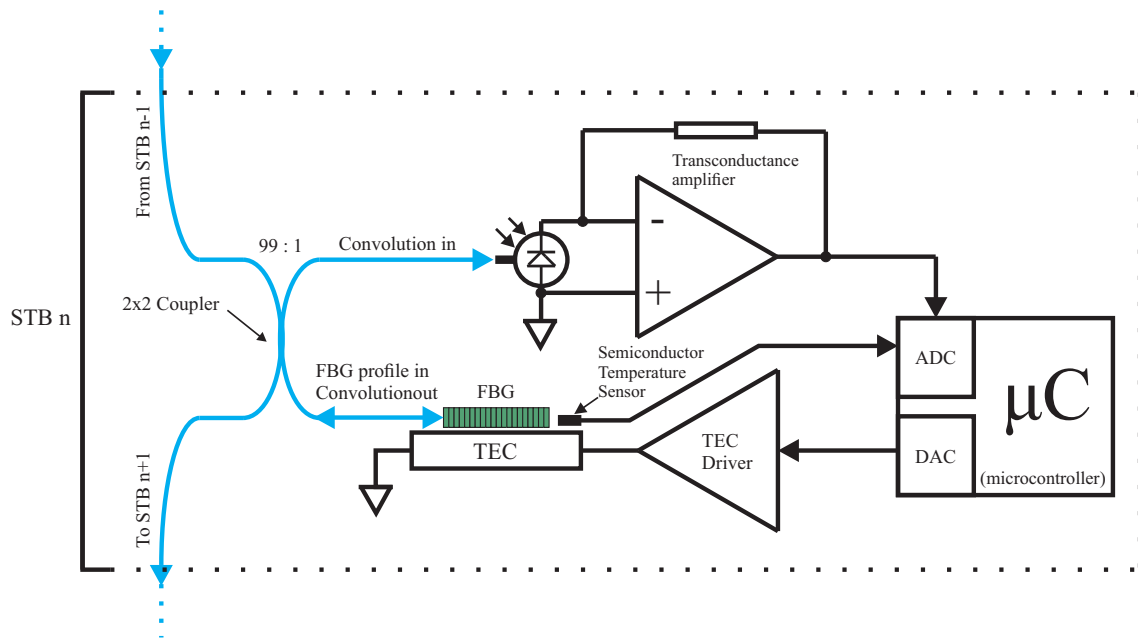
Figure 2.27: Schematic of the Signal Tracking Block - STB

readings depends only of the sampling rate of the analog to digital converter.

3

Experimental procedures and results

THE previous chapters presented the operation principle of the proposed interrogation technique. This chapter will present the assembling of a working prototype, highlighting the design of electronic boards, optical circuit and thermal chambers used in the construction of TFBGs. Subsequently, results and system characterization will be presented and discussed.

3.1 The optical circuit

The optical circuit was designed using the WDM configuration described in section 2.2.1. Figure 3.1 shows the designed optical circuit with two sensing gratings. In this circuit, the light coming the broadband source is directed to the sensing network through an optical circulator, and the reflected light signal enters in the detection system, containing the STB modules. The two STB modules were built in a same electronic board sharing the same microcontroller.
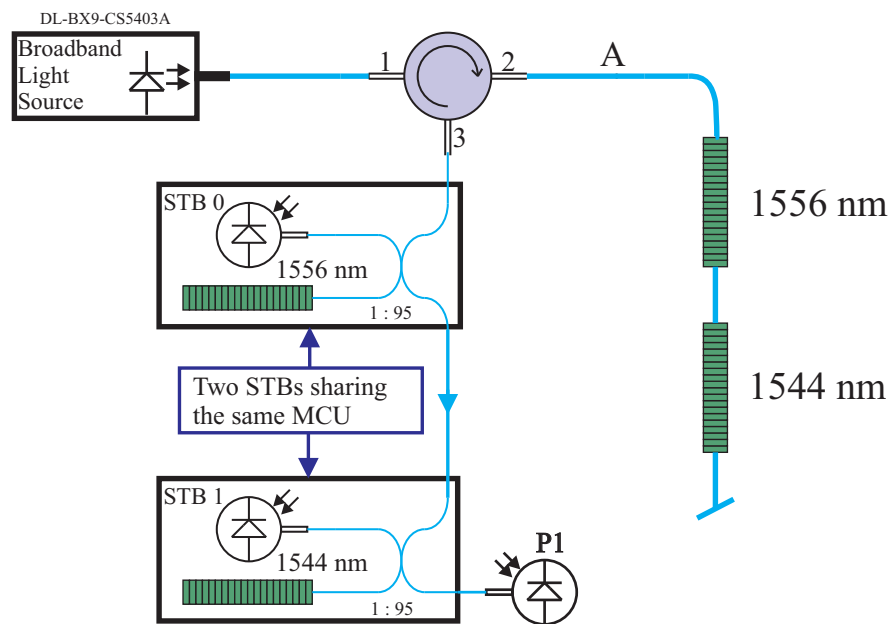
Figure 3.1: Schematic of the optical circuit assembled.

The broadband light source module DL-BX9-CS5403A, a superluminescent light emitting diode (SLED), from Denselight (Denselight 2007), was used to illuminate the sensors. The specifications of this module are described in table B.1 of appendix B. The module is capable of delivering a minimum optical power of 35 mW over a 40 nm bandwidth range centered in 1550 nm, more than enough to illuminate two FBG sensors. According to the manufacturer it is ideal to optical sensing applications, and incorporates a high precision controller for high output level and stability of the SLED.

Four FBGs were available during the development of the optical circuit, and they were acquired from Micron Optics Inc. (MicronOptics 2009). These Gratings are characterized by presenting 250 pm bandwidth and a temperature sensitivity of approximately 9.9 pm/°C (see section B.2 of appendix B for more specifications). The center wavelengths of the gratings were 1544 and 1556 nm, forming two matched pairs.

The reflected light of the sensor array is distributed between the STBs by the two serially placed optical couplers, each one possessing a 95/5 coupling ratio. Therefore, the first STB module (STB 0) receives approximately 5% of the reflected light signal, transmitting 95% of the power to the next STB. Next, STB 1 receives 5% of the incoming signal, resulting in 4.75% of the total reflected light. As there is no other STB, the rest of the signal (around 90%) reaches the photodiode P2. The estimated percentage values of optical power that reach the STBs modules and the photodiode P2 do not take into account other types of losses, always present in practical applications, but serves as a reference to analyze the optical circuit during operation. Figure C.3 in appendix C shows a picture of the assembled optical circuit. To prevent light return to the previous STB module an optical isolator was placed between then.

3.2   The thermal chambers

The thermal chamber design is very critical to the system operation, since the temperature must be equally distributed along the FBG length. A thermal chamber can be easily designed using a thermoelectric cooler (TEC), also called Peltier chip or thermoelectric module (TEM). The operation of a TEC is explained by the Peltier effect, which is the presence of heating or cooling at a junction of two different conductors when an electric voltage is applied. Since the direction of heating and cooling is determined by the polarity of the applied voltage, thermoelectric devices can be used as temperature controllers. They operate like heat pumps, i.e., these devices moves heat energy in the opposite direction of the spontaneous heat flow. Commercial Peltier chips are found in some standardized sizes with their respective voltage and current specifications.

The model utilized for the development of the thermal chamber was the CP10,31,05 from Laird Technologies(Laird 2009). This module comes in a small package of $15 \times 15 \times 2.5$ mm, long enough to accommodate a 10 mm grating over its surface. It is coated with a thermally conductive Aluminium Oxide ceramic which is an electrical insulator but has a relatively high thermal conductivity for a ceramic material, which allows a equally distributed temperature on its surface. The great drawback of thermoelectric coolers is the maximum temperature of operation, which is 80°C for the chosen module, limiting the operation range.

To built the proposed interrogation system, two thermal chambers were necessaries, each one being part of the two TFBGs, and a third chamber was necessary to characterize the sensors. This chambers were designed to allow easy installation of FBGs making easy the exchange process of the gratings, since it would be often necessary during the characterization tests. Therefore, three chambers were equally built using the same materials. A picture of one chamber is shown is figure 3.2
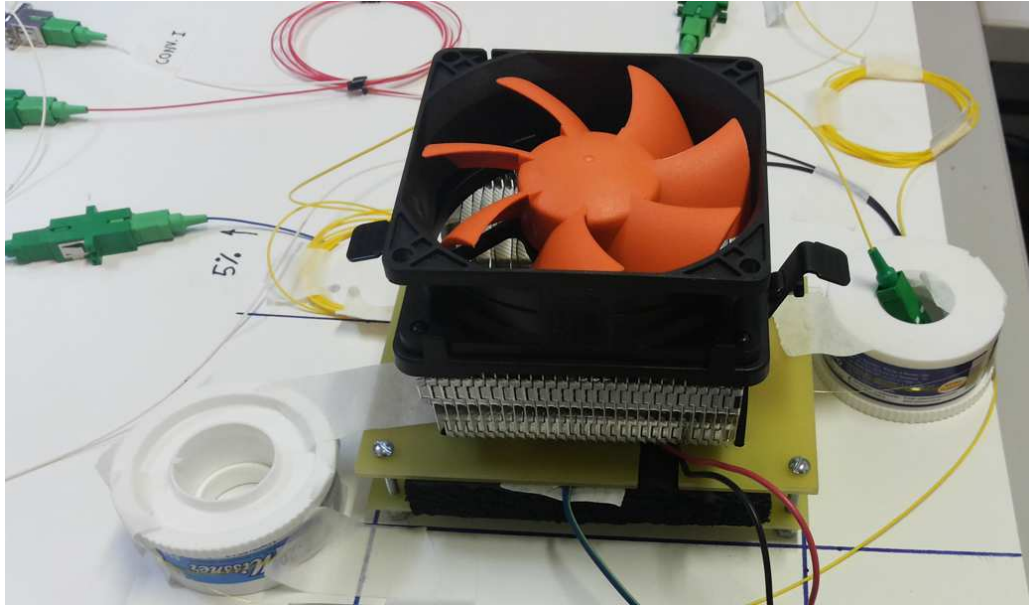

Figure 3.2: Picture of the developed thermal chamber.

The internal view of these chambers is illustrated in figure 3.3. The superior and inferior covers were made of fiberglass plates and produced using a milling machine, and have been designed to perfectly fit a TEC, giving passage to its power wires. The interior was covered with a layer of heat insulating foam to prevent heat exchange with the external environment. To measure the chamber's internal temperature a semiconductor sensor, the AD590 (Analog 2013), was placed directly over the internal face of the TEC. The AD590 is a 2-terminal integrated circuit temperature transducer that produces an output current proportional to absolute temperature (PTAT). It acts like a high impedance current source passing 1 μA/°C. The chip is factory calibrated to generate a 298.2 μA output current at 298.2 K (25°C). The aluminium heat sink was used to create a thermal mass to drain or supply heat to the external face of the TEC, allowing a better cooling or heating of the internal face, respectively.

To ensure a certain temperature uniformity along the length of the FBG, some tests were performed with the one chamber. The tests were performed using two AD590 sensors (Analog 2013) which have a very good accuracy and good thermal coupling. One reference sensor was positioned according to figure 3.4a. This sensor was utilized to perform a temperature control inside the chamber and its measurements was taken as reference. An electronic circuit was utilized to perform a digital PID control to manage the temperature of the chamber. The second sensor was placed over the TEC surface in one of the three different regions, as shown in figure 3.4a. Measurements were made in a range of 50°C, for each one of the three points,
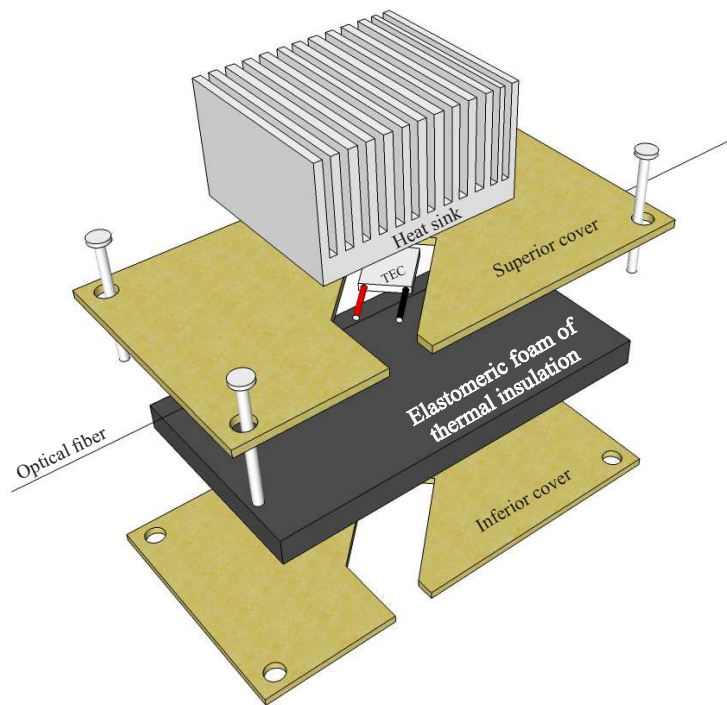
(a) Top view.
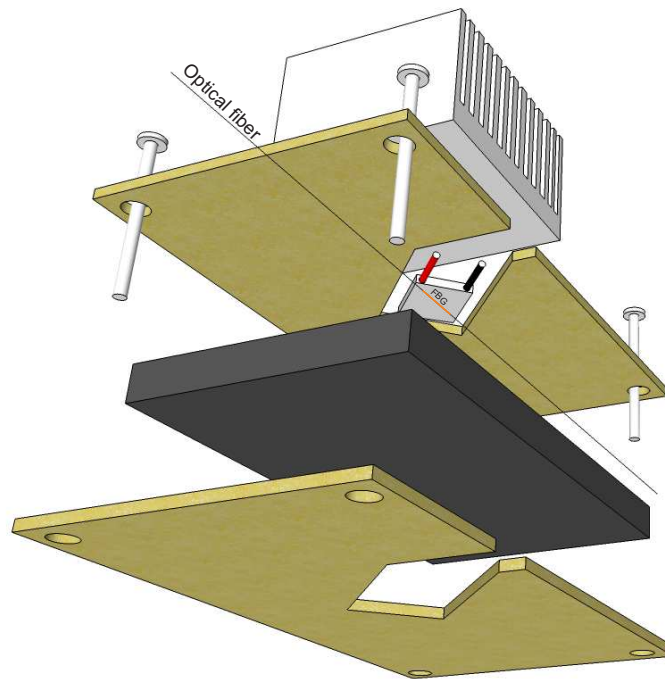
(b) Bottom view.

Figure 3.3: Internal view of the thermal chamber employed in the construction of TFBGs.

and the result can be seen in figure 3.4b.
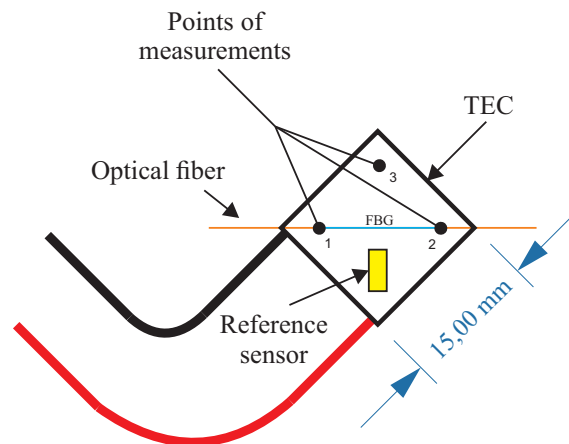
(a) Temperature measurements points over the TEC.
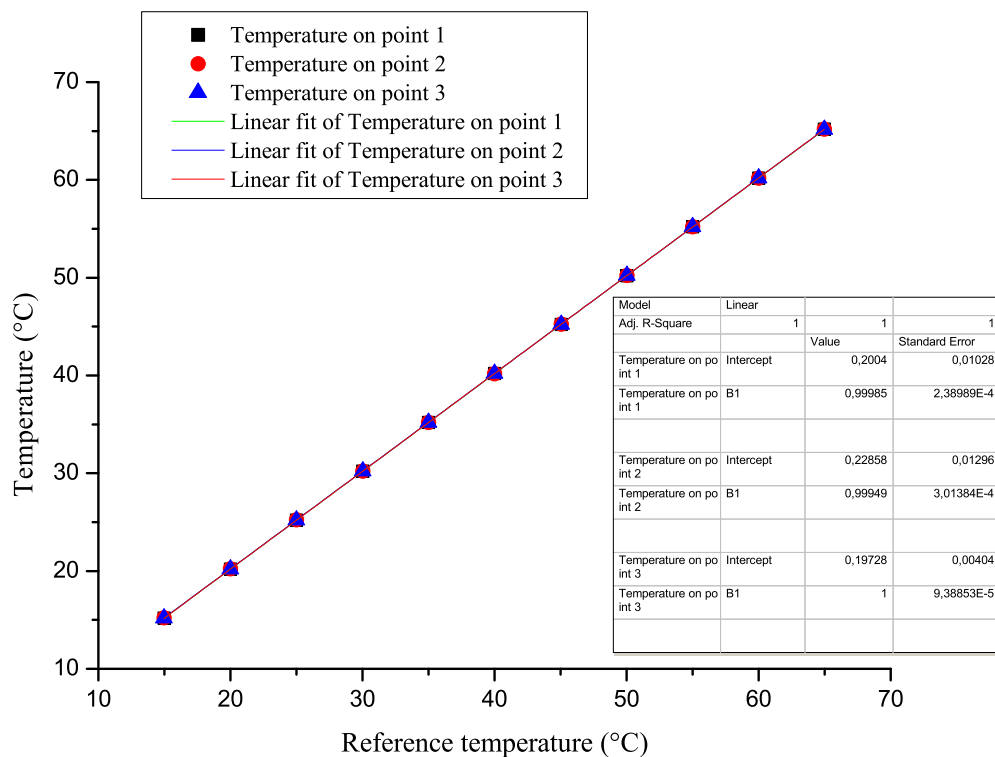
(b) Test results.

Figure 3.4: Temperature measurements made within the thermal chamber to ensure temperature uniformity along the length of the FBG. The performed test confirms a good temperature uniformity inside the thermal chamber.

The test confirmed a good temperature uniformity within the chamber, and it was observed a maximum temperature difference of 0.04°C between points 2 and 3, and 0.03°C between points 1 and 2. Despite the good results, it was noticed, during tests, that the thermal coupling of a FBG (which is a cylindrical surface) to the surface of the TEC is not very good. This was

solved wrapping the FBG with a metallic foil, allowing a good heat exchange.

3.3   Electronic circuits

During the development of this work, the design and programming of the electronic circuits was one of the activities that took longer to be implemented, since they were designed from scratch. The final system was composed of three boards. The first is the control board, designed to perform a digital PID control for each STB module. The second is the TEC driver board, containing the power amplifier that drives the TEC and some protection circuits. The last is the interface and isolation board, which makes the communication link with a computer through a USB port.

3.3.1   Control board

The control board was developed based in the operation of the MSP430F5438A (Texas Instruments 2010), a microcontroller from Texas Instrument which features a 16-bit RISC CPU. The microcontroller has three functions: perform the control routines of the two STB modules, send relevant data to a computer interface, and receive and execute instructions from the computer.

To perform the control routines, the microcontroller needs to receive the digitalized signals from the photodiodes and from the temperature sensors. Both of these transducers generates an electrical current as output, being necessary to convert these currents in electrical voltage before digitalization. For the photodiodes a simple transimpedance amplifier with a low pass filter in the output, shown in figure 3.5, was used. The gain of this amplifier was set to 200 mV/µA and the cutoff frequency of the filter to 10 Hz for each STB. With this gain the peak of the convolution plot reached 650 mV in the output for the STB 0 and around 520 mV for the STB 1.
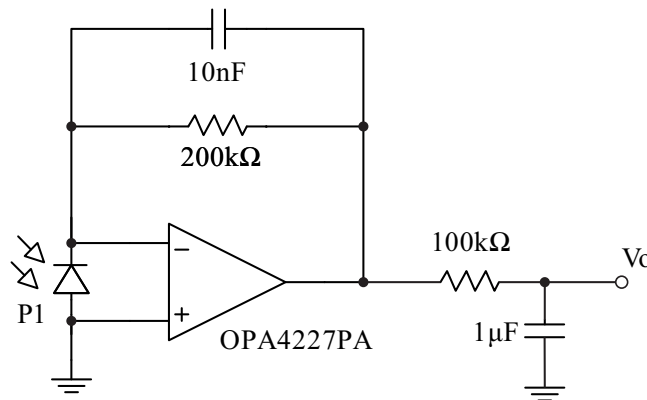

Figure 3.5: Photodiode transimpedance amplifier schematic. The gain was set to 0.2 V/µA and the cutoff frequency to 10 Hz

For the AD590 transducer a similar approach could be used. However, for temperature measurements, the range of interest vary from 270 to 370 K. Therefore, to optimize the output,

a little adjustment was made adding the resistor R_2 and the voltage reference LT1790 (Linear 2009), which adds a negative offset voltage to the output, as can be seen in figure 3.6. Using this scheme the output voltage, V_O, is given by:

$$V_O = 10^{-6} R_2 T - 2.5 \frac{R_2}{R_1}, \tag{3.1}$$

where T is the absolute temperature in Kelvin. Using the indicated values of resistances in figure 3.6 ($R_1 = 9.2$ kΩ and $R_2 = 25$ kΩ), the output, V_O, results in 0 V for 270 K and 2.5 V for 370 K. The LT1790 is capable of delivering a very stable 2.5 V voltage reference. The operational amplifier OPA4227 (Burr-Brown 1998) was chosen for both circuits for being very precise and present low noise (typically 3 nV/$\sqrt{\text{Hz}}$), being an ideal amplifier to be used in measurement systems.
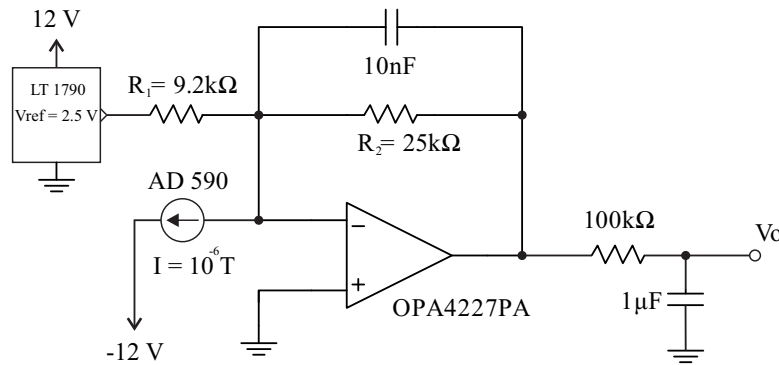
Figure 3.6: AD590 transimpedance amplifier schematic. An offset adjust circuit was added to increase the resolution.

Digitalization was performed by the ASD1256 (Texas Instruments 2003), a 24-bits analog-to-digital converter, which one of its main features is a very low noise. It consists of a sigma-delta modulator, followed by a programmable digital filter. This ADC can perform a sampling rate up to 30,000 SPS (samples per second). It communicates with the microcontroler through a serial-peripheral-interface (SPI) port. Get the best performance of this ADC, requires careful attention in its support circuitry and printed circuit board (PCB) design. Figure 3.7 shows the schematic diagram of the ADS1256. As can be seen, the digital and analog pins are positioned on opposite sides of the chip, facilitating the creation of two ground planes that were tied only in the power source input of the board. The separation in analog and digital planes prevents the entry of high-frequency noises, from the microcontroller, in the analog circuits, improving the signal resolution.

To generate the control signal to drive the TEC a 16-bits digital-to-analog converter was used, the DAC8568 (Texas Instruments 2009), which can perform a full scale output of 2.5 V. It also communicates with the microcontroler through a SPI port, supporting transference rates up to 50 Mbps and settling time of 5 μs for each analog channel when unloaded. The connection diagram of the DAC is shown in figure 3.8. The operational amplifier was used to extend the range of output to ±2.5 V, which is directed to the TEC driver board. The disposition of the analog and digital pins of the DAC are also placed on opposite sides, allowing an appropriate connection in the ground planes.
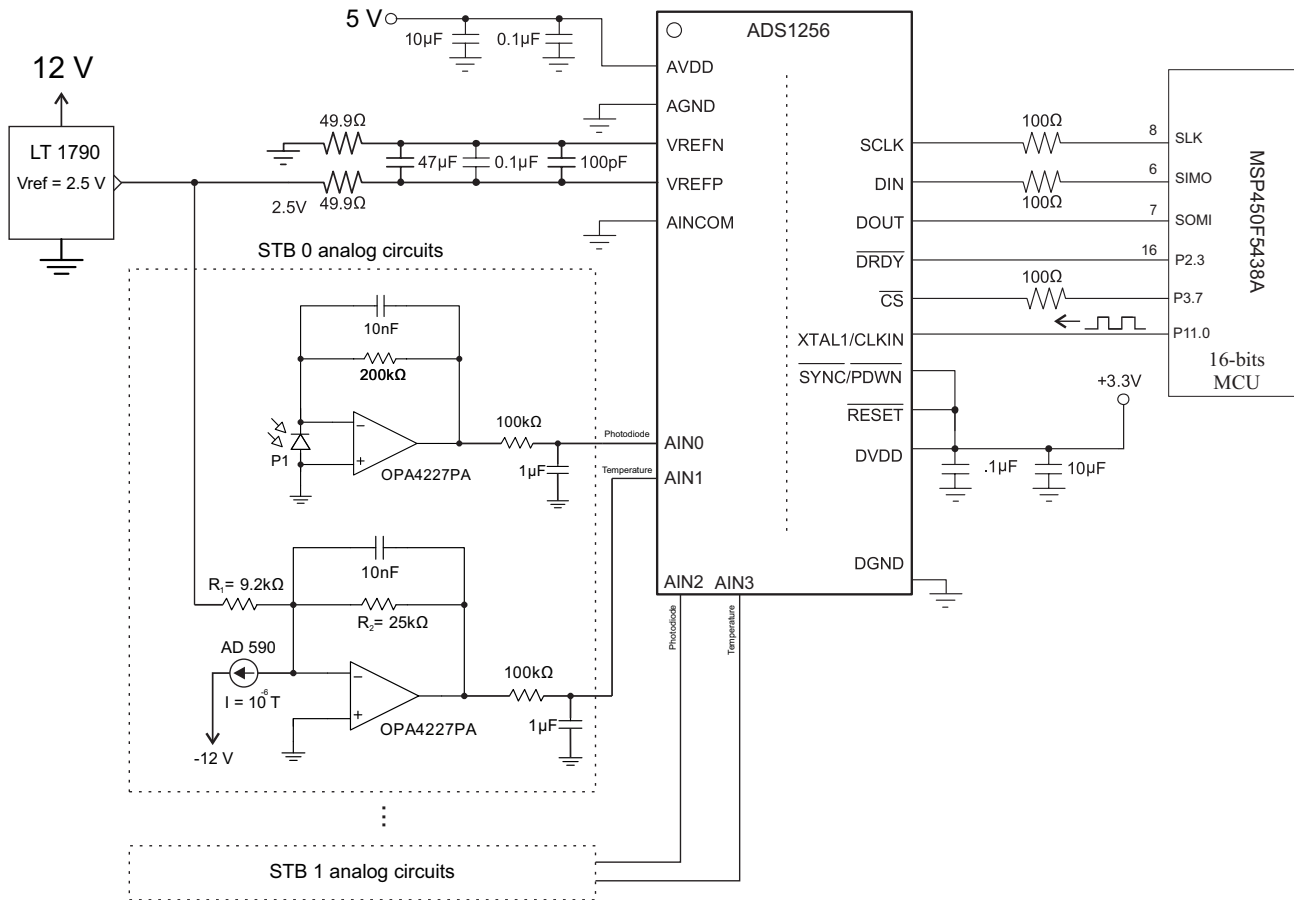
Figure 3.7: Connection diagram of the ADS1256 inside the control board.
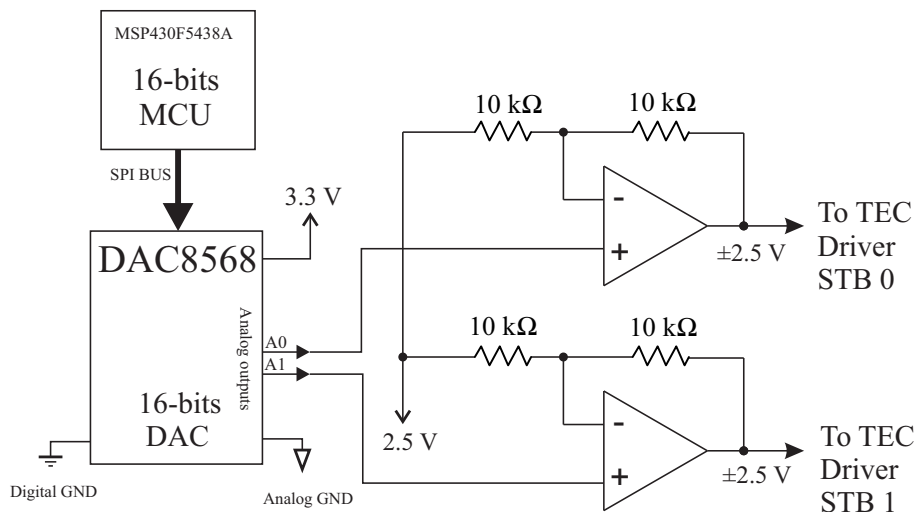
Figure 3.8: Connection diagram of the DAC8568 inside the control board.

The electronic board also features an isolated RS-485 interface, being able to communicate with a PC or a display interface. A picture of the control board is shown in figure 3.9.
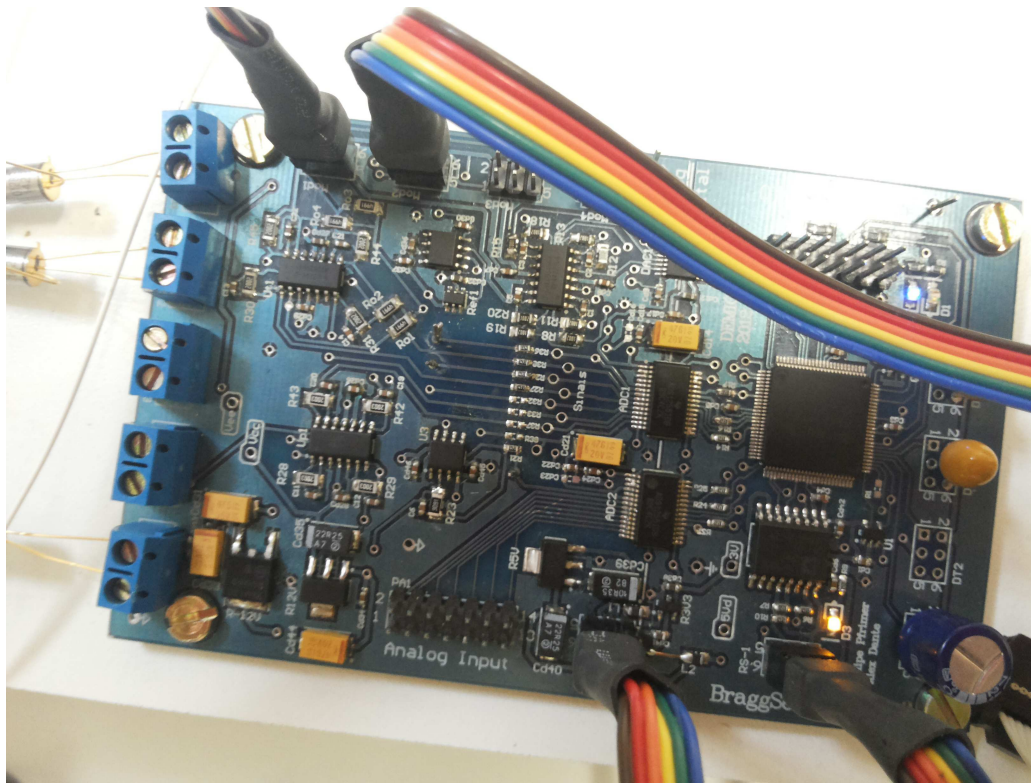
Figure 3.9: Picture of the control board.

3.3.2   TEC driver

The electrical current necessary to drive a TEC is relatively high, ranging between ± 1.5 A for the chosen model. Therefore, a complementary push pull power amplifier was implemented using two complementary Darlington transistors (TIP120 and TIP125), as can be seen in figure 3.10.
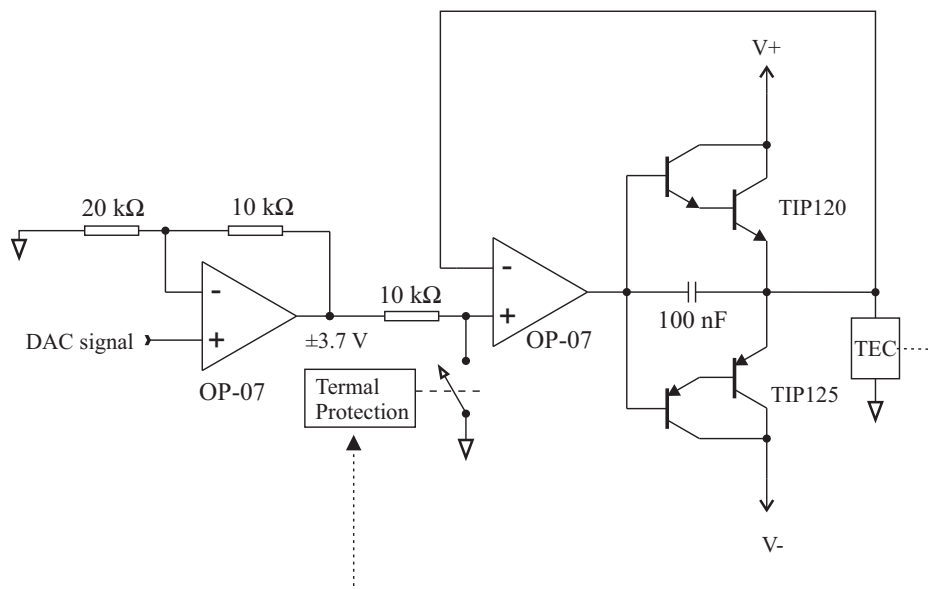
Figure 3.10: Schematic of the TEC driver.

The DAC signal that ranges between ± 2.5 is slightly amplified to reach ± 3.7 V which is the operating range of the TEC. This circuit also features a thermal protection which disables the TEC in case of very high or very low temperatures which could damage either the TEC or the FBG. Low temperatures can condense moisture inside the thermal chamber. The protection circuit measures the AD590 current using a 10 kΩ resistor. The voltage generated over this resistor is applied in the input of a hysteresis comparator that generates a positive voltage when the sensor temperature is out of the operating range. Finally, the output of the comparator is connected with a normally open relay. This protection circuit was very important during the PID control tuning and also during tests. Figure 3.11 shows a picture of the TEC driver board.

Figure 3.11: Picture of the TEC driver board.

3.3.3 Interface and isolation board

The control board communicates through a RS-485 port. Therefore, to perform communications with a PC it is necessary to convert the RS-485 protocol to USB. However, the ground wire within the USB cable can create a ground loop path in some industrial applications where equipment is often powered from different building ground references (Briano 2011), causing noise.

To avoid this problem a small board was developed to isolate the USB ground from the system ground, while transmitting or receiving data. This is possible using the ADM2483, which is an integrated, galvanically isolated component designed for bidirectional data communication (Analog Devises 2005). Basically, this chip converts the differential signal of the RS-485 port in a RS-232 receiving signal or the RS-232 transmitting signal in RS-485 differential signal.

The serial data is converted in USB protocol using the FT232RL chip (FTDI 2010) which is a USB devise controller. This component features a specific pin that automatically controls

the transmitting and receiving buffers of RS-485 half-duplex transceivers, which is the case of the ADM2483.

The data transfer speed of this board is limited by the isolator chip, which can deliver a baud rate of 500 kbps, fast enough to the temperature readings of the interrogation system. A picture of the board is shown in figure 3.12.

Figure 3.12: Picture of the interface and isolation board.

3.4   Experimental results

The prototype was assembled and tested in laboratory, according to the block diagram of figure 3.13.

A portion of the convolution plot of each STB was traced to specify reference points to be used in the control routines. Figure 3.14 shows the convolution plot for STB 0 and STB 1. To trace the convolution plot the temperature of the FBG sensor was held constant at 300 K inside a thermal chamber, while the tunable FBG was shifted by heat over the frequency spectrum. The entire process was controlled by a computer through a software specially developed for this purpose. Although each matched pair have the same nominal center wavelengths, a small difference was observed. This difference was expected since can exist a ± 0.5 pm error in the central wavelength position during the fabrication process, according to informations from the manufacturer, but it does not have any influence in the accuracy of the measurement technique, since each STB has to be calibrated individually.

The reference values for the STB 0 and STB 1, were chosen, respectively, as 332 mV and 369 mV. The selection criteria used to choose the reference points was the convolution value when the matched pair of FBGs are at 300 K (which is a high slope region for both STBs). The manual
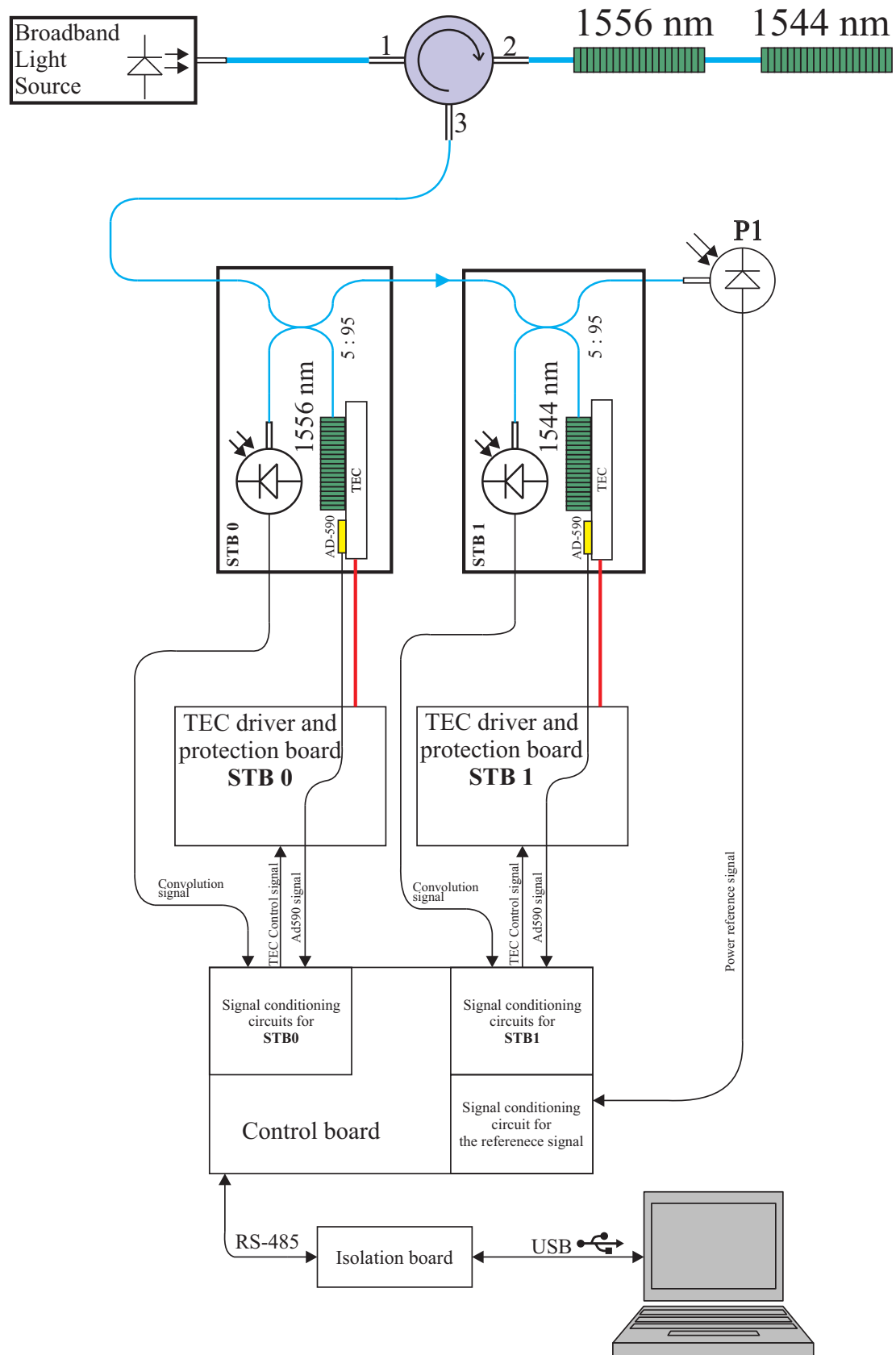
Figure 3.13: Complete block diagram of the experimental setup.
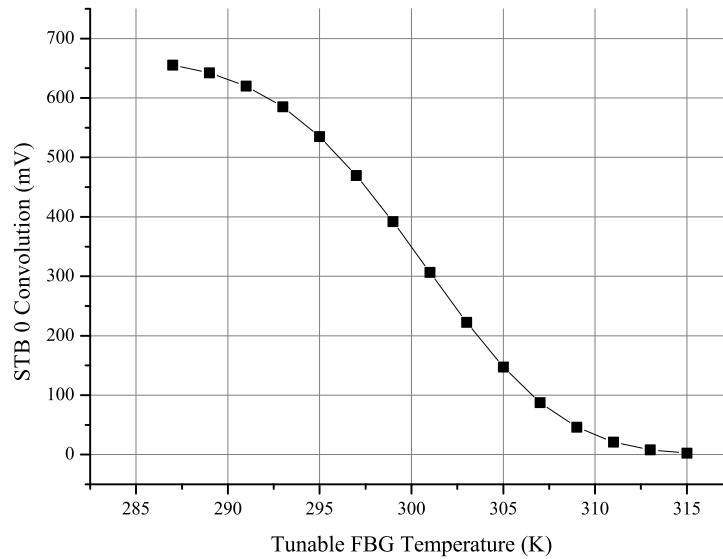
(a) STB 0.
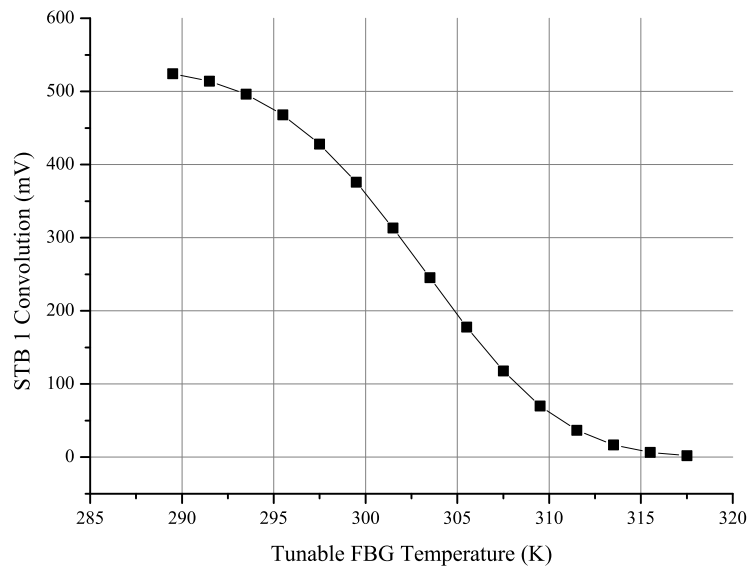
(b) STB 1.

Figure 3.14: Convolution chart with the sensors temperature held at 300 K for the STB 0 and STB 1.

tuning technique was used to adjust the PID control (Araki 1984). After these procedures the system was turned-on and some measurements were made to test the functionality and stability of the proposed interrogation technique.

It is not a requirement to choose the operation point over the right side of the convolution chart, the operation point can be located on either side. To position the operation point on the

left, the error signal must be multiplied by negative one inside the control routine. However, it is recommended to choose the side that requires less energy consumption by the TEC.

As can be seen, the two FBGs which constitute a STB must be chosen so that their central wavelengths λ_B must be preferably near but not equal. If the wavelengths λ_B are very distant the TEC will drain a considerable amount of electrical current to heat or cold the tunable FBG in order reach the steady state. The same happens if the central wavelengths are exactly the same. If, theoretically, the central wavelengths are equals, the system must shift the tunable FBG around 12°C, assuming a short FWHM of 250pm. Ideally, when the two FBGs are near the room temperature the value of the convolution between them must be near of the operating point.

3.5   Calibration tests

To verify the system functionality, the STB 0 sensor was inserted inside the thermal chamber and its temperature was varied over a 70°C range. The system was started and temperature was measured. The measurement result with STB 0 is shown in figure 3.15. The procedure was repeated for the STB 1 and a similar result was obtained, as can be seen in figure 3.16.

Equation	y = a + b*x		
Adj. R-Square	0,99924		
		Value	Standard Error
Tunable FBG temperature	Intercept	36,52272	2,27027
Tunable FBG temperature	Slope	0,8792	0,00699
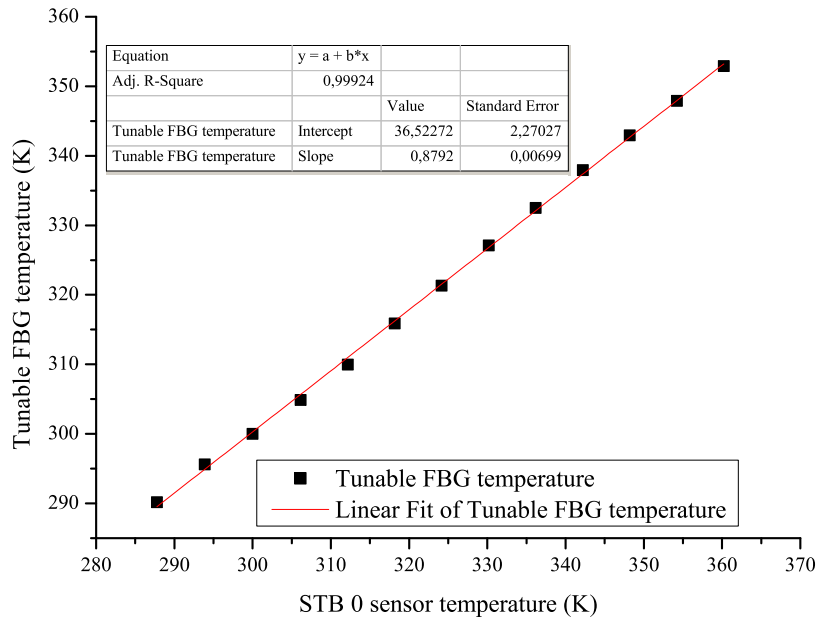
Figure 3.15: STB 0 calibration test

Although the measured points plotted in figures 3.15 and 3.16 deviate slightly from a straight line, the measurements were repeated many times for both STBs, and the repeatability of the measured data points were extremely good, as all points presented a maximum deviation of only ±10 m°C between all sets of measurement experiments. The small non-linearity of the results when compared to the temperature readings obtained with the AD590 can be attributed

Equation	y = a + b*x		
Adj. R-Square	0,99893		
		Value	Standard Error
Tunable FBG temperature	Intercept	20,5713	2,85355
Tunable FBG temperature	Slope	0,93101	0,00878
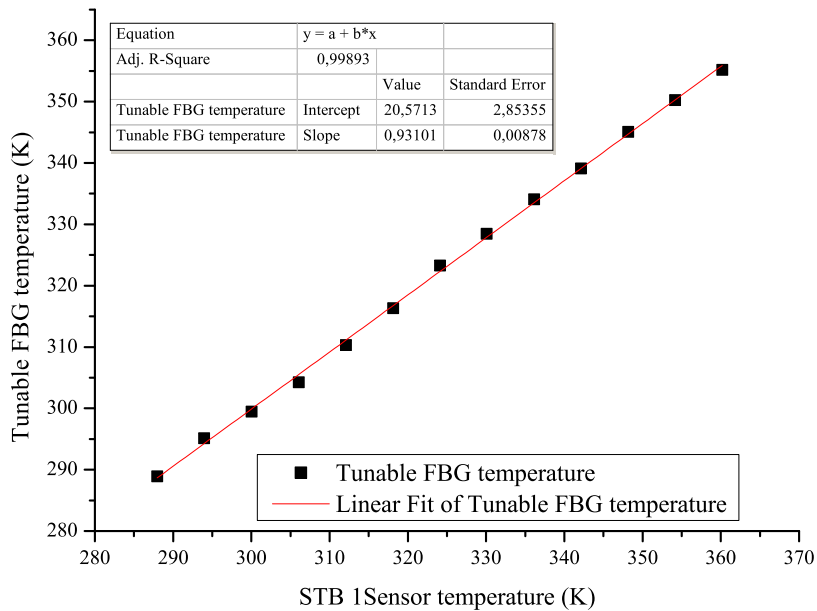
Figure 3.16: STB 1 calibration test.

in part to the AD590 (which has a maximum non-linearity error of 0.3°C) and also to a very small dependency of the reflection profile shape of the FBGs with temperature. However, since the repetition was extremely precise, it suggests that after an initial calibration, the presented measurement technique can be used to measure temperature with a ±1 m°C resolution.
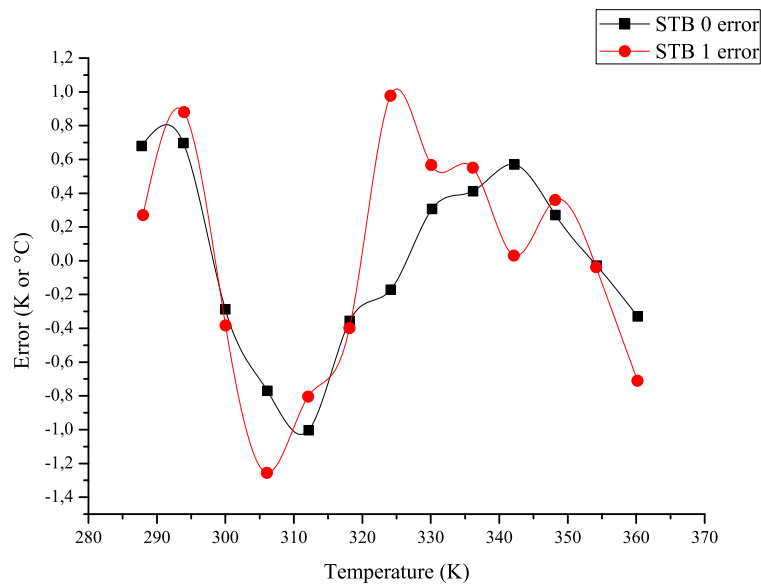
Figure 3.17: Nonlinearity errors.

From the linear regression of the curves obtained with the different STBs, nonlinearity

errors (the maximum deviation of the TFBG temperature over the corresponding FBG sensor temperature from a best-fit straight line) were calculated. The result is can be seen in figure 3.17.

3.6 Stability test

A step temperature rise (10°C) was applied on the FBG sensors in order to measure the system stability. The STB 0 associated sensor was once again inserted inside the thermal chamber. Initially, the temperature of the sensor was controlled at 300 K, and then the control reference suddenly changed to 310 K, at the time t_0. The temperature of the sensor, during the procedure, was independently measured by another AD590 sensor. It was observed that the system presented a good response to the temperature step, as can be seen in Fig. 3.18, where the black curve represents the temperature of the FBG sensor, and the red curve represents the temperature of the TFBG.
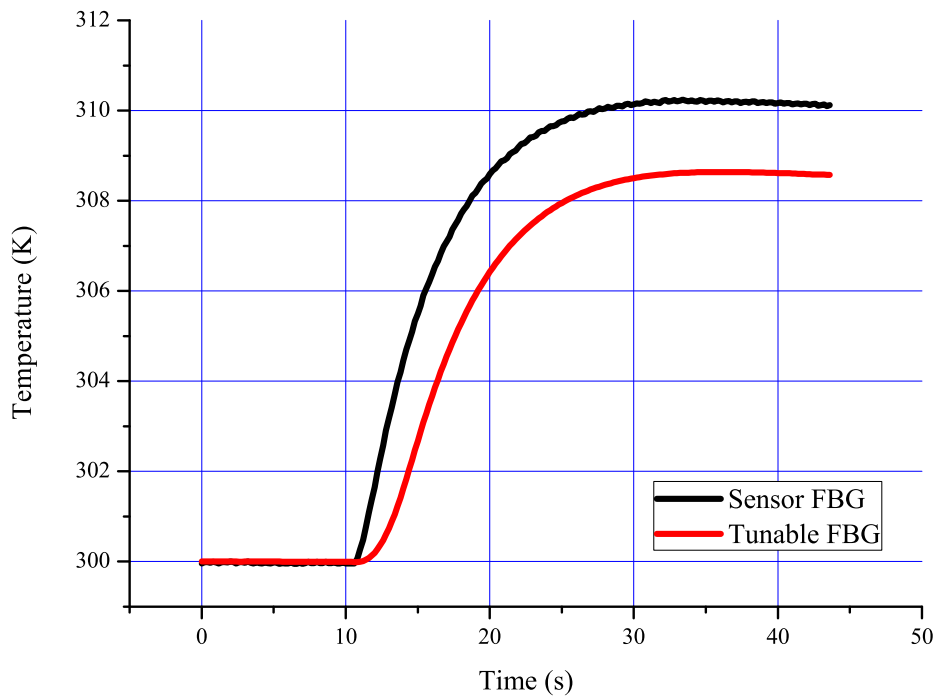
Figure 3.18: Temperature step plot.

It is clear by Fig. 3.18 that the temperature of the TFBG does not reach 310 K, this was expected since the TFBG temperature follows the calibration plot displayed in Fig. 3.15. Fig. 3.19 displays the same measurement normalized to show how the control follows the temperature of the sensor.

It was observed that, during the temperature rise, the system temperature signal delayed 2.2 s in relation to the FBG sensor. This delay is due to the thermal mass of the TFBG, and
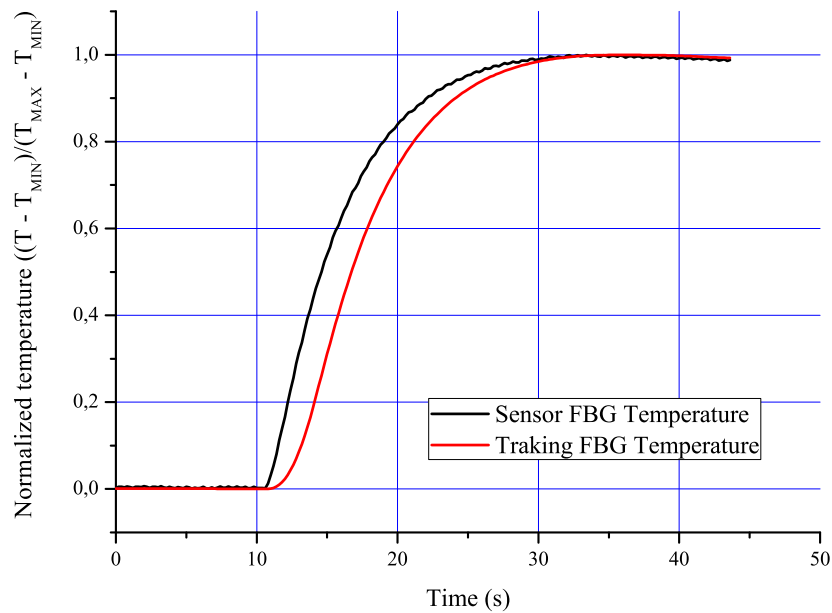
Figure 3.19: Normalized plot of the temperature step.

it is inherent in the system. Fig. 3.20 shows the convolution signal (controlled variable), during the temperature step procedure, reaching a peak of 9 mV above the reference.
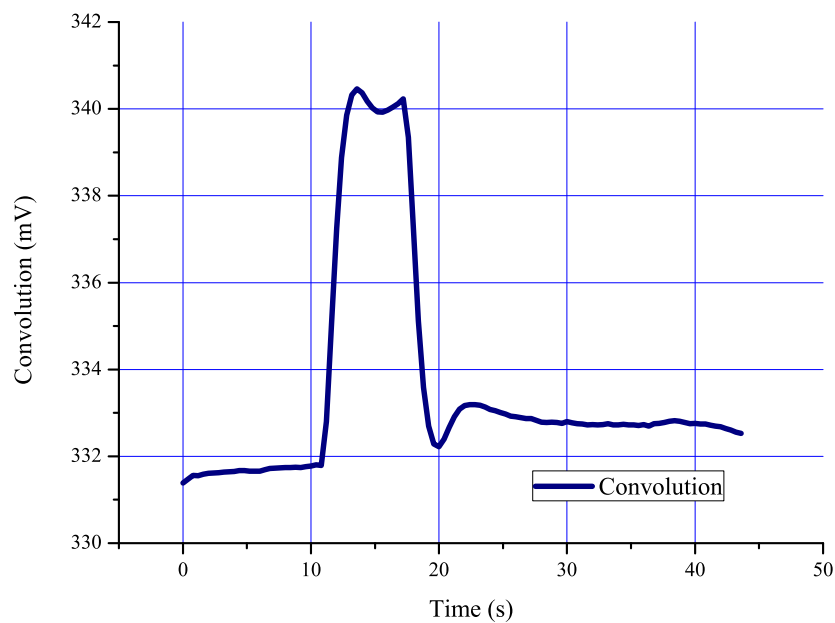
Figure 3.20: Convolution plot during the temperature step.

3.7 Power source compensation routine

To establish a power source compensation routine, it was necessary verify the behavior of the convolution signal in the presence of luminous power loss. To do this, the matched FBGs of STB 0 were held in constant temperatures while the optical power varied. The result is a straight line, as shown in figure 3.21. Therefore, the compensation routine is realized by simply updating the reference point, in every iteration, according to the obtained curve.

Equation	y = a + b*x		
Adj. R-Square	0,99995		
		Value	Standard Error
Convolution signal	Intercept	8,50107E-4	6,09847E-4
Convolution signal	Slope	0,52658	0,00137
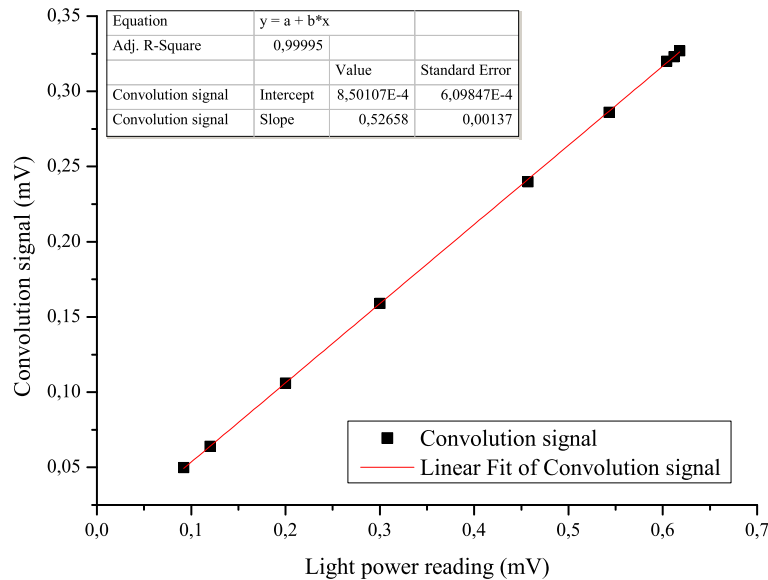
Figure 3.21: Power compensation routine test 1. The matched FBGs of STB 0 were held in constant temperatures while the optical power varied, resulting in a straight line.

To test the amplitude compensation routine an abrupt reduction of the luminous power reflected by the sensor was simulated making a small folding in the optical fiber (point A shown in figure 3.1). Figure 3.22 shows that a 30% reduction of light power (compensation signal) does not affect the temperature reading.

Fig. 3.23 shows that the system starts to be disturbed at 12 s when the power signal (third graph) reaches approximately 400 mV. This reduction represents 33% of power loss. Light loss greater than 33% adds error to the system, but it remains functional. The error added to the measurement can reach 0.05°C to a power loss of 80%, which, depending of the application, is not very significant. A series of measurements showed that the system starts to lose the control only when the reduction of the luminous power is greater than 90%. It is important to note that even with reduced light reflection, the resolution of the temperature remain the same because the reading is taken by the temperature sensor near the tunable FBG. However, the control variable (the convolution value) has its resolution compromised, making the system unstable.
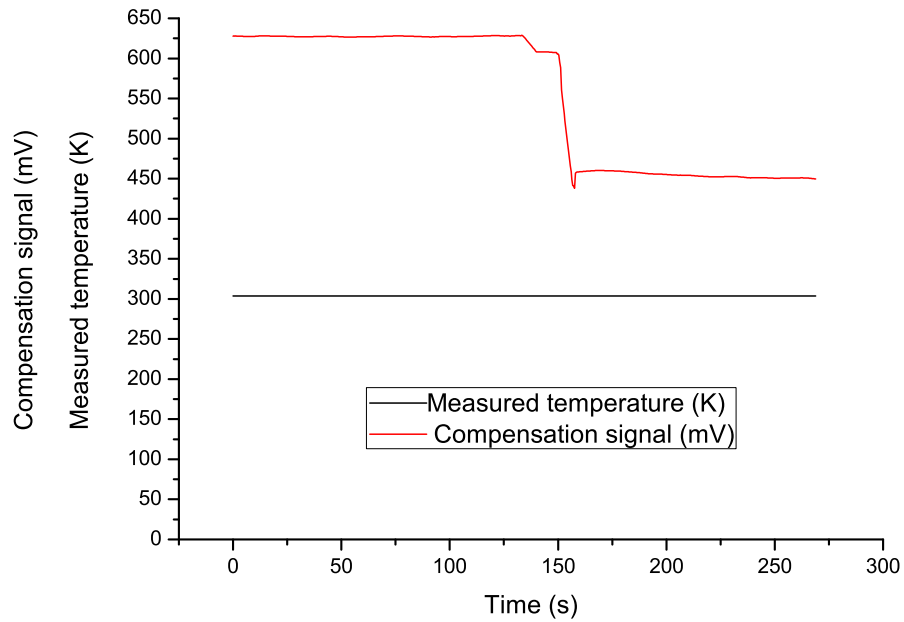
Figure 3.22: Power compensation routine test 1.An abrupt reduction of 30% of the light power does not affect the temperature reading.

3.8   Simultaneous measurement test

After all the tests described so far, the system was programmed to perform simultaneous measurements for both STBs. The FBG sensors were exposed to environmental conditions of the laboratory. The test results can be seen in figure 3.24. At t = 15 s it was approached a glass filled with cold water near to the STB 0 sensor, resulting in a decrease of 2.75 °C of the temperature readings. At t = 21 s it was approached a glass filled with warm water near to the STB 1 sensor, resulting in a increase of 2.5 °C of the temperature readings.

70
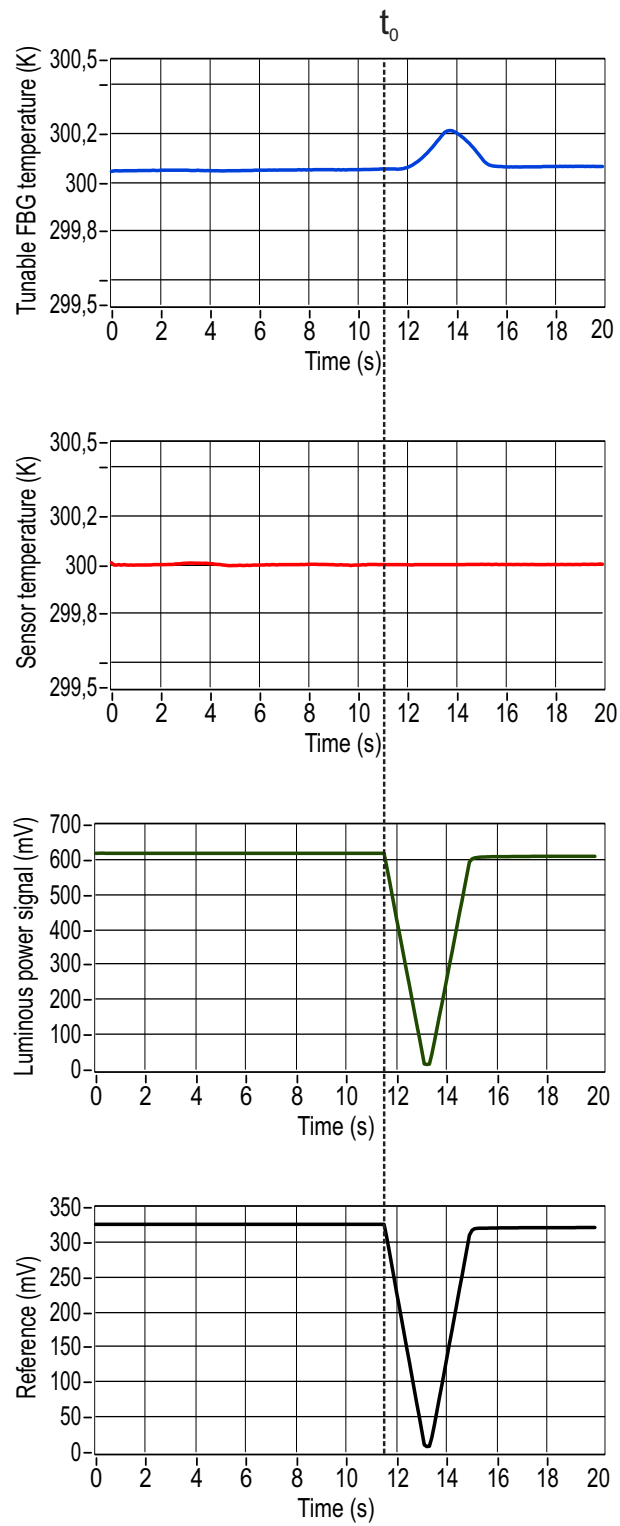
Figure 3.23: An abrupt reduction of the luminous power is compensated by a software routine in the single sensor configuration.
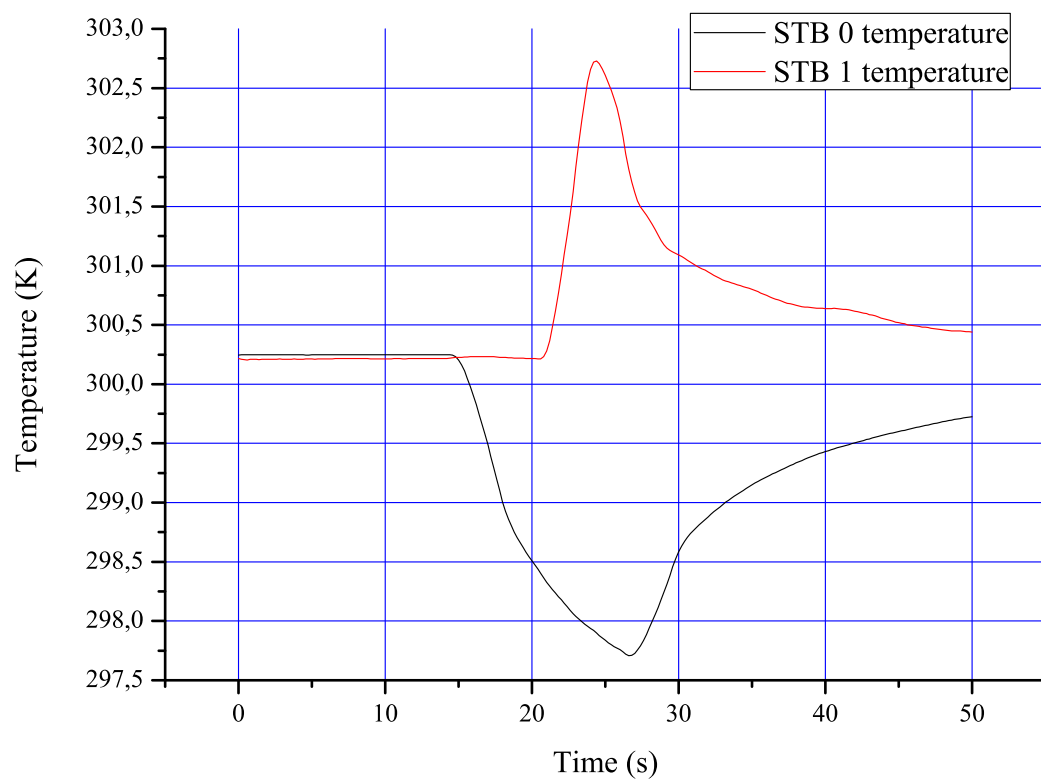
Figure 3.24: Simultaneous measurement test of the two STBs.

Chapter 4

Conclusions

A low-cost multi-point closed-loop interrogation system for temperature measurement has been proposed, assembled and tested. The system is based on a set of pairs of FBGs. Each pair is composed of a TFBG and a sensing FBG element, with matched central wavelengths. The prototype, built to show the feasibility of the concept, had only two channels that can perform simultaneous temperature readings, but it can be easily extended to incorporate a large number of FBG sensors. The maximum number of STBs is limited by the optical source bandwidth and the temperature range of each FBG sensor.

Two TFBGs were built exploring the linear thermal sensitivity of FBG devises. Thermo electric coolers were used as actuators to heat or cool down the gratings. Piezoelectric elements were not used because they present large hysteresis and elevated cost.

The system simultaneously interrogate an array of FBG sensors by tracking down their central wavelengths using the TFBGs. To track the central wavelengths a digital controller was developed using a proportional-integral-derivative (PID) topology. The PID algorithm was tested achieving good response. This closed-loop concept has been studied in some papers (Leite & Ferreira 2007, Cremonezi et al. 2013) and shows one of the most promising alternatives to interrogation of FBGs (Othonos & Kalli 1999).

The system uses a WDM configuration based on an alternative serial topology, described in section 2.2.1. This serial topology facilitates the construction of a modular detection system. Therefore, the system was developed in modules called "signal tracking block" or STB. Each STB is composed of a TFBG and an electronic detection circuit.

Although tested over a small temperature range (70°C), the prototype showed excellent results, being capable of measuring temperatures with a high precision and resolution. The high resolution was achieved by the careful design of the electronic circuit. Larger temperature ranges are possible by gluing the tunable FBG to a metallic substrate (e.g., zinc or cooper), which would greatly increase its sensitivity. In (Dante 2012) there was a large increase in the sensitivity of a FBG using a piece of zinc as substrate which has a high thermal expansion coefficient. With this adaptation the proposed interrogation system could, theoretically, measure temperature in a range up to 250°C.

Although the interrogator may require one or two minutes to stabilize when it is turned-on, after that, the temperature readings are extremely fast, depending of the ADC sampling rate.

The system showed a good response to a rapid temperature changes and did not lose accuracy when subjected to an abrupt reduction of 90% in the luminous power source.

Since it is completely modular, adding new channels is done by simply connecting other STB modules. The cost of each STB module is dominated by the cost of the optical components. The system provides a good solution for low-cost temperature measurements where conventional electrical sensors could not be used.

One of the major difficulties encountered in this work was the design of the thermal chamber, which is essential to the system operation. This difficulty is due to the bad thermal coupling of the optical fiber on the surface of the TEC. This was easily resolved by involving optical fiber with a metallic paper with high thermal conductivity, allowing a better heat transfer. The thermal mass added by this piece of metallic paper is small and, therefore, the speed of the system was not affected.

During the tests, it was observed some dependence of the reflection spectrum shape of FBGs with temperature, that even being low, introduced very-little error to the system measurements. This dependence is proved repetitive and, therefore, can be compensated by software, being a proposal for future works.

4.1   Future works proposals

With the conclusion of this thesis, there are several possibilities of modifications, improvements and studies that can be conducted by future works. New possibilities can be listed:

1. Perform field tests to measure multiple points through the construction of various STBs, in real-world conditions.

2. Improve the thermal chamber design, aiming to build smaller modules that consume less electrical current. This would be possible through the development of smaller TECs, uniquely designed to accommodate the TFBGs.

3. Study the system performance for quasi-static strain measurements.

4. Study a method to encapsulate a FBG with a temperature sensor (e.g., thermistor) in order to facilitate the construction of the tunable gratings.

5. Increase the operating range of each STB module by gluing the TFBGs on metallic substrates with high thermal expansion coefficient.

6. Study the behavior of the reflection spectra of the FBGs as a function of temperature, and the effect of this behavior in the interrogation system, aiming to develop a compensation routine to reduce the absolute error of the system.

4.2   Related publications

F. W. D. PFRIMER, Marcela H. Koyama, E. C. Ferreira, and J. A. Siqueira Dias. "Closed-loop interrogation techniques for temperature measurement using fibre bragg gratings" in International Conference on Photonics, Optics and Laser Technology, 2013.

Alex Dante, Felipe Walter Dafico Pfrimer, Elnatan Chagas Ferreira and José Antonio Siqueira Dias. "A low cost technique for simulation and characterization of Bragg grating sensors in undergraduate instructional laboratories". Accepted in International Journal of Electrical Engineering Education.

4.3   Submissions

Felipe. W. D. Pfrimer, Marcela Koyama, Alex Dante, Elnatan Chagas Ferreira, and Jose A. Siqueira Dias "A Low-cost Closed-loop Interrogation Technique for Ultra-Fast Multi-point Temperature Measurement using Fiber Bragg Gratings" submitted in Journal of Lightwave Technology, 2013.

Appendix A

Digital implementation of a PID Controller

Proportional-Integral-Derivative (PID) control is still widely used in practical applications due to its simplicity and ease of deployment. The user just installs a controller and adjusts three gains to get the best achievable performance. The digital implementation of a PID controller may bring several advantages to the system. The gains in a digital application can be easily changed during the system tuning and even during operation allowing the use of adaptive control. In this appendix we discuss digital PID implementation and its use in the proposed interrogation system. The approach described here was described by (da Silva & Bazanella 2000).

A.1   Introduction

The combination of proportional, integral and derivative actions to generate a single control signal, leads to what is called the proportional-integral-derivative controller or simply PID. The objective is to take advantage of the particular characteristics of each of these actions in order to achieve a significant improvement of transient behavior and steady state of the controlled system. The control signal generated by the PID controller is generally given as:

$$u(t) = K \left(e(t) + \frac{1}{T_i} \int_0^t e(\tau)\mathrm{d}\tau + T_d \frac{\mathrm{d}e(t)}{\mathrm{d}t} \right) \tag{A.1}$$

where the error $e(t)$, the difference between the command and plant output, is the controller input, and the control variable $e(t)$ is the controller output. The three constants are the proportional gain K, the integral time T_i, and the derivative time T_i.

Despite the availability these three basic actions, depending on the application, will not be necessary to use one or more of these actions. Basically there are four possible configurations of controllers from a PID structure:

1. Proportional (P);

2. Proportional-integral (PI);

3. Proportional-derivative (PD);

4. Proportional-integral-derivative (PID).

A.1.1 The proportional band

In practice, by physical or security limitations, it is not possible to apply control signals with unlimited amplitudes. There are an upper limit and a lower limit for the control variable. The control signal given by equation A.1 can be rewritten as:

$$u(t) = Kf(e(t)) = Kw(t). \tag{A.2}$$

Considering the limits of control, the effective applied signal is described as follows:

$$u(t) = \begin{cases} u_{\max} & \text{if } w(t) > u_{\max} \\ Kw(t) & \text{if } u_{\min} \leq w(t) \leq u_{\max} \\ u_{\min} & \text{if } w(t) < u_{\min} \end{cases} \tag{A.3}$$

Therefore, if $Kw(t) > u_{\max}$ or if $Kw(t) < u_{\min}$ it is said that there is a control saturation. In this case the controller behavior becomes nonlinear. In order to obtain a linear behavior, the signal $w(t)$ must belong to the interval $[w_1, w_2]$, where $w_1 = u_{min}/K$ and $w_2 = u_{\max}/K$. The width of the interval $[w_1, w_2]$ is what is called the proportional band, P_b:

$$P_b = w_2 - w_1 \tag{A.4}$$

From this definition is possible to obtain:

$$u_{\max} - u_{\min} = KP_b \tag{A.5}$$

Therefore, a larger proportional band results in a larger linear region and is more difficult to the system enter in a saturated condition.

A.1.2 The proportional controller (P)

Often, simple processes can be controlled satisfactorily with only the proportional action. In this case the integral and derivative actions are simply disconnected, and the equation A.1 becomes simply:

$$u(t) = K(e(t)) \tag{A.6}$$

In many industrial PID controllers, rather than directly we specify the value of K, it is specified the value of the proportional band in percentage. Therefore, considering $u_{max} - u_{min} = 100\%$, it is obtained:

$$K = \frac{100}{P_b} \tag{A.7}$$

Obviously, larger the value of K lower is the proportional band. Higher the gain K, smaller is the value of the steady state error, but this error will never be completely nullified.

A.1.3   The proportional-integral controller (PI)

The main function of the integral action is to make some processes track, with zero error, a reference signal. However, if the integral action is applied alone, it tends to worsen the relative stability of the system. To counterbalance this fact, the integral action is generally used in conjunction with the proportional action, becoming the PI controller, whose control signal is given by:

$$u(t) = K(e(t) + \frac{1}{T_i} \int_0^t e(\tau)) \tag{A.8}$$

The graph in figure A.1 illustrates the application of the integral action together with the proportional action. From this graph it is possible to give an interpretation for T_i: integral time or reset-time, corresponds to the time when the portion of the proportional control action is duplicated. T_i is commonly specified in minutes.
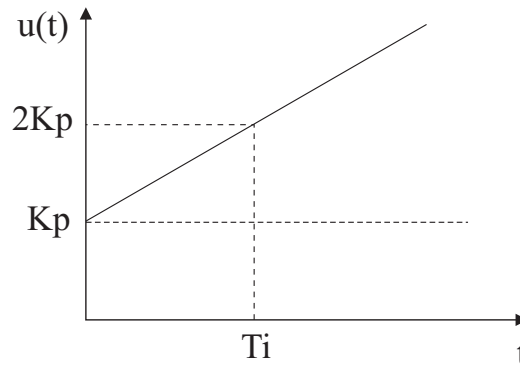
Figure A.1: Effect of the integral action.

By applying the Laplace transform in equation A.8 it is obtained the following transfer function to the PI controller:

$$G_{pi}(s) = \frac{u(s)}{r(s)} = \frac{K(s + 1/T_i)}{s} \tag{A.9}$$

it can be noted that there is a zero at $-1/T_i$ which tends to compensate the destabilizing effect of the pole at the origin.

For high values of T_i, there is a predominance of proportional action, and $T_i = \infty$ corresponds to the proportional controller. In this case, there is steady state error. As the value of T_i is decreased, the integral action begins to overcome the proportional action and the output tends to approach faster to the reference, i.e., the steady state error tends to be canceled quickly. Decreasing excessively T_i it is observed that the response becomes more oscillatory in a tendency to instability. This is justified by the fact that, in this case, the zero of the controller begins to deviate excessively from the pole at the origin, and the controller tends to behave as a pure integrator.

A.1.4 The proportional-derivative controller (PD)

The output from a process has, intuitively, a certain "inertia" in relation to changes in the input variable. This "inertia" is explained by the dynamics of the process that makes a change in the control variable induce a considerable change in the output of the system only after a certain time. Another interpretation is that, depending on the process dynamics, the control signal will be "late" to correct the error. This fact is responsible for transients with large amplitude and period of oscillation, and may, in an extreme case, generate unstable responses.

The derivative action, when combined with the proportional action, has the function of "anticipating" the control action in order for the process to react faster. In this case, the control signal to be applied is proportional to a prediction of the process output.

The basic structure of the PD controller is given by:

$$u(t) = K\left(e(t) + T_d\frac{de(t)}{dt}\right) \tag{A.10}$$

Considering that $e(t + T_d)$ can be approximated by:

$$e(t + T_d) \approx e(t) + T_d\frac{de(t)}{dt}, \tag{A.11}$$

it follows that $u(t) \approx Ke(t + T_d)$, i.e., the control signal is proportional to the control error estimation T_d time units ahead. In other words, the prediction is made by extrapolating the error value for the tangent line to the curve of error in the instant t, as can be seen in figure A.2.
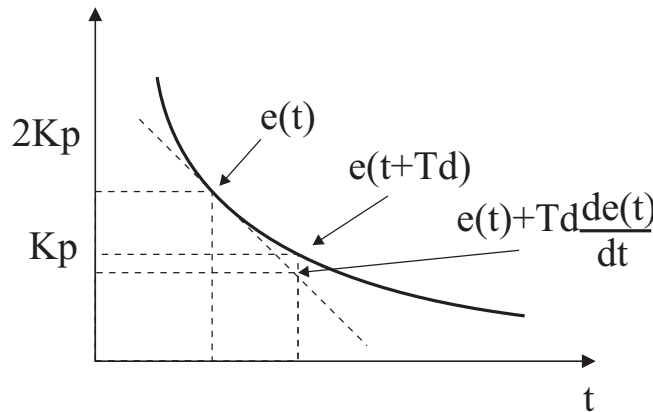
Figure A.2: Effect of the proportional-derivative action.

This predictive action tends to increase the relative stability of the system and make the transient response, more fast. In practice, one should limit the derivative gain at high-frequencies by adding a pole p. The transfer function of the PD controller is then given by:

$$G_{pd} = \frac{u(s)}{r(s)} = K(1 + \frac{spTd}{s+p}) = \frac{K(1 + T_dp)(s + \frac{p}{1+pT_d})}{(s+p)} \tag{A.12}$$

It can be noted that the zero of the PD controller is always at the right of the pole. It is also clear that as T_d increases, the zero of the controller tends to the origin, meaning the prevalence of derivative action.

A.1.5 The PID controller

The proportional controller combines the advantages of PI and PD controller. The integral action is directly linked to the precision of the system being responsible for the null steady state error. The PI controller destabilizing effect is counterbalanced by the derivative action that tends to increase the relative stability of the system while the system response becomes faster due to its anticipatory effect.

The transfer function of the PID controller is given by:

$$G_{pid} = \frac{K\left(s^2 + \frac{1+T_dT_i}{T_i}s + \frac{p+T_ip}{T_i}\right)}{s(s+p)} \tag{A.13}$$

It is important to note that equation A.1 and transfer function A.13 constitute the classical version of the PID controller. Other versions and variations exist, but the operating principle from the combined effects of the three basic actions, are the same.

A.2 Digital implementation

The implementation of the PID controller can be made by making numerical approximations of the derivatives and the integral appearing in the control law. Thus, it is possible to describe each action by a recurrence equation. The recurrence equations describe the mathematical operations to be programmed into the microcontroller or microcomputer which will be implemented the digital PID.

Assume that the sampling period T is suitably chosen to satisfy the Nyquist theorem. The control signal will be updated only in time instants $t_k = kT$. The system output, the reference signal, the control signal, and the error in a given time t_k will be denoted as $y(k), r(k), u(k)$ and $e(k)$, respectively.

A.2.1 Proportional action

The discretized proportional term to be applied in the instant k is given by:

$$P(k) = K(r(k-1) - y(k-1)) = K(e(k-1)) \tag{A.14}$$

A.2.2 The integral action

The integral action is given by:

$$I(t) = \frac{K}{T_i} \int_0^t e(t)dt, \tag{A.15}$$

or equivalently by:

$$\frac{dI(t)}{dt} = \frac{K}{T_i}e(t) \tag{A.16}$$

There are several ways to discretize equation A.16, two of then will be presented next.

Backward Differences

In this case we have the following approximation to the equation A.16:

$$\frac{I(k) - I(k-1)}{T} = \frac{K}{T_i}e(k) \tag{A.17}$$

which is equivalent to the following recurrence equation:

$$I(k+1) = I(k) + \frac{K}{T_i}e(k) \tag{A.18}$$

Tustin's approximation

The Tustin approximation, also known as bilinear transformation, gives us the following recurrence equation:

$$I(k+1) = I(k) + \frac{KT}{T_i}\frac{e(k+1) + e(k)}{2} \tag{A.19}$$

A.2.3   The derivative action

The derivative term can be re-written as follows:

$$\frac{dD}{dt} + Dp = -KT_d\frac{de(t)}{dt} \tag{A.20}$$

Likewise the integral term, equation A.20 can be discretized according to various methods, that will be presented below.

Backward Differences

$$\frac{D(k) - D(k-1)}{T} + pD(k) = -KT_d\frac{e(k) - e(k-1)}{T} \tag{A.21}$$

The recurrence equation in this case is:

$$D(k) = \frac{1}{1 + pT}D(k-1) - \frac{KT_dT}{1 + pT}(e(k) - e(k-1)) \tag{A.22}$$

Tustin's approximation

For the Tustin's approximation there is the following recurrence equation:

$$D(k) = \frac{(pT - 2)}{(pT + 2)}D(k-1) + \frac{2KT_d}{T(pT + 2)}(e(k) - e(k-1)) \tag{A.23}$$

A.2.4   PID routine

From the presented above, the routine for the implementation of the digital PID control algorithm can be written from the recurrence equations of each actions. An example of basic code would be as follows:

```
#define        K              50
#define        T              0.05
#define        T_i            0.05
#define        T_d            0.025

#define        UPPER_LIMIT          100
#define        LOWER_LIMIT          -100

P= K*error
I=I_prev+ {K*T}*{2*T_i}*(error+error_prev}/{(2*T_i)}
D=(pT-2)/(pT+2)}*D_prev + 2*K*T_d*T*(pT+2)*(error-error_prev)
control_signal = P + I + D
if(control_signal >= UPPER_LIMIT){control_signal = UPPER_LIMIT;}
if(control_signal <= LOWER_LIMIT){control_signal = LOWER_LIMIT;}
error_prev=error
D_prev = D
```

Appendix B

Optical devises specifications

B.1   Broadband light source module DL-BX9-CS5403A

According to DenseLight (Denselight 2007), the DL-BX9-CS5403A is a superluminescent light emitting diode (SLED) broadband source, ideal for fiber optic sensors. It provides a stable light source over a wide wavelength range for C band as can be seen on table B.1. It module incorporates a high precision controller for high output level and stability of the superluminescent diodes output.

Parameter	Min	Typical	Max	Unit
Operating temperature (case)	0		65	°C
Operating Relative Humidity			85	%
Input current			6	A
Min optical power	35			mW
Typ. Bandwidth		40		nm
Central wavelength		1550		nm
Output stability: 1 hour 8 hour			±0.03 ±0.01	dB dB

Table B.1: Broadband light source module DL-BX9-CS5403A specifications (Denselight 2007)

B.2   Characteristics of the FBGs used in this thesis

Table B.2 shows the specifications of the FBGs utilized during the development of this thesis.

Physical Properties	
Number of FBGs	1
FBG Length	10 mm
Strain Limit	5000 $\mu\varepsilon$
Strain Sensitivity	≈ 1.2 pm/$\mu\varepsilon$
Operating Temperature Range	- 40 to 120°C
Thermal Response	≈ 9.9 pm/°C
Fiber Lead Length	1 m ($\pm$ 10 cm), each end
Fiber Type	SMF28-Compatible
Fiber Coating	Polyimide
Fiber Re-Coating Diameter	145 - 165 μm
Fiber Bend Radius	≥ 17 mm
Optical Properties	
Peak Reflectivity (Rmax)	$\geq 70\%$
FWHM (-3 dB point)	0.25 nm ($\pm$ 0.05 nm)
Isolation	≥ 15 dB (@ $\pm$ 0.4 nm around center wavelength)

Table B.2: FBGs specifications (MicronOptics 2009)

Figure B.1 shows the typical reflection profile of the FBGs utilized during the experimental measurements. It is easy to see some side-lobes in the profile.
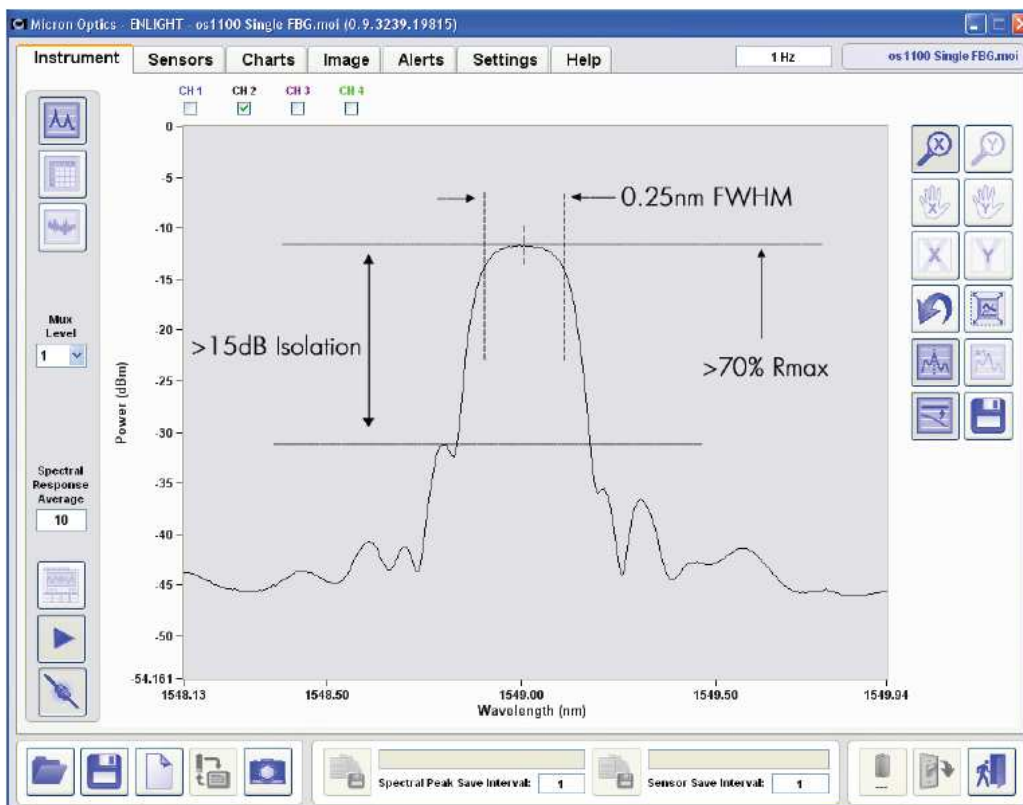

Figure B.1: Spectral characteristic of the FBGs (MicronOptics 2009).

B.3   Optical circulator

The PIOC315P213 (AC Photonics 2011b) is an optical circulator developed by ACphotonics. Its characteristics are described in table B.3.

Parameter		Value
Configuration		Port 1 to Port2 to Port 3
Operation		1550±30
Insertion Loss (dB)	Typical	0.6
	Maximum	0.8
Channel Peak Isolation (dB)		≥50
Channel Minimum Isolation(dB)		≥40
Channel Cross Talk (dB)		≥50
Polarization Dependent Loss (dB)		≤0.15
Polarization Mode Dispersion (ps)		≤0.1
Return Loss (dB)		≥50
Power Handling (mW)		300
Operating Temperature (°C)		0∼ +70
Storage Temperature (°C)		−40 ∼ +85
Package Dimensions (mm)		Radius = 5.5; Length = 50

Table B.3: Optical circulator specifications (AC Photonics 2011b).

B.4   Optical couplers

The WP36050202B2033 (AC Photonics 2011c) is an optical coupler developed by ACphotonics. Its characteristics are described in table B.4.

Parameter	Specification
Coupling Ratio (%)	5/95
Directivity (dB)	≥55
Operating Temperature (°C)	−20 ∼ +70
Storage Temperature (°C)	−40 ∼ +85
Fiber Type	Corning singlemode SMF-28
Fiber Pigtail Length (m)	1
Port Configuration	2x2
Package Dimension (mm)	Radius = 3; Length = 40

Table B.4: Optical couplers specifications (AC Photonics 2011c).

B.5   Optical isolator

The IU15P21B3 (AC Photonics 2011a) is a dual stage optical isolator developed by ACphotonics. Its characteristics are described in table B.5.

Parameter	Value
Operating Wavelength (nm)	1550
Typical Peak Isolation (dB)	58
Minimum Isolation (dB)	46
Typical Insertion Loss (dB)	0.4
Maximum Insertion Loss (dB)	0.6
Return loss (In/Out) (dB)	$\geq 65/60$
PDL (dB)	≤ 0.05
PMD (ps	0.2
Bandwidth (nm)	± 30
Operating Temperature (°C)	$-20 \sim +70$
Storage Temperature (°C)	$-40 \sim +85$
Fiber Type	Corning SMF-28
Fiber Length (Min.)	1 meter each end
Power Handling (mW)	300
Package Dimension (mm)	Radius = 5.5; Lenght = 30

Table B.5: Optical isolator specifications (AC Photonics 2011a).

C

System images
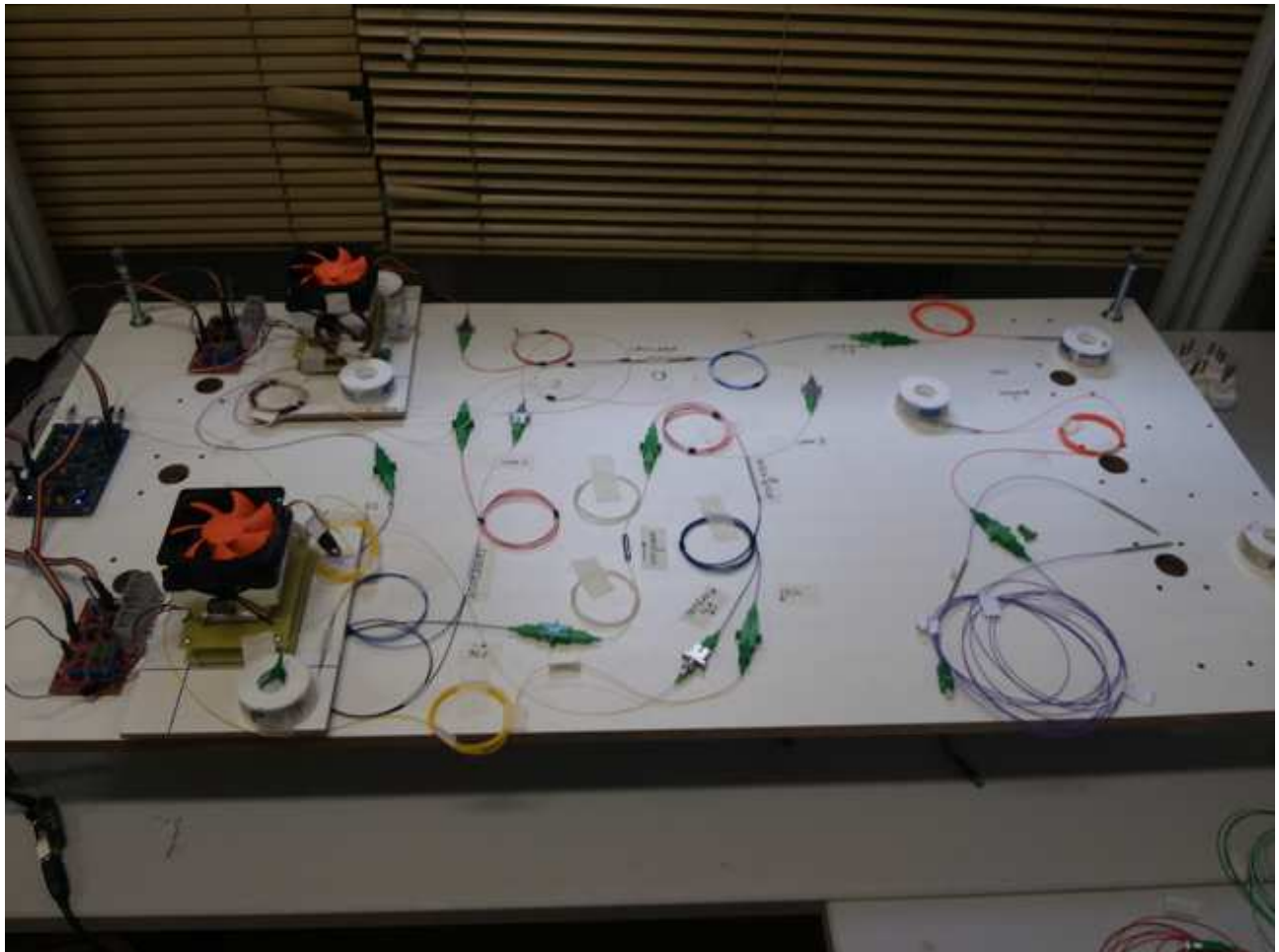
C.1 Pictures of the experimental setup

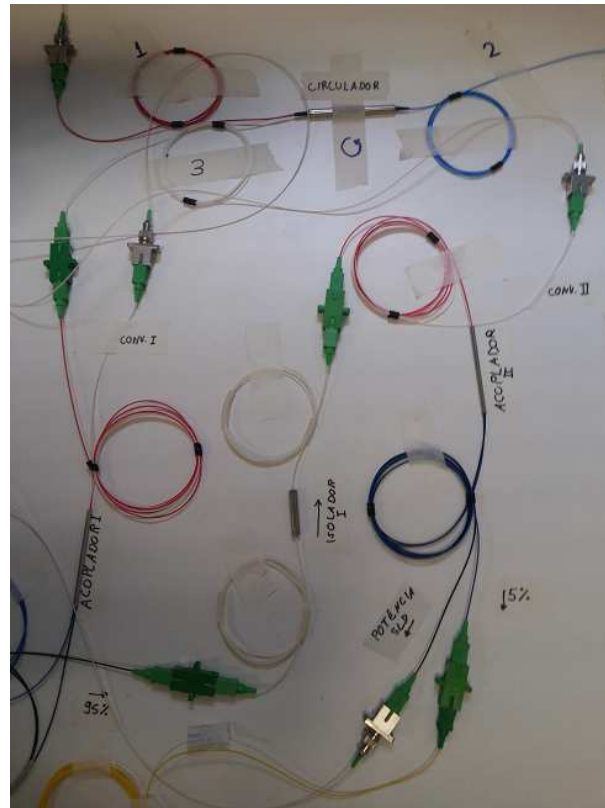Figure C.1: Picture of the assembled prototype.

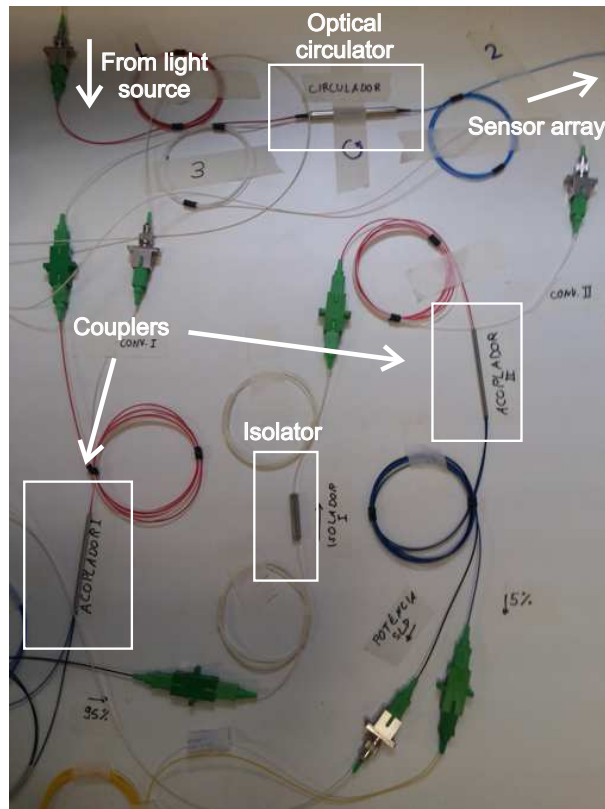Figure C.2: Picture of the assembled optical circuit.

Figure C.3: Picture of the assembled optical circuit with details.

Figure C.4: Picture of the broadband light source.
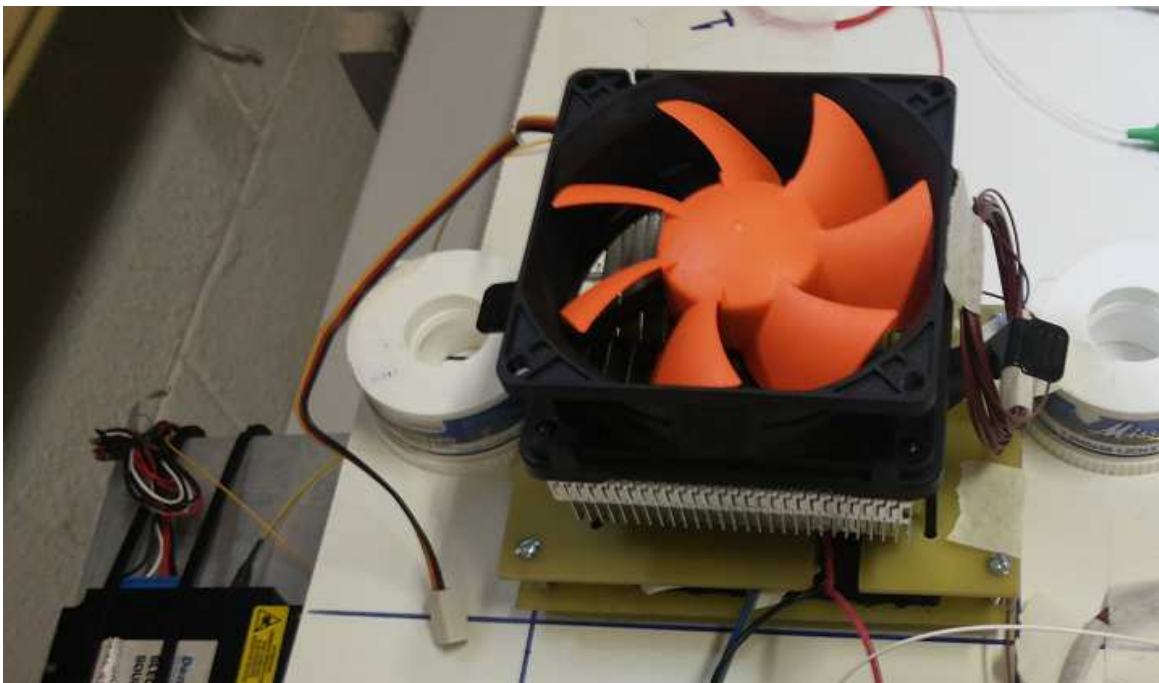
C.2 Pictures of the thermal chamber

Figure C.5: Picture of the assembled thermal chamber.
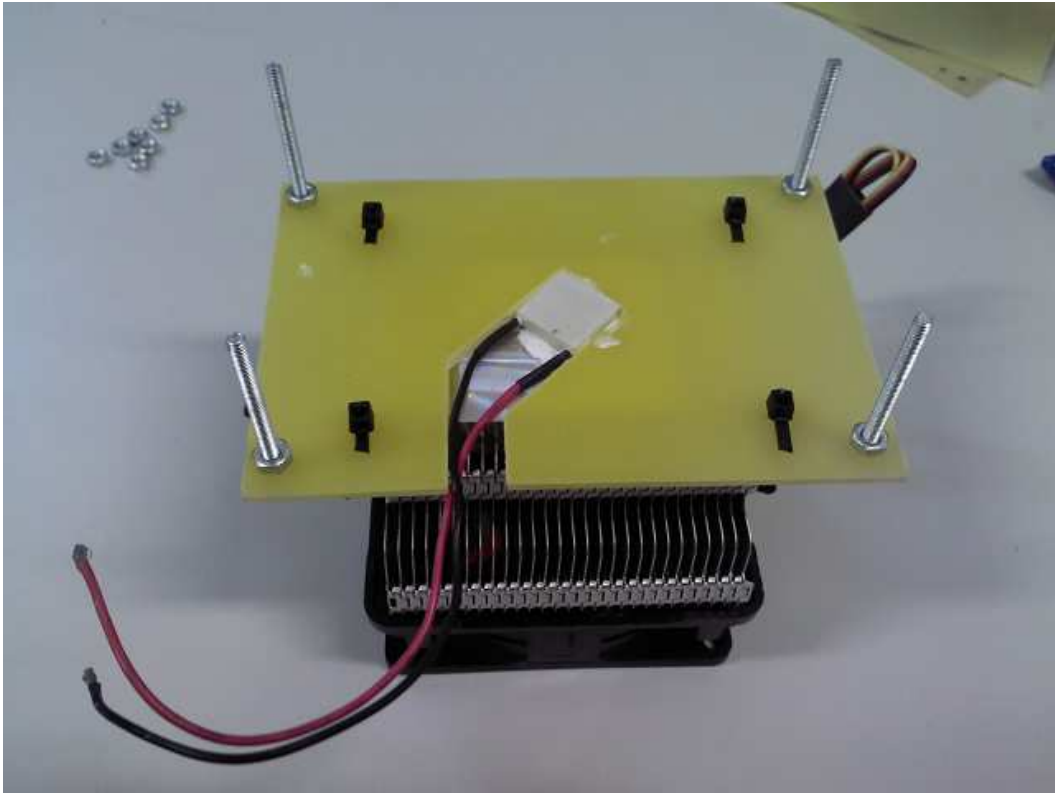
Figure C.6: Internal view of the thermal chamber.
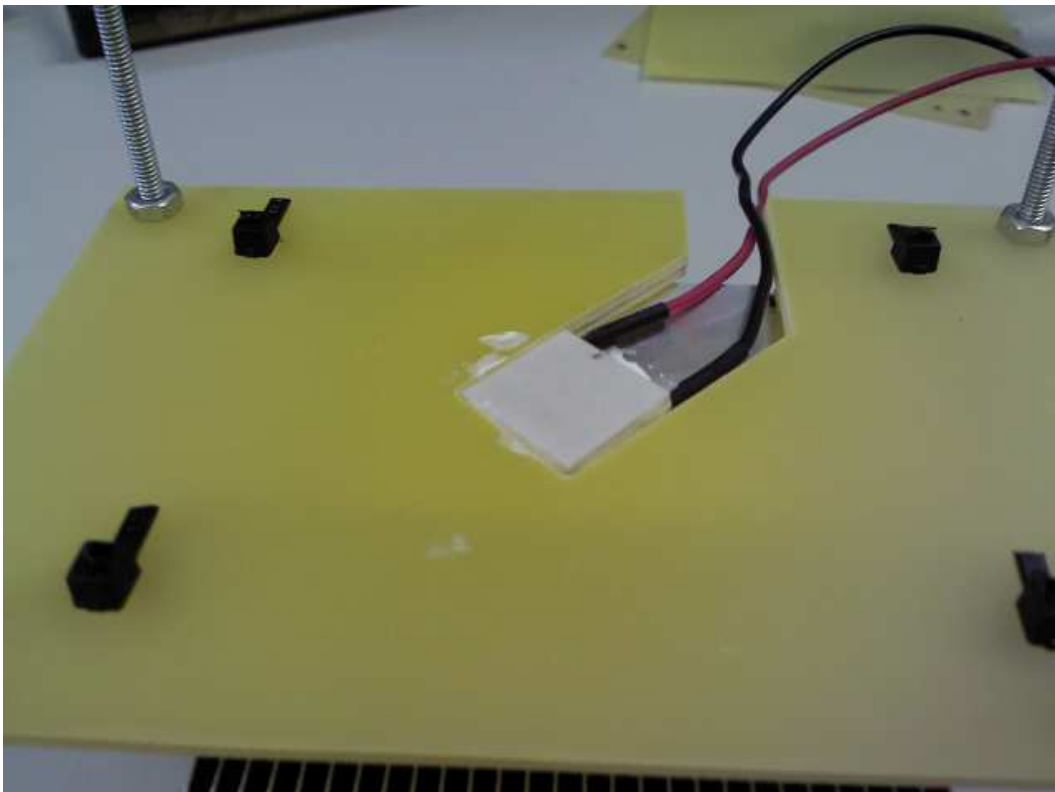
Figure C.7: Internal view of the thermal chamber, TEC detail.

Figure C.8: Internal view of the thermal chamber, FBG installation.

C.3 Pictures of the control board

Figure C.9: Control board picture.
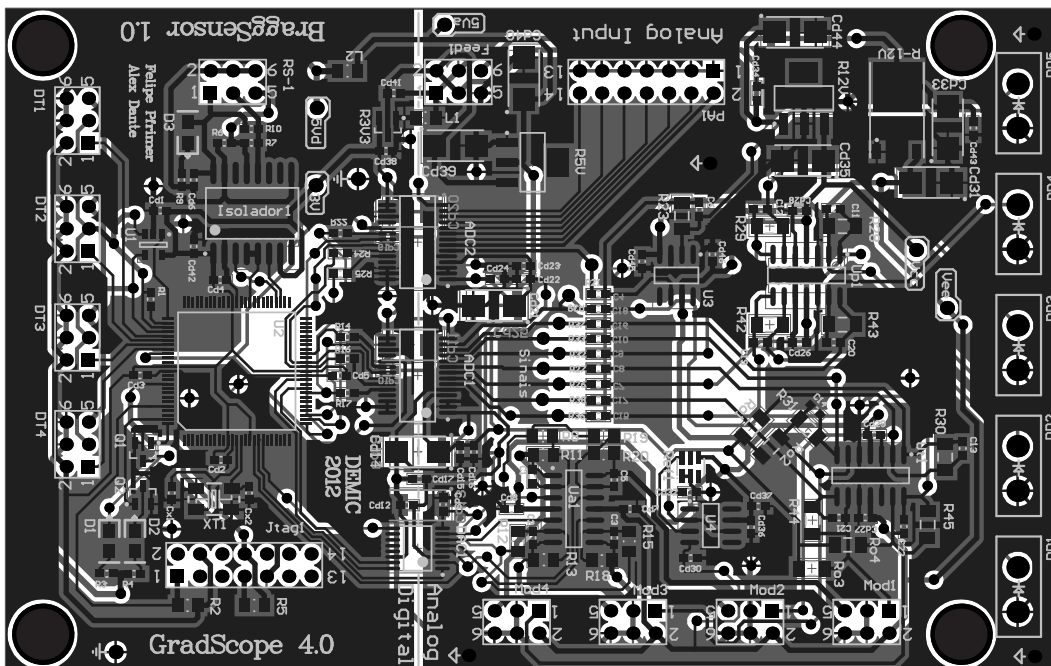
Figure C.10: Control board layout.

C.4   Pictures of the TEC driver
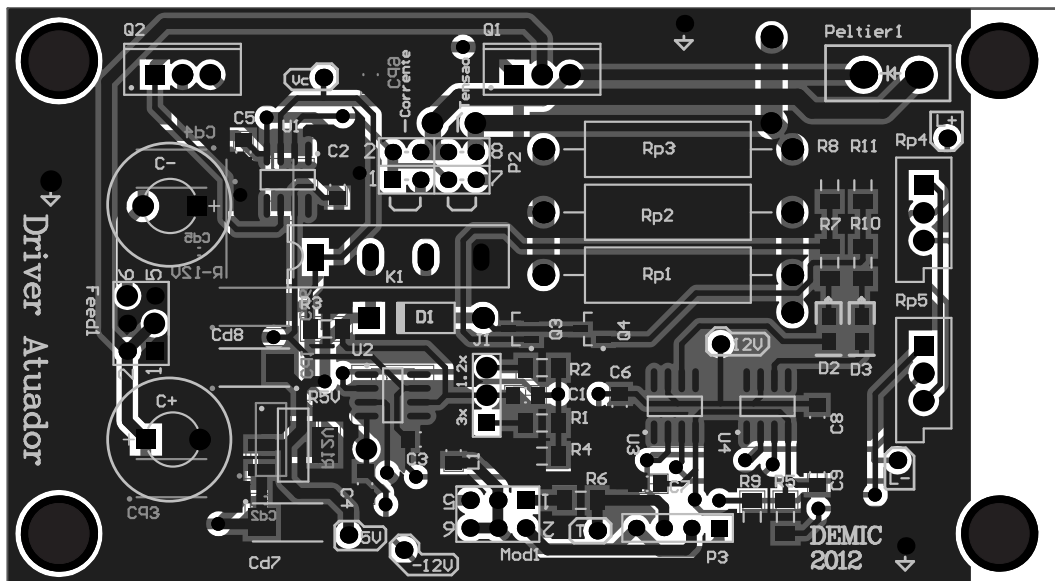
Figure C.11: TEC driver board layout.
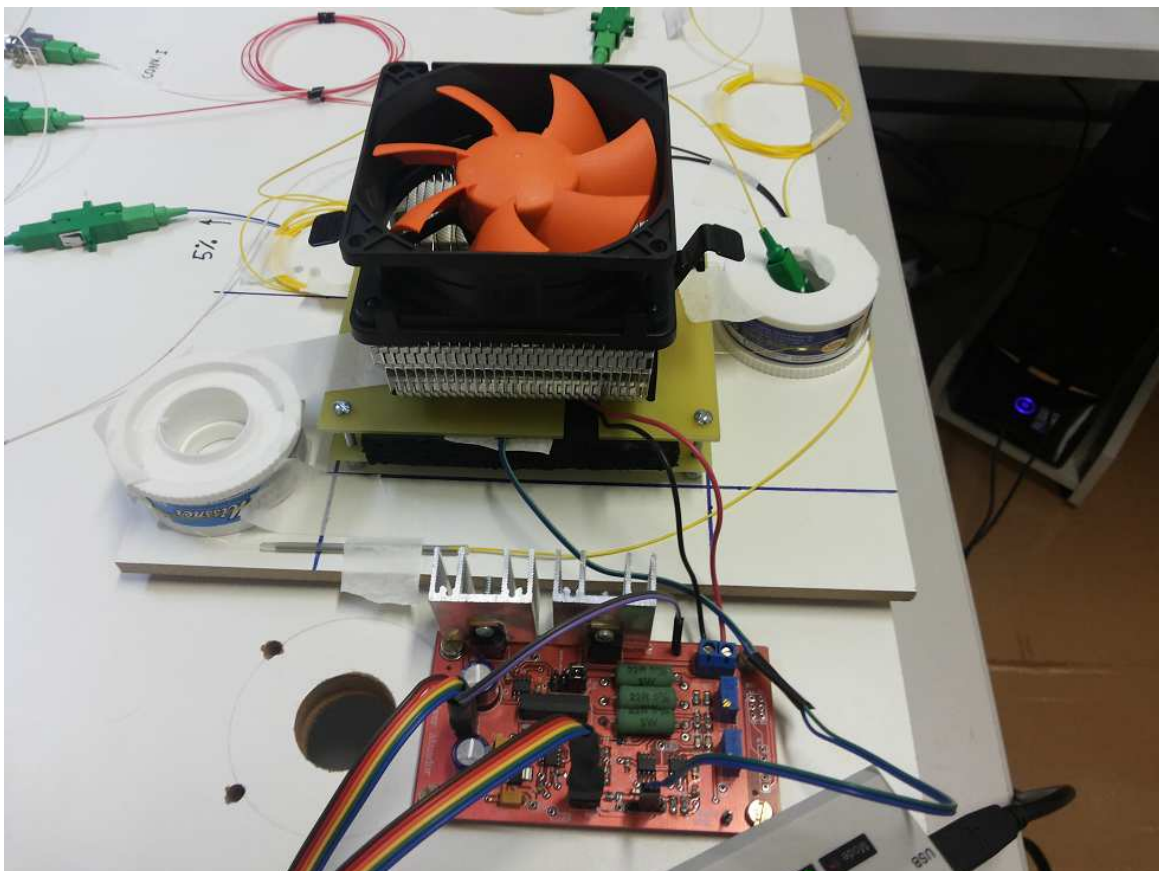
Figure C.12: TEC driver board connected to a thermal chamber (STB 1).

C.5   Front panel of the Labview software

Figure C.13: Front panel of the Labview software.

Appendix D

Electronics schematics

D.1 Interface and isolation board schematics
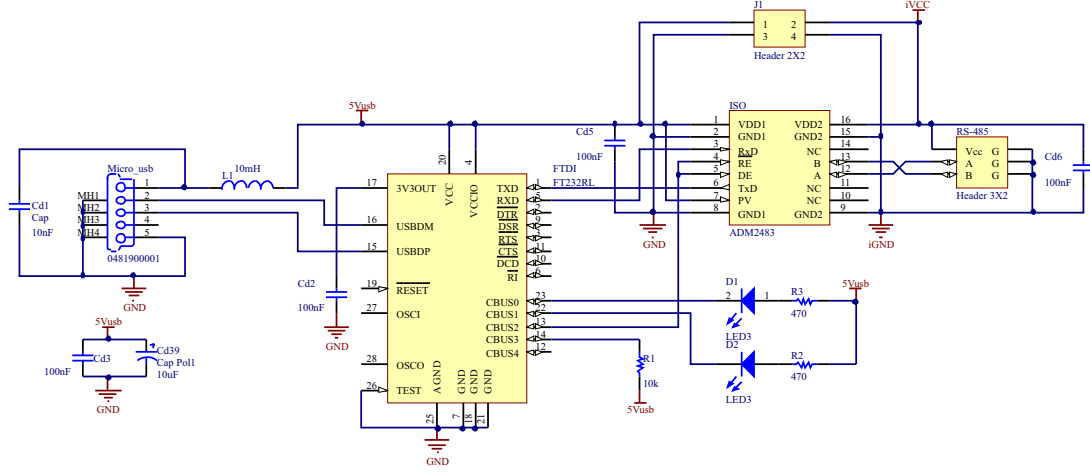
Figure D.1: Interface and isolation board schematics.

D.2 TEC driver schematics
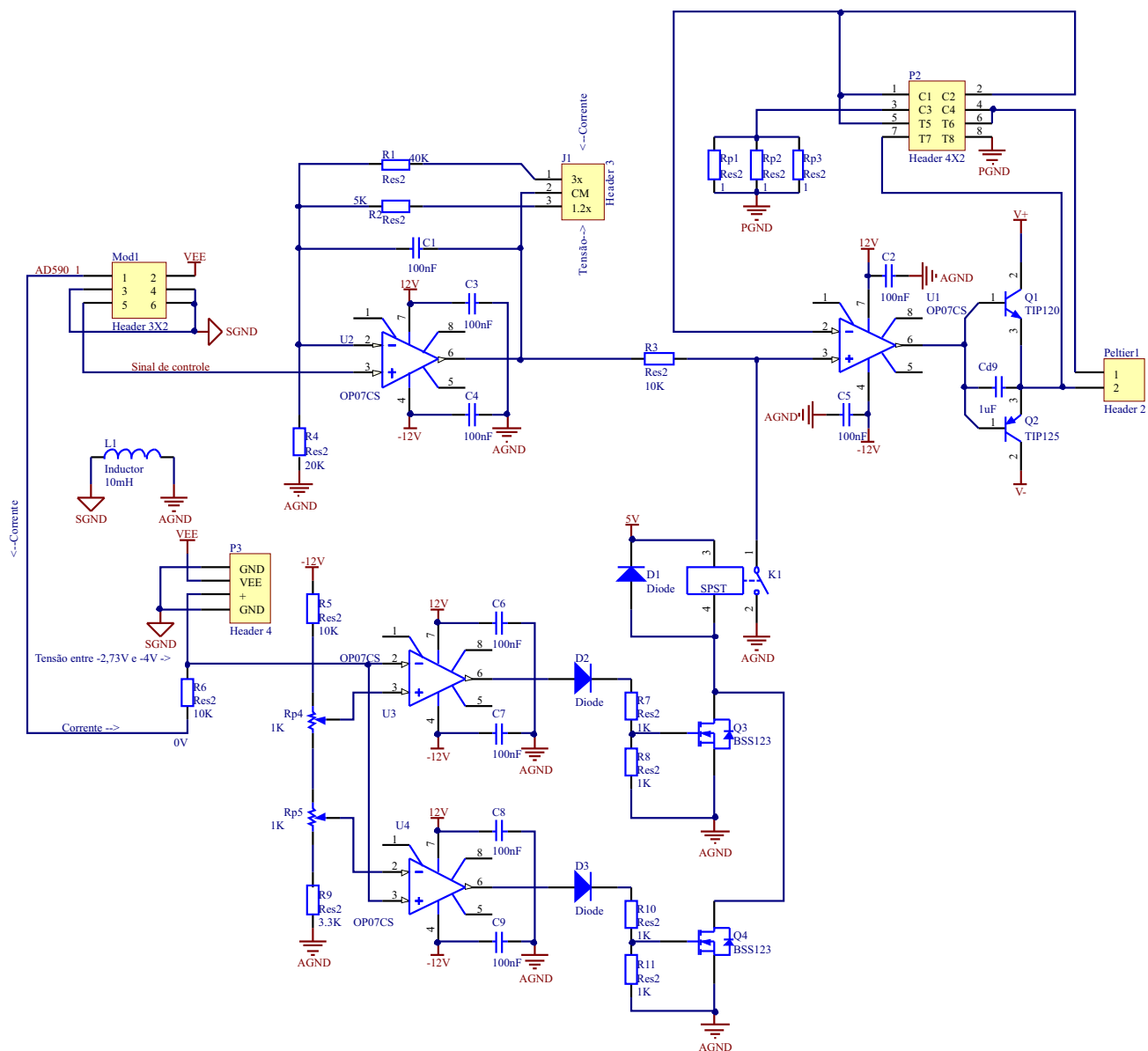
Figure D.2: TEC driver schematics.

Figure D.3: Control board schematics - analog circuits.

Figure D.4: Control board schematics - digital circuits.
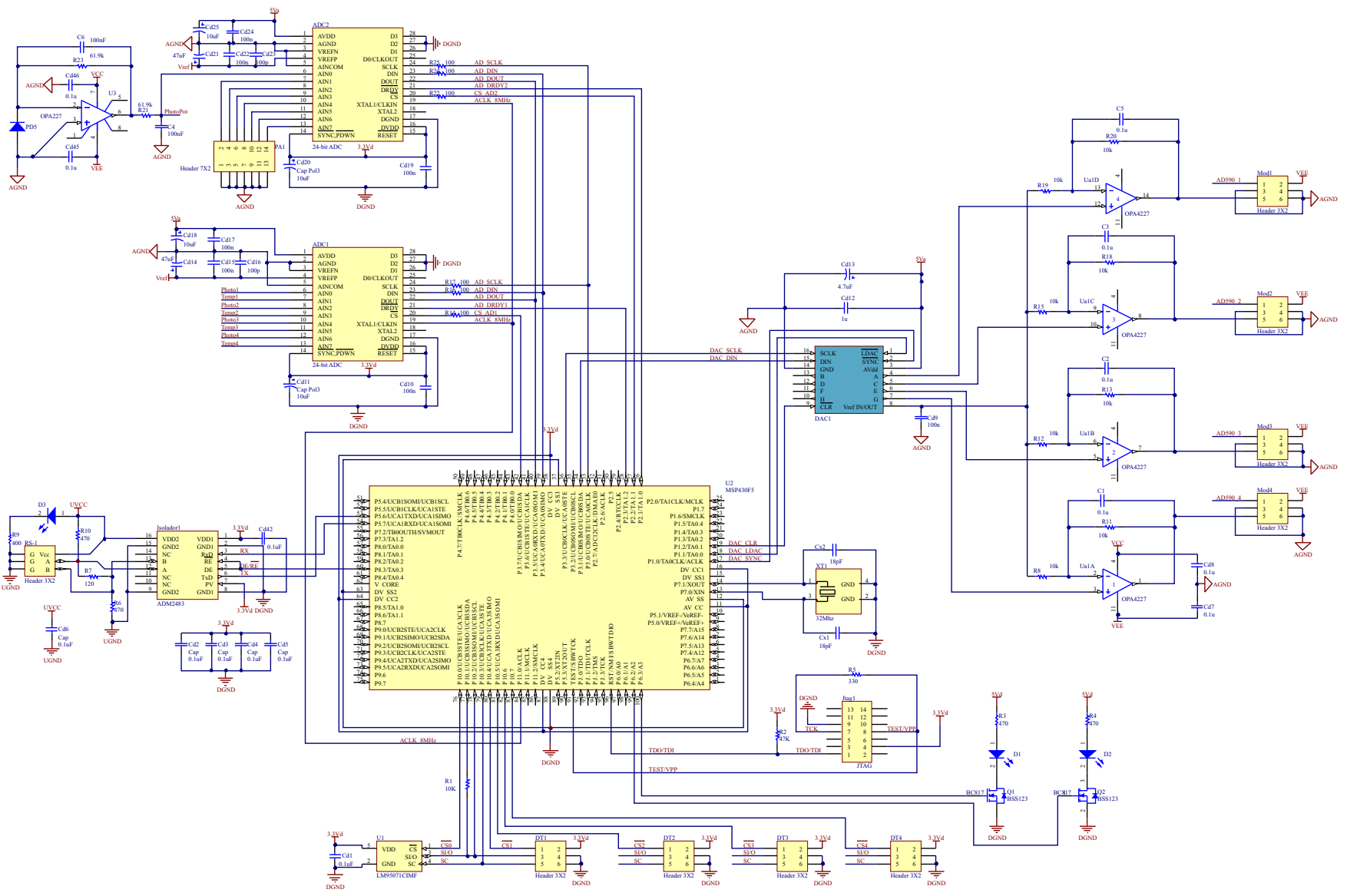
Bibliography

AC Photonics (2011a). Polarization-insensitive dual-stage optical isolator, *Technical report*, AC Photonics Inc.

AC Photonics (2011b). Polarization insensitive optical circulator, *Technical report*, AC Photonics Inc.

AC Photonics (2011c). Single mode optical couplers, *Technical report*, AC Photonics Inc.

Albert, J. (2011). *Fiber Bragg Grating Sensors: Research Advancements, Industrial Applications and Market Exploitation*, Bentham Science Publishers.

Allan, W. R., Graham, Z. W., Zayas, J. R. & Roach, D. P. (2009). Multiplexed Fiber Bragg Grating Interrogation System Using a Microelectromechanical Fabry-Perot Tunable Filter, *IEEE Sensors Journal* **9**: 936 – 943.
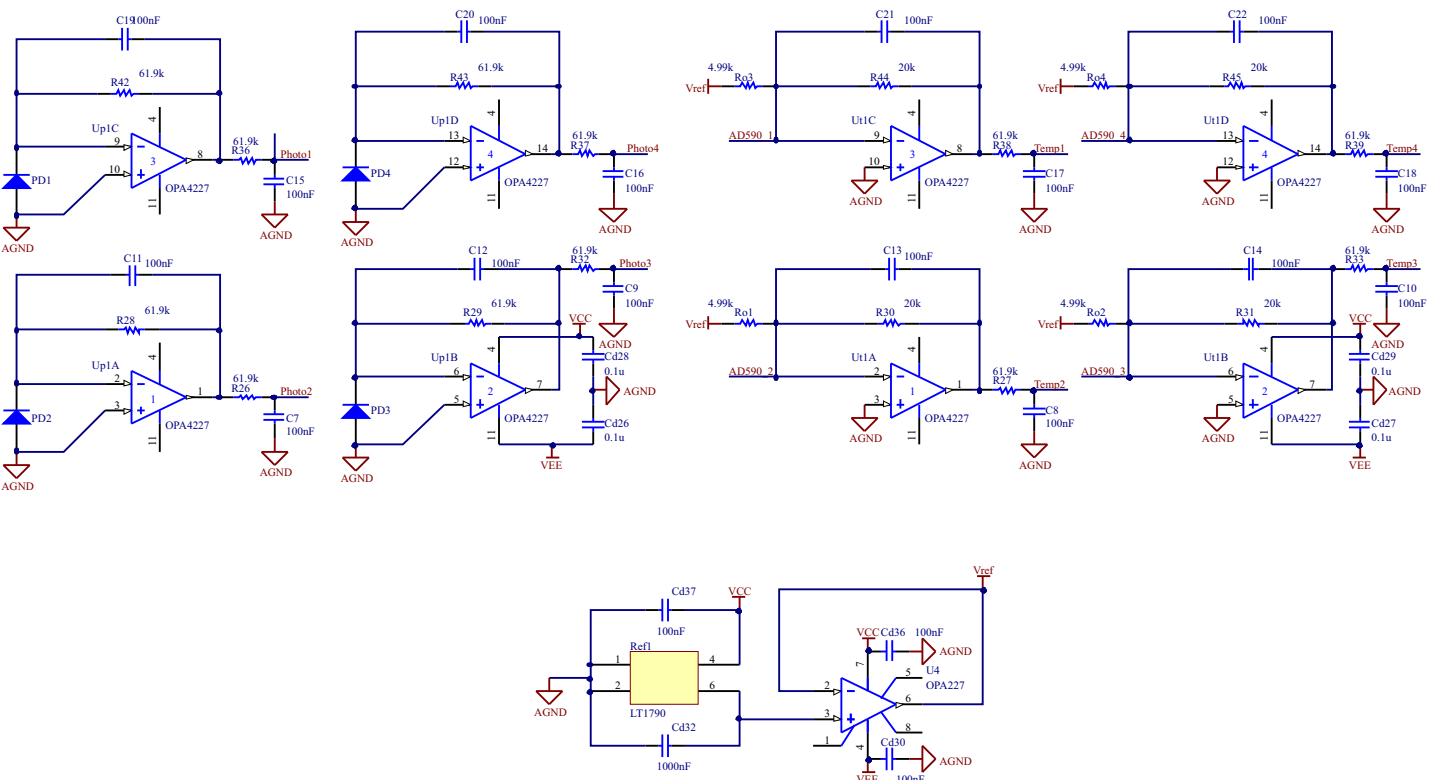
Analog (2013). AD590: 2-Terminal IC Temperature Transducer REV-G, *Technical report*, Analog Devises Inc.

Analog Devises (2005). Half-Duplex, iCoupler, Isolated RS-485 Transceiver, *Technical report*, Analog Devises Inc.

Araki, M. (1984). *Control Systems, Robotics and Automation*, EOLSS.

Archambaut, J. L., Reekie, L. & Russel, P. S. J. (1993). 100% reflectivity Bragg reflectors produced in optical fibers by single excimer laser pulses, *Electronic Letters* **29**: 453–455.

Atkins, R., Lemaire, P., Erdogan, T. & Mizrahi, V. (1993). Mechanisms of enhanced UV photosensitivity via hydrogen loading in germanosilicate glasses, *Electronics Letters* .

Atkins, R. M. & Mizrahi, V. (1992). Observations of changes in UV absorption bands of singlemode Germanosilicate core optical fibers on writing and thermally erasing refractive index gratings, *Electronics Letters* **28**: 1743–1752.

Baldwin, C., Kiddy, J., Salter, T. & Chen, P. (2002). Fiber optic structural health monitoring system: rough sea trials testing of the RV Triton, *OCEANS 2002 MTS/IEEE*, Vol. 3, pp. 1806 – 1813.

Ball, G. A., Morey, W. W. & Glenn, W. H. (1991). Standing-wave monomode erbium fiber laser, *IEEE Photonics Technology Letters* **3**: 613–615.

Banks, C. & Grant, J. (2007). Strain Measurement Using FBG on COPV in Stress Rupture Test, *Technical report*, NASA Marshall Space Flight Center.

Boulet, C., Webb, D. J., Douay, M. & Niay, P. (2001). Simultaneous interrogation of fiber Bragg grating sensors using an acoustooptic tunable filter, *IEEE Photonics Technology Letters* **13**: 1215 – 1217.

Brady, G. P., Hope, S., Ribeiro, A. B., Webb, D. J., Reekie, L., Archambault, J. L. & Jackson, D. A. (1994). Demultiplexing of fibre Bragg grating temperature and strain sensors, *Optics Communications* **111**: 51 – 54.

Briano, B. (2011). Breaking Ground Loops to Protect USB Data Transmission, *Technical report*, Analog Devises.

Burr-Brown (1998). High Precision, Low Noise OPERATIONAL AMPLIFIERS, *Technical report*, Texas Instruments Incorporated.

Cai, Z., Hao, J., Dong, B. & Chiam, J. P. T. M. (2012). Design of a Fiber Bragg Grating Sensor Interrogation System using Volume Phase Grating and CCD Detection, *Proc. of 22nd International Conference on Optical Fiber Sensors* **8421**: 84213N–1–4.

Cremonezi, A. O., Ferreira, E. C., Filho, A. J. B. & Dias, J. A. S. (2013). A Fiber Bragg Grating RMS Current Transducer Based on the Magnetostriction Effect Using a Terfenol-D Toroidal-Shaped Modulator, *IEEE Sensors Journal* **13**: 683 – 690.

da Costa, E. F. (2009). *Eletrônica de controle de um sensor de temperatura óptico que utiliza FBG*, Master's thesis, Universidade Estadual de Campinas.

da Silva, J. C. C. (2005). *Monitoração de vibrações de estruturas com emprego de sensores em fibra ótica*, PhD thesis, Centro Federal de Educação Tecnológica do Paraná.

da Silva, J. M. G. & Bazanella, A. S. (2000). Ajuste de Controladores PID.

Dante, A. (2012). *Uma nova técnica para caracterização de grades de Bragg em fibra óptica utilizando um método de deconvolução*, PhD thesis, Universidade Estadual de Campinas.

Davis, M. A. & Kersey, A. D. (1995). Matched-filter interrogation technique for fibre Bragg grating arrays, *Electronics Letters* **31**: 822 – 823.

Davis, M., Bellemore, D., Putnam, M. & Kersey, A. (1996). Interrogation of 60 fibre Bragg grating sensors with microstrain resolution capability, *Electronics Letters* **32**: 1393– 1394.

Denselight (2007). Superluminescent LED Box DL-BX9-CSxxxxA, *Technical report*, DENSE-LIGHT SEMICONDUCTORS INC.

Dong, L., Archambault, J. L., Reekie, L., Russel, P. S. J. & Payne, D. N. (1993). Single pulse Bragg gratings written during fibre drawing, *Electronic Letters* **29**: 1577–1585.

Dong, X., Zhang, H., Liu, B. & Miao, Y. (2011). Tilted Fiber Bragg Gratings: Principle and Sensing Applications, *Photonic Sensors* **1**: 6–30.

Epsilon (2013). EA-3000-H series Fibre-optic Sensor Interrogation (FSI) unit, *Technical report*, Epsilon Optics Inc.

Erdogan, T. (1997). Fiber Grating Spectra, *Journal of Lightwave Technology* **29**: 1577–1585.

Fallon, R. (1997). Multiplexed identical broad-band-chirped grating interrogation system for large-strain sensing applications, *Photonics Technology Letters, IEEE* **9**: 1616– 1618.

Froggatt, M. (1996). Distributed measurement of the complex modulation of a photoinduced Bragg grating in an optical fiber, *Applied Optics* **35**: 5162 – 5164.

FTDI (2010). FT232R USB UART IC Datasheet Version 2.10, *Technical report*, Future Technology Devices International Ltd.

Gong, J. (2002). A novel wavelength detection technique for fiber Bragg grating sensors, *Photonics Technology Letters, IEEE* **14**: 678– 680.

Graver, T. (2008). How do FBG sensor interrogators work?, *Technical report*, Micron Optics.

Grobnic, D., Mihailov, S., Smelser, C. & Ramos., R. (2008). Ultrafast IR Laser Writing of Strong Bragg Gratings Through the Coating of High Ge-Doped Optical Fibers, *Photonics Technology Letters* **20**: 973 – 975.

Hecht, J. (1999). *City of light: the story of fiber optics*, Oxford University Press.

Hill, K. O., Fujii, Y., Johnson, D. C. & Kawasaki, B. S. (1978). Photosensitivity in optical fiber waveguides: Application to reflection filter fabrication, *Applied Physics Letters* **32**: 647.

Hill, K. O., Malo, B., Bilodeau, F. & Johnson, D. C. (1993). Photosensitivity in Optical Fibers, *Annul Review of Materials Science* **23**: 125–157.

Hill, K. O., Malo, B., Bilodeau, F., Johnson, D. C. & Albert, J. (1993). Bragg gratings fabricated in monomode photosensitive optical fiber by UV exposure through a phase mask, *Applied Physics Letters* **62**.

Jackson, D. A., Ribeiro, A. B. L., Reekie, L., & Archambault, J. L. (1993). Simple multiplexing scheme for a fiber-optic grating sensor network, *Optics Letters* **18**: 1192 – 1194.

Jeunhomme, L. B. (1990). *Single-mode fiber optics: principles and applications*, 2nd edn, M. Dekker.

Kashyap, R. (1999). *Fiber Bragg Gratings*, Academic Press.

Kawasaki, B. S., Hill, K. O., Johnson, D. C. & Fujii, Y. (1978). Narrow-band Bragg reflectors in optical fibers, *Optics Letters* **Vol. 3**: 66–68.

Kerrouche, A., Leighton, J., Boyle, W. J. O. & Gebremichael, Y. M. (2008). Strain Measurement on a Rail Bridge Loaded to Failure Using a Fiber Bragg Grating-Based Distributed Sensor System, *IEEE Sensors Journal* **8**: 2059 – 2065.

Kersey, A. D. (1997). Fiber Grating Sensors, *IEEE Journal of lightwave technology* **15**: 1442–1463.

Kersey, A. D., Berkoff, T. A. & Morey, W. W. (1993). Multiplexed fiber Bragg grating strain-sensor system with a fiber Fabry-Perot wavelength filter, *Optics Letters* **18**: 1370–1372.

Kreuzer, M. (2008). Strain Measurement with Fiber Bragg Grating Sensors, *Technical report*, HBM.

Kuntz, D. (2011). An Introduction to Phase Masks for FBG Writing, *Technical report*, Coherent.

Laird (2009). Ceramic Plate Series CP10,31,05 Thermoelectric Modules, *Technical report*, Laird Technologies Inc.

Lam, D. K. W. & Garside, B. K. (1981). Characterization of single-mode optical fiber filters, *Applied Optics* **20**: 440–445.

Leite, J. A. S. D. R. L. & Ferreira, E. C. (2007). Electronic Technique for Temperature Compensation of Fibre Bragg Gratings Sensors, *International Journal of Electronics and Communications* **1**: 1 – 4.

Lemaire, P., Atkins, R., Mizrahi, V. & Reed, W. (1993). High pressure h_2 loading as a technique for achieving ultrahigh UV photosensitivity and thermal sensitivity in geo_2 doped optical fibres, *Electronics Letters* **29**: 1191–1193.

Lemaire, P. J. (1991). Reliability of optical fibers exposed to hydrogen: prediction of long-term loss increases, *Optical Engineering* **30**: 780–781.

Lima, H., Antunes, P., de Lemos Pinto, J. & Nogueira, R. (2013). Simultaneous Measurement of Strain and Temperature With a Single Fiber Bragg Grating Written in a Tapered Optical Fiber, *IEEE Sensors Journal* **10**: 269–273.

Linear (2009). LT1790: Micropower SOT-23 Low Dropout Reference Family, *Technical report*, Linear Technology Corporation.

Liu, Y., Williams, L., Zhang, L. & Bennion, I. (2002). Abnormal sectral evolution of fiber Bragg gratings in hydrogenated fibers, *Optics Letters* **27**: 586–568.

Malo, B., Hill, K., Bilodeau, F., Johnson, D. C. & Albert, J. (1993). Point-by-point fabrication of micro-Bragg gratings in photosensitive fibre using single excimer pulse refractive index modification techniques, *Electronics Letters* **29**.

Martin, J. & Ouellette, F. (1995). Novel writing technique of long and highly reflective in-fibre gratings, *Electronics Letters* **30**: 811– 812.

Melle, S. M., Liu, K. & Measures, R. M. (1992). A passive wavelength demodulation system for guided-wave Bragg grating sensors, *IEEE Photonics Technology Letters* **4**: 516 – 518.

Meltz, G. & Moery, W. W. (1991). Bragg Grating Formation and Germanosilicate Fiber Photosensitivity, *Proceedings SPIE* .

Meltz, G., Morey, W. W. & Glenn, W. H. (1989). Formation of Bragg gratings in optical fibers by a transverse holographic method, *Optics Letters* **Vol. 14**: 823–825.

MicronOptics (2009). Fiber Bragg Grating: OS1100, *Technical report*, Micron Optics Inc.

Mizrahi, V. & Sipe, J. E. (1993). Optical properties of photosensitive fiber phase mask, *Journal of Lightwave Technology* **11**: 1513–1517.

Méndez, A. (2007). Fiber Bragg grating sensors: a market overview, *Third European Workshop on Optical Fibre Sensors* **Proceedings of SPIE**.

Morikawa, S. R. K., Camerini, C. S., Pipa, D. R., Santos, J. M. C., Pires, G. P., Braga, A. M. B., Llerena, R. W. A. & Ribeiro, A. S. (2008). Monitoring of Flexible Oil Lines Using FBG Sensors, *19th International Conference on Optical Fibre Sensors*, Vol. 7004, pp. 70046F–1,4.

Nunes, L. C. S., Valente, L. C. G. & Braga, A. M. B. (2004). Analysis of a demodulation system for fiber Bragg grating sensors using two fixed filters, *Optics and Lasers in Engineering* **42**: 529 – 542.

Othonos, A. & Kalli, K. (1999). *Fiber Bragg gratings: fundamentals and applications in telecommunications and sensing*, Artech House.

Pfrimer, F. W. D., Koyama, M. H., Ferreira, E. C. & Dias, J. A. S. (2013). Closed-loop Interrogation Techniques for Temperature Measurement Using Fibre Bragg Gratings, *International Conference on Photonics, Optics and Laser Technology* .

Rao, Y. J., Jackson, D. A., Zhang, L. & Bennion, I. (1996). Strain sensing of modern composite materials with a spatial=wavelength-division multiplexed fiber grating network, *Optical Letters* **21**: 683 – 685.

Rao, Y. J., Kalli, K., Brady, G., Webb, D. J., Jackson, D. A., Zhang, L. & Bennion, I. (1995). Spatial multiplexed fiber-optic Bragg grating strain and temperature sensor system based on interferometric wavelength-shift detection, *Electronic Letters* **31**: 1009 – 1010.

Rhead, P. (2008). Fibre optic Sensing Technology and applications in wind energy, *Technical report*, Insensys.

Riant, I. & Haller, F. (1997). Study of photosensitivity at 193 nm and comparison with photosensitivity at 240 nm influence of fiber tension: type IIA aging, *Journal of Lightwave Technology* **15**: 1464–1469.

Russell, Archambault, J. L. & Reekie, L. (1993). Fibre gratings, *Physics World* pp. 41–46.

Silva, R. G. R., Ferreira, E. C. & Dias, J. A. S. (2013). Low-cost technique for the interrogation of optical FBG temperature measurement sensors, *International Journal of Electronics - Accepted to publication* .

Simpson, A. G., Kalli, K., Zhou, K., Zhang, L. & Bennion, I. (2003). An idealized method for the fabrication of temperature invariant IA-I strain sensors, *16th Internation Conference on optical Fibre Sensors* **OFS'2003**: 14–17.

Stone, J. (1987). Photorefractivity in GeO2-doped silica fibers, *Journal Applied Physics* **62**: 4371–4376.

Texas Instruments (2003). ADS1256 Very Low Noise, 24-Bit, Analog-to-Digital Converter, *Technical report*, Texas Instruments Inc.

Texas Instruments (2009). DAC8568 Digital-to-Analog Converter Datasheet, *Technical report*, Texas Instruments Inc.

Texas Instruments (2010). MSP430F5438A Mixed Signal Microcontroller datasheet, *Technical report*, Texas Instruments Inc.

Volanthen, M., Geiger, H., Xu, M. G. & Dakin, J. P. (1996). Simultaneous monitoring of multiple fibre gratings with a single acousto-optic tunable filter, *Electronics Letters* **32**: 1228 – 1229.

Wang, Q., Jewart, C. M., Canning, J., Grobnic, D. & andand Kevin P. Chen, S. J. M. (2011). High-temperature fiber Bragg grating sensors in microstructured fibers for harsh environment applications, *NETL UCR Annual Meeting* .

Wang, Q., Zhang, L., Sun, C. & Yu, Q. (2008). Multiplexed Fiber-Optic Pressure and Temperature Sensor System for Down-Hole Measurement, *IEEE Sensors Journal* **8**: 1879 – 1883.

Wood, K., Brown, T., Rogowski, R. & Jensen, B. (2000). Fiber optic sensors for health monitoring of morphing airframes: I. Bragg grating strain and temperature sensor, *Smart Materials and Structures* **9**: 163 – 169.

Xu, M. G., Geiger, H. & Dakin, J. P. (1996). Modeling and performance analysis of a fiber bragg grating interrogation system using an acousto-optic tunable filter, *Journal of Lightwave Technology* **14**: 391 – 396.

Xu, M. G., Geiger, H., l. Archambault, J. & Reekie, L. (1993). Novel interrogating system for fibre Bragg grating sensors using an acousto-optic tunable filter, *Electronics Letters* **29**: 1510 – 1511.

Yu, F. T., Yin, S. & Ruffin, P. B. (2010). *Fiber Optic Sensors*, CRC Press.

Yuan, W., Stefani, A. & Bang, O. (2012). Tunable Polymer Fiber Bragg Grating (FBG) Inscription: Fabrication of Dual-FBG Temperature Compensated Polymer Optical Fiber Strain Sensors, *Photonics Technology Letters* .

Zhao, Y. & Liao, Y. (2004). Discrimination methods and demodulation techniques for fiber Bragg grating sensors, *Optics and Lasers in Engineering* **41**: 1–18.

Zhong, Z. Y., Zhi, X. L. & Yi, W. J. (2007). Oil Well Real-time Monitoring With Downhole Permanent FBG Sensor Network, *IEEE International Conference on Control and Automation*, pp. 2591 – 2594.

Zhou, Z., Graver, T. W., Hsu, L. & ping Ou, J. (2003). Techniques of Advanced FBG sensors: fabrication, demodulation, encapsulation and their application in the structural health monitoring of bridges, *Pacific Science Review* **5**: 116–121.